Cand. scient. thesis
in physics

Performance of the Time Projection Chambers of the BRAHMS experiment at RHIC

Jens Ivar Jørdre

University of Bergen
June 2000

Preface

During my time as a student at the University of Bergen, and in particular while working with the project that has lead to this thesis, I have had the pleasure of working with and gettings assistance from a great many people. I would like to thank these people for all the time spent and for answering all my questions.

In particular I would like to thank professor Dieter Röhrich for supervising my work and guiding me through the world of experimental nuclear physics to the very end of my thesis. Also I owe great thanks to late professor Tor Fredrik Thorsteinsen. He introduced me to experimental nuclear physics and has been an important source for inspiration.

I would also like to thank the entire experimental nuclear physics group at the departement in Bergen. It is a priviledge to be surrounded by and study together with people like you.

Many people in the BRAHMS collaboration deserve thanks for letting me in to the mysterious ways of the experiment. Especially I would like to thank spokesman Flemming Videbæk, Ramiro Debbe and Konstantin Olchanski at Brookhaven National Laboratory for helping me out with questions and tests, and letting my stays there be of great interest and inspiration. Also I thank professor Jens Jørgen Gaardhøje, Ian Bearden and Børge Svane Nielsen at the Niels Bohr Institute, Copenhagen, for important guidance and for letting me participate in detector test in Århus, Denmark, spring 1999.

I have had the priviledge of travelling a great deal in connection with the work on this thesis and as a student at the Departement of Physics. I had a very nice stay as summer student at CERN in 1998. I was very lucky to share office with Lucien Montanet and work with Rolf Landua, who both inspired me a lot. It has been of great interest to be able to participate at conferences and meetings in Copenhangen, Sicilly, Brookhaven and Oslo.

Finally I would like to thank my wife Tone for always being there for me. Without her support and understanding this thesis would not have been possible. I owe her everything.

Bergen, May 2000

Jens Ivar Jørdre

Contents

List of Figures

List of Tables

Introduction

In the 60s it was suggested that the particles from which the atomic nucleus is made, the proton and neutron, contain even smaller constituents. These constituents were named quarks and gluons. Experiments in the 70s supported this theory. However, these elementary particles have never been observed as free particles. They are always hidden inside other particles, called hadrons. Protons and neutrons are two kinds of hadrons.

The laws of nature does not seem to allow free quarks and gluons, or partons as these two particles are often called. It has been suggested, however, that if the nuclear matter is put under high pressure and/or high temperatures, conditions will be reached in which a phase transition will occur. The new phase of nuclear matter is called a quark-gluon plasma (QGP). Within the plasma it is expected that quarks and gluons can move freely.

In order to reach high enough densities and temperatures nuclei have to be accelerated in nuclear accelerators. At high energies the accelerated nuclei collide either with a fixed target or with other nuclei accelerated in the opposite direction. The main facilities for this kind of scientific research are the Centre Européen pour la Recherche Nucléaire (CERN) close to Geneva, Switzerland, and Brookhaven National Laboratory (BNL) at Long Island, USA. In their facilities heavy ions are accelerated very close up to the speed of light. The outgoing particles from collisions are detected and studied, as many of the characteristics of the collisions show up in the dynamics and distributions of outgoing particles.

The outgoing particles provide the sole way of studying the collision. The reason for this is the short time intervals and spatial dimensions in which nuclear interactions at high energies take place. The typical time for interactions in modern accelerators is 10^{-23} s, i.e. the time for two nuclei to pass each other. If the nuclei collide head on, their common nuclear matter may reach dimensions of a few fm. It is therefore impossible to observe such a collision directly. One has to rely on the outcome of particles from collisions, so called signatures. Also if a QGP is produced, it will have a similar lifetime and spatial dimensions. The outcome of particles from a QGP is expected to be different from the outcome if no QGP is produced.

The search for the QGP has been the main focus in relativistic heavy ion physics for many years. As more and more experiments have been performed, also quite a few signatures seem to undermine the existence of a QGP. They can not be explained by theories without introducing a phase transition. Earlier this year a seminar was held from which the conclusion was that a new state of matter has been observed. Very little, however, is known about the this state, not enough to call it a QGP, and new experiments are running or being planned to investigate further this new state of matter. At BNL a new heavy ion collider called RHIC is about to start colliding gold nuclei, and at CERN the LHC accelerator is being built for startup in 2005. Both of these accelerators go one step further in collision energy and will provide better possibilities to study the new state.

One of the experiments in connection to the RHIC collider is named BRAHMS. The Experimental Nuclear Physics Group at the Department of Physics, University of Bergen, is participating in this experiment. The purpose of this thesis is to test one of the detectors to be used in the BRAHMS detector setup. The detector is a Time Projection Chamber, named T1.

T1 has been tested to detect cosmic radiation, and I have used the output from these tests to investigate its performance. Before it is placed along the collider, at the collision point, several parameters have to been known. From the cosmic test data one can estimate these parameters.

In chapter 1 the basic theory including the quark-gluon plasma is presented. Chapter 2 deals with the RHIC collider and the BRAHMS detector setup. The principles for the Time Projection Chamber are explained in chapter 3, and in chapter 4 the analysis tools are presented. Finally the result of the analysis of test data are given in chapter 5.

Chapter 1

Quark-gluon plasma and relativistic heavy ion experiments

During the past decades physicists in the field of relativistic heavy ion experiments have been motivated in their research by the quest for the quark-gluon plasma. This first chapter will introduce fundamental concepts and parameters used in the field. Different ways of indirectly detecting a quark-gluon plasma will be presented. But first a look into the basic constituents of matter, described in *The Standard Model*.

1.1 The Standard Model

Matter as we see it around us on the earth is made up of atoms. More than 100 different families of atoms, called elements, have been found and cataloged in *The periodic table of elements*. All atoms have the same basic construction, with a nucleus made of protons and neutrons, and electrons in orbitals surrounding the nucleus.

1.1.1 The basic constituents

Hadrons

Protons and neutrons are commonly referred to as *nucleons*. Nucleons are members of a big group of particles called *hadrons*, whose main common characteristic is that they are made up of *quarks*. Six different quarks have been found in experiments since quarks were introduced in theory in the sixties. Particles in general are given quantum numbers to illustrate some characteristic feature, and the quantum number *flavour* is generally used to distinguish types of quarks from one another. Thus six different quark flavors are known, i.e. u (up), d (down), s (strange), c (charm), b (bottom) and t (top). Quarks are believed to be point like spin 1/2 particles, i.e. they are *fermions*.

The quarks are divided into three families according to the energy regime in which they occur. Ordered from left to right with increasing energy we have:

$$\begin{pmatrix} u \\ d \end{pmatrix} \quad \begin{pmatrix} c \\ s \end{pmatrix} \quad \begin{pmatrix} t \\ b \end{pmatrix}$$

Their energy regime is directly related to their mass, through Einstein's famous formula $E = mc^2$ [1]. Each of the six quarks has an antiquark having the same mass and spin, but with the rest of the quantum numbers having opposite sign. Table 1.1 summarizes some basic feature of quarks

Flavor	**Mass, m** $[GeV/c^2]$	**El. charge, q** $[e]$	**Baryon number B**	**Spin, s** $[\hbar]$
u	0.0015 - 0.005	2/3	1/3	1/2
d	0.003 - 0.009	-1/3	1/3	1/2
s	0.060 - 0.170	-1/3	1/3	1/2
c	1.1 - 1.4	2/3	1/3	1/2
b	4.1 - 4.4	-1/3	1/3	1/2
t	168.6 - 179.0	2/3	1/3	1/2

Table 1.1: *Summary of quark characteristics* [PDG98]

Quarks group in numbers of two or three to form hadrons. Hadrons with two quarks are called *mesons* and the ones with three quarks are called *baryons*. The grouping of quarks is such that all hadrons have integral electric charge in units of the elementary electric charge[2] e, ranging from -1 to $+2$. Mesons are made of one quark and one antiquark, resulting in a total baryon number for the meson of $B_{meson} = 0$. Baryons are made of three quarks giving baryon number $B_{baryon} = 1$, while the three antiquarks in an antibaryon give it baryon number $B_{\overline{baryon}} = -1$.

Leptons

The electron finds its place in a group of particles called leptons. The Standard Model describes the existence of six different leptons. Similar to quarks leptons are believed to be point like spin 1/2 particles, and thus not made up of other smaller constituents. Also they are divided into three pairs according to their energy regime:

$$\begin{pmatrix} e \\ \nu_e \end{pmatrix} \begin{pmatrix} \mu \\ \nu_\mu \end{pmatrix} \begin{pmatrix} \tau \\ \nu_\tau \end{pmatrix}$$

The lepton families are described by their *lepton family number*, L_e, L_μ and L_τ. Except for ν_τ all leptons are have been detected directly in experiments [Pov95]. However it has been detected indirectly from τ decay data combined with ν reaction data [Fel81] [Alb92]. Leptons also have antiparticles, with the same mass and spin and opposite sign for the rest of the quantum numbers. Table 1.2 shows a summary of some characteristics of leptons.

For the neutrinos only upper limits for mass exist, and they were for a long time thought to be massless. In 1998, however, experimental data from the Super-Kamiokande

[1] The velocity of light $c = 299792458\ m/s$ [PDG98].

[2] e is the charge of one proton and the absolute value of the charge of a lepton. $e = 1.60217733(49) \cdot 10^{-19}\ C$ [PDG98].

Lepton	**Mass, m** $[MeV/c^2]$ (approximated)	**El. charge** q $[e]$	L_e	L_μ	L_τ	L $(L_e + L_\mu + L_\tau)$	**Spin** s $[\hbar]$
e	0.511	-1	1	0	0	1	1/2
ν_e	$< 7.2 \cdot 10^{-6}$	0	1	0	0	1	1/2
μ	105.7	-1	0	1	0	1	1/2
ν_μ	< 0.17	0	0	1	0	1	1/2
τ	1777.1	-1	0	0	1	1	1/2
ν_τ	< 18.2	0	0	0	1	1	1/2

Table 1.2: *Summary of lepton characteristics* [PDG98], m_{ν_e} from [Pov95]

facility in Japan led to the conclusion that there is a mass difference between neutrinos. Therefore not all of them can be massless [SKC98]

The symmetry between quark and leptons is outstanding, with three families of both kinds. Experimental measurements of cross-section of $e^+e^- \rightarrow hadrons$ compared to theoretical calculations indicate that there only exist three families of each. [Bu91]

The fundamental forces

Four fundamental forces are used to describe all interaction between the the basic constituents of matter: the strong nuclear force, the electromagnetic force, the weak nuclear force and gravitation. Each force is related to a certain charge and is mediated by exchange particles, all of which are integral spin particles (*bosons*). Commonly known is the relation between electric charge and the electromagnetic force. The electromagnetic force is mediated by massless photons.

In addition to having electric charge and flavour, quarks also have *color* or *color charge*. Color charge is the charge of the strong force, and only quarks and the exchange particle of the strong force, the *gluon*, have color charge.

The weak charge of a particle is related to its spin and direction of motion, the force being mediated by three heavy bosons named $W^\pm$ and Z^0.

Mediators of these three strongest forces are all known from experiments. Gravitation is believed to be mediated by a spin 2 boson called *graviton*, but has yet to be detected. Compared to the other three forces gravitation is very weak and therefore hardly ever taken into account when doing nuclear or particle physics experiments.

Interactions obey certain conservation laws. In all interactions momentum, energy, angular momentum, baryon number and lepton family number to mention some of them are conserved. The strong and the electromagnetic forces also obey conservation of flavor. In weak interactions, on the contrary, flavor is not conserved, and this is the reason why heavy quarks can decay into lighter ones.

The range is not the same for all forces. Generally a force with a massless exchange particle will have infinite range. This is the case with the electromagnetic and gravitational forces. However, even though gluons have no mass, the range of the strong force is on the order of 1 fm. The reason for this is that gluons have color charge, and therefore interact strongly (ref. sec. 1.5.3). The exchange particles of the weak force are really heavy particles, $m_{W^\pm} \approx 80\ GeV/c^2$ and $m_{Z^0} \approx 91\ GeV/c^2$. On the basis of *Heisenberg's uncertainty principle*[3] such heavy particles cannot move very far without conflicting with conservation of energy and momentum. The range of the weak force is therefore limited to the order of $10^{-3}\ fm = 1\ am$ ("atto meter").

Physicists always search for unifications, and it is a general wish to be able to unify the four forces in one basic force that maybe was the one force a short time after *The Big Bang*. So far the electromagnetic and the weak forces have been united in the *electroweak theory*, but *The Theory of Everything* is still a major motivation for many physicists.

1.1.2 Quarks, gluons and the strong interaction

Gluons possess color charge, and therefore they not only mediate the strong force but also interacts strongly themselves. Only quarks and gluons have color charge and can therefore interact by the strong nuclear force. The strong interaction between quarks and gluons is described in *QCD*, i.e. *Quantum Chromo Dynamics* (lat. "chromo" = color).

Hadrons are made of quarks with color. A quark can be *red*, *green* or *blue*. But a hadron in itself is always colorless. For baryons this is possible by having one quark of each color, thus giving a total of "white". In mesons the quark has color, the antiquark has the respective anticolor.

The strengths of the four fundamental forces is described by coupling constants, the coupling constant of the strong force being α_s. The strong coupling constant is not constant in the true meaning of the word, as it dependent upon separation between color charges and the momentum transfer in collisions. On short distances or large momentum transfer α_s goes to zero, and at that point two quarks can hardly feel the strong force from one another. This is called *asymptotic freedom*. With increasing separation however they get heavily bound. As a result of this free quarks have never been observed. They are always bound in hadrons. If one tries to separate say a quark and an antiquark, one only increases the energy in the *color field* between the quarks. At some point the energy in the field will be high enough to create a new quark-antiquark pair. The newly created quark then binds to the original antiquark and the new antiquark to the original quark. For this reason free quarks have never been observed.

1.2 Quark gluon plasma

Ordinary nuclear matter in atoms has a certain nuclear density, $\rho_0 \approx 0.15\ baryons/fm^3$, a value which changes very little from one element to another. Some decades ago it was generally believed that nuclear matter only had this density $\rho = \rho_0$. As more and more energetic collisions were possible through development in accelerator technology, this part of theory had to be modified. It is now believed that the nuclear density can vary, and that ρ_0 only is the density resulting in the lowest energy of the nuclear system. *The caloric equation of state* (fig. 1.1) expresses the content of energy in infinite nuclear matter per nucleon as a function of temperature and pressure/density, $E(\rho, p, T)$.

Relativistic heavy ion collisions is best described theoretically in *Lattice QCD*. The mobility of quarks and their effective mass has been calculated over a wide range of energy.

[3]This principle can be presented in two equivalent ways: $\Delta x \Delta p \leq \hbar/2$ and $\Delta E \Delta t \leq \hbar/2$

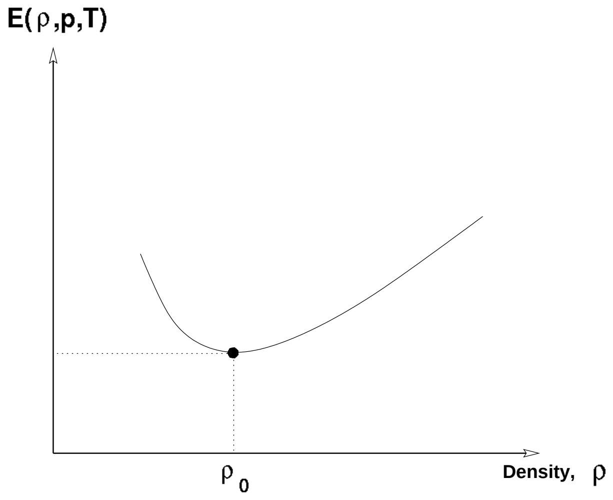

Figure 1.1: *The caloric equation of state as function of nuclear density*

At some energy threshold there is a drastic increase in quark mobility, and a decrease in effective mass [Kar95] [Lae96]. This gives indication that a new state of matter may exist, a state in which quarks and gluons are no longer bound in hadrons but can wander about freely within the system. Such a state has been calculated to occur at a critical temperature $T_c = 150 - 200\ MeV$, i.e. an energy density $\epsilon_c = 1 - 2\ GeV/fm^3$.

In relativistic heavy ion experiments it is possible to reach very high energy densities in nuclear collisions. Passing energy densities above ϵ_c it should therefore be possible to produce a new state of matter. When the kinematic distribution of this state starts resembling a thermal distribution it is generally called *quark-gluon plasma* (QGP). The dynamics of the plasma will be such that it expands with velocity comparable to the speed of light. As it expands energy density decreases, and below ϵ_c it will *hadronize*. This process is also referred to as *freezeout*. The quarks will group into hadrons, and because of the dynamics of the plasma the newly created hadrons will spread out in radial direction from the collision zone. The plasma will only exist for a very short amount of time, τ_{QGP}, on the order of $10^{-23}\ s$, and only reach dimensions of a few fm.

The quark-gluon plasma also touches the field of cosmology. It is believed that the universe was in a state of quark-gluon plasma on the order of a few micro seconds after *Big Bang*. An important stage in the development of the universe can thus be investigated through creation of quark-gluon plasma in the lab. It is also assumed that the density in the center of neutron stars is so high that quark-gluon plasma can exist there [Her96]. Fig. 1.2 illustrates the conditions for existence of quark-gluon plasma.

1.3 Kinematics

In modern accelerators heavy ions are accelerated up to velocities very close to the speed of light. At velocities above 0.1 c one generally has to introduce relativity into kinematic calculations. In this regime one can no longer perform Galilean transformations when

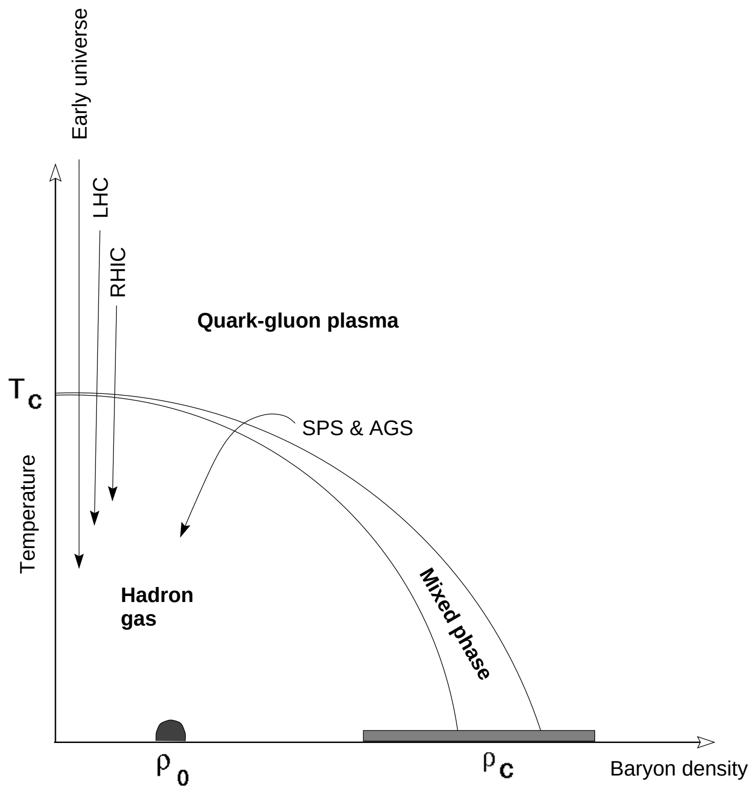

Figure 1.2: *Phase diagram for nuclear matter as function of temperature and nuclear density*

transforming quantities from one frame of reference to another. One has to use Lorentz transformations.

In relativistic heavy ion experiments particularly two reference frames are much used. One is the *lab frame* in which the accelerator and detectors have zero momentum, i.e. the frame we live in. The other frame is the *center of mass frame* in which the total momentum of a nuclear collision is zero.

Quantities that are easily scalable from one reference frame to another are generally preferred. One such quantity replacing velocity is *rapidity* defined as

$$y = tan^{-1}(\beta) = tan^{-1}(v/c) \tag{1.1}$$

At low velocities $y \approx \beta$. When going from one frame of reference (S) to another (S'), also in the relativistic regime, rapidity transform as in Galilean times, $y' = y + y_{S'}$, where $y_{S'}$ is the rapidity of S' relative to S.

Energy and momentum are related as

$$E^2 = p^2c^2 + m^2c^4 \tag{1.2}$$

The quantity *transverse mass*, m_T, given by

$$m_T^2c^4 = p_T^2c^2 + m^2c^4 \tag{1.3}$$

is often substituted into the above expression, giving

$$E^2 = p_L^2 c^2 + m_T^2 c^4 \tag{1.4}$$

Energy thus has a longitudinal component $E_L = p_L c$ and a transverse component $E_T = m_T c^2$.

At relativistic energies where $pc \gg mc^2$ *pseudorapidity*, η, is also used. It is defined as

$$\eta = \frac{1}{2} \ln \frac{p + p_L}{p - p_L}. \tag{1.5}$$

In fact pseudorapidity only depends on the *scattering angle*, θ, as

$$\eta = tan^{-1}(cos\theta). \tag{1.6}$$

The scattering angle is the angle that the outgoing momentum of a particle makes with its incoming momentum. At these high energies $y \approx \eta$, as can be seen from the alternative expression

$$y = \frac{1}{2} \ln \frac{E + p_L c}{E - p_L c}, \tag{1.7}$$

where at high energies $E \approx pc$.

1.4 Ultra-relativistic heavy ion physics

Heavy ion collisions started up with low energies, below 0.1 c. As higher energies have become available, new language terms have arose. We are therefore nowadays talking about both *relativistic* and *ultra-relativistic heavy ion collisions*. Generally the term relativistic is used in experiments when beam energy is about 100 $AMeV$[4], while the term ultra-relativistic is used when energies over 10 $AGeV$ prevail.

The ultra-relativistic regime is reached in e.g. the Alternating Gradient Synchrotron (AGS) at Brookhaven National Laboratory (BNL) in USA and at the Super Proton Synchrotron (SPS) at CERN in Switzerland and France.

I will however refer to both energy ranges as relativistic, and in general not make this distinction.

Models

Heavy ion collisions are often described in the *participant-spectator model* (fig. 1.3).

In this description the distance between the paths of the two colliding nuclei, the *impact parameter* b, is defined at a separation where the nuclei don't interact. In the collision only overlapping nucleons, the participants, interact while the other nucleons, the spectators, fly along almost as if nothing has happened. The participants form a so-called *fireball*. It is in the fireball that the above mentioned quark-gluon plasma eventually can be created.

[4] $AMeV$ is a common notion for $MeV/nucleon$. Also used is AeV, $AkeV$, $AGeV$ etc.

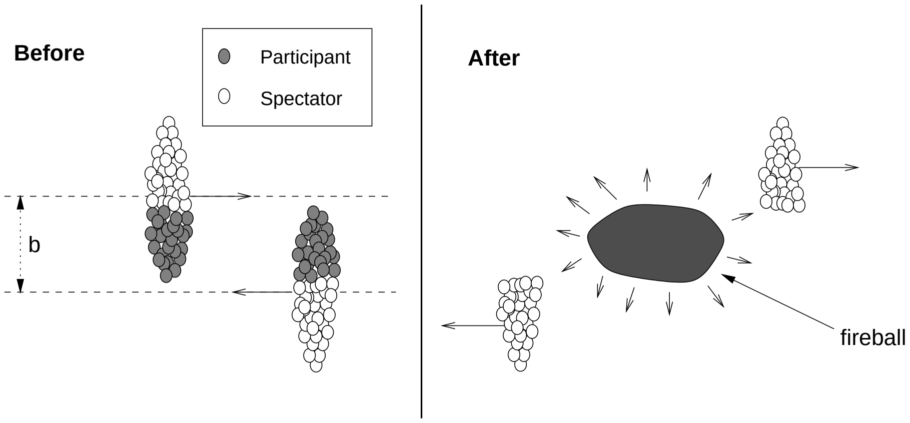

Figure 1.3: *The participant-spectator model.*

In central nuclear collisions the degree to which the nuclei are stopped is important to know. In theory generally two models are used to describe the stopping. These models describe two different energy regimes.

In the low energy regime, with a center of mass energy $\sqrt{s} \approx 5-10\ AGeV$, the *Landau model* is used. This model describes a collision between two contracted nuclei leading to a full coalescence and stopping in the center of mass system (fig. 1.4). The collision has a high baryon density. If a quark-gluon plasma is created in such a collision it will also have a high baryon density.

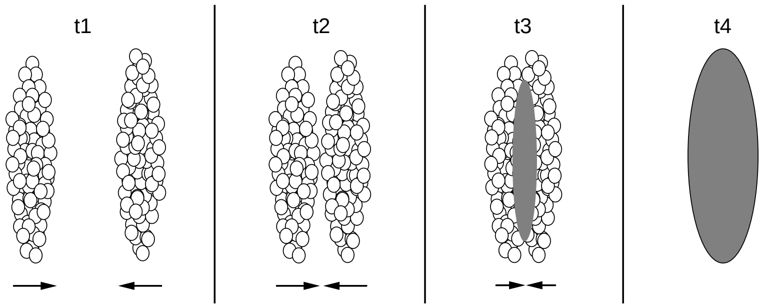

Figure 1.4: *A central nuclear collision in the Landau picture. The two nuclei coalesce and have rapidity $y = 0$ in the center of mass system.*

At higher energies, with center of mass energy above $\sqrt{s} \approx 100\ AGeV$, the *Bjorken model* is assumed to give the best description. In this model the nuclei have so much energy that they will be almost transparent to one another and go through each other instead of stopping (fig. 1.5).

In the wake after the nuclei have passed each other there will be a an exited color field, with high temperature and low baryon density. The quark-gluon plasma can then be produced in the this field.

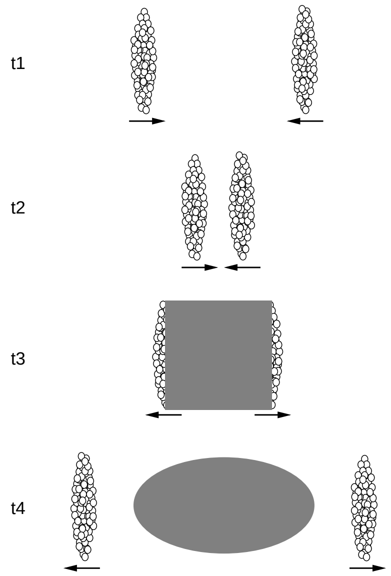

Figure 1.5: *A nuclear collision in the Bjorken picture. A highly exited color field is created in the wake of the two nuclei.*

The conditions prevailing in the Landau picture, with an eventual quark-gluon plasma with high density, resemble the expected conditions in the center of a neutron star. The conditions of the quark-gluon plasma produced according to the Bjorken picture, on the contrary, with low density but high temperature, resemble more closely the calculated conditions from the Big Bang. We should therefore be able to study quark-gluon plasma produced in two ways, out of a dense hadron gas and in an exited color field, if the quark-gluon plasma really exists.

Experimental results

NA49 is a CERN experiment that has performed extensive measurement of stopping of baryons. The stopping can be illustrated with a plot of number of baryons as a functions of rapidity in the center of mass system. In the Landau picture all baryons will be centered closely around mid-rapidity. In the Bjorken picture, on the contrary, there will be very few baryons around mid-rapidity and two rather sharp peaks at the rapidities of projectile and target.

From the NA49 results on fig. 1.6 we see that baryons are smeared out in the entire rapidity interval, with shoulders between maximal (minimal) rapidity and mid-rapidity. The collisions examined by the NA49 collaboration thus makes it necessary to combine the Landau and Bjorken models. In the upcoming experiments at RHIC at BNL and LHC at CERN higher center of mass energies will prevail, and it is therefore expected that the Bjorken model will best describe the stopping of baryons in these experiments.

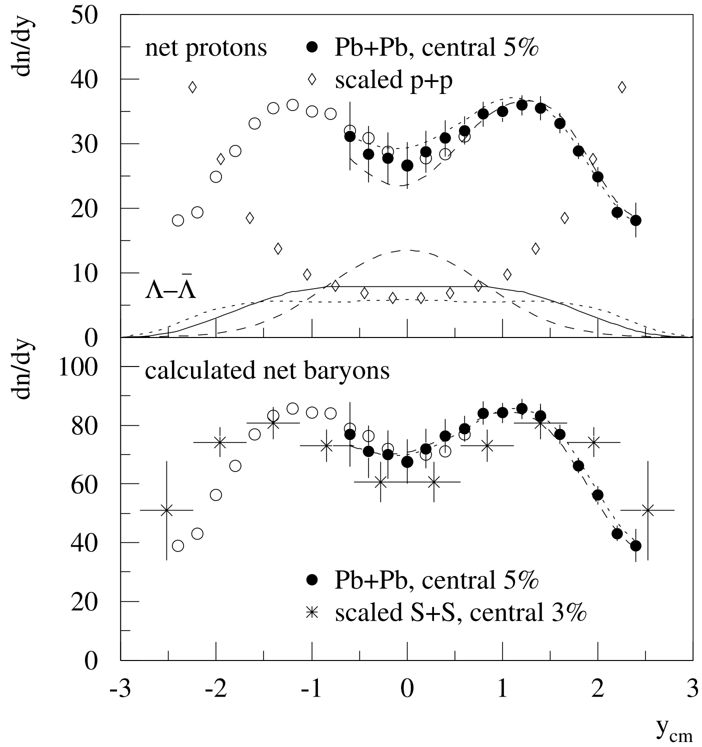

Figure 1.6: *Baryon and proton density as function of rapidity in center of mass frame.* [NA49a]

1.5 Signatures of quark-gluon plasma

Due to the small space-time dimensions of an eventual quark-gluon plasma, freezeout will occur long before it reaches any detector. Only indirect indications from the plasma, so-called *signatures*, can be detected. QCD predicts several different kinds of signatures of a quark-gluon plasma. One signature only would not be enough to support the existence of a quark-gluon plasma. Therefore recent ultra-relativistic experiments aims at detecting several possible signatures.

1.5.1 Thermodynamic variables

As mentioned earlier a rise in the effective number of *degrees of freedom* over a small range in temperature is is expected if a quark-gluon plasma is produced. The number of degrees of freedom can be expressed by ϵ/T^4 or as s/T^3, where ϵ is energy density, s is entropy and T is temperature. The quantities ϵ, s and T can be identified from a relativistic heavy ion experiment with the transverse energy density dE_T/dy, the hadron rapidity density dN/dy and the average transverse momentum $< p_T >$ respectively [Hov82]. The number of degrees of freedom can thus be measured and provide a signature of quark-gluon plasma.

1.5.2 Interferometry - HBT

Known from astronomy is the method developed by Hanbury-Brown and Twiss to measure the radius of a stellar object, typically a distant star. [HBT56]. The method uses the interference pattern from photons, i.e. bosons, emitted from the object to determine its radius. In relativistic heavy ion experiments the same principle can be used to measure transverse radius and lifetime of the fireball, as well as flow patterns in it. Correlations between pairs of identical bosons are therefore investigated. Most often $\pi\pi$-correlations are measured [Gol60], but also kaons have been used.

Several experiments at CERN and BNL have performed extensive two-particle correlations in the past years, using mainly pions and/or kaons. One of these experiments is NA44, where pion and kaon correlations have been studied in collisions systems ranging from p-Pb to Pb-Pb. The radius of the fireball is found to be systematically increasing and is also consistently larger than the projectiles (fig. 1.7).

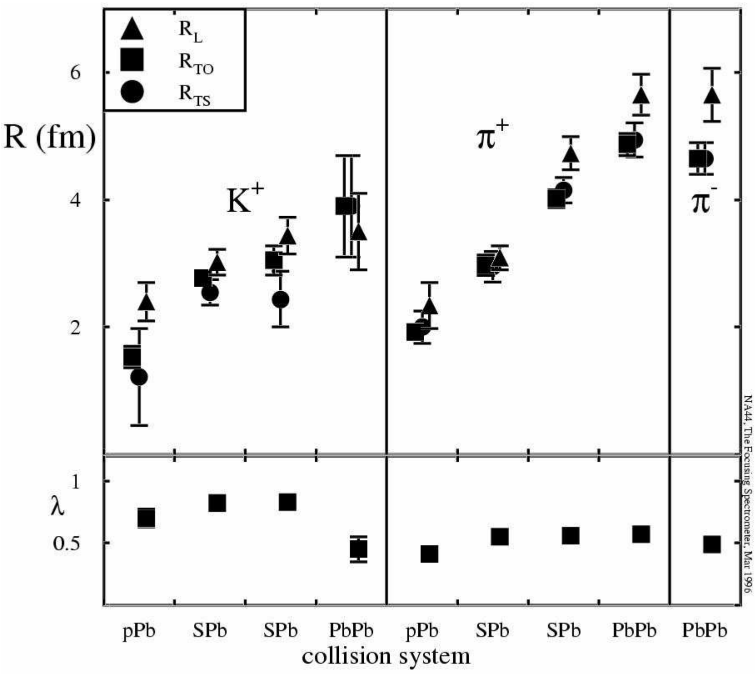

Figure 1.7: *Radius of the fireball as function of collision systems from HBT with* $\pi^{\pm}$ *and* K^{+}*.* [Fra96]

The WA98 collaboration has studied the elliptic emission patterns of π^{+} and K^{+} in semi-central 158 $AGeV$ Pb-Pb collisions at the SPS. The aim of this study is to get insight into the flow patterns prevailing in the fireball. In central collisions radial flow patterns will occur, while elliptic and direct patterns occur in off-central collisions. In these reactions the K^{+} were found to be emitted mostly in a perpendicular direction to the reaction plane, while the π^{+} were emitted in the reaction plane [WA98a]. The results of this measurement indicate that the emission of kaons is subject to some potential within the fireball in addition to the collective flow effects. This result can not be explained by

RQMD[5].

1.5.3 Charmonium suppression

Bound states of charm and anti-charm quarks are generally referred to as *charmonium*. The J/ψ is meson with content $c\bar{c}$ and thus a charmonium. It is predicted that in a collision involving quark-gluon plasma the yield of J/ψ will be suppressed compared to collisions without a plasma [Mat86].

In the early phases of a nuclear collision many new particles will be produced from the available energy. Since baryon number is an absolutely conserved quantity, the new quarks can only be produced in quark-antiquark pairs. The most common ways a J/ψ can be made is through annihilation of other quarks, $q\bar{q} \to c\bar{c}$, or fusion of gluons, $gg \to c\bar{c}$. Most $c\bar{c}$ will be created in the early stages of the collision, as the energy density is highest and the m_c is significantly bigger than m_u and m_d. In a quark-gluon plasma the c and $\bar{c}$ will not be bound and can roam around within the plasma. At the point of freezeout it is less likely that the $c\bar{c}$-pair binds to each other. They can more easily bind to lighter quarks as they outnumber the charmonium, e.g. c binding to either $\bar{u}$ or $\bar{d}$ to form D-mesons, and $\bar{c}$ forming $\bar{D}$ with u or d. Thus we are likely to see an increase in D-mesons and a decrease or suppression in J/ψ.

Also, once the J/ψ is created it has a small probability of dissociating in the soft interactions it will experience through the fireball. It will only be subjected to its own statistical decay.

The lightest D-mesons have a life time of order of 10^{-12} s [PDG98], and the short lifetime makes it very difficult to find out whether detected particles come from decayed D-mesons or from the fireball. One therefore has to measure the decrease in the rate of detected J/ψ-mesons. Other excited bound states of $c\bar{c}$, such as χ_c and ψ', are also detected. Being less bound than J/ψ they dissociate even easier and will be suppressed even more.

Similar behavior as the one for charmonium will probably be seen for heavier systems such as Υ and Υ' being bound $b\bar{b}$-states [Kar91]. However the Υ' is the best candidate as the temperature at which it "melts" is just above the transition temperature T_C, while the one of Υ is about $2.5T_C$.

Another way to understand the charmonium suppression is to look at the screening of color charge, so-called *Debye screening*, within a quark-gluon plasma and compare the binding of a $c\bar{c}$-system in the plasma with the system in normal hadronic matter. The energy of a $q\bar{q}$-system in a hadron gas is given by[6]

$$E(r) = 2m + \frac{1}{2mr^2} + V(r) \tag{1.8}$$

where the potential energy

$$V(r) = \sigma r - \frac{\alpha_s}{r} \tag{1.9}$$

Here m is the mass of the quark, r is the separation distance between q and $\bar{q}$, σ is a string constant approximated to 0.16 GeV^2 at zero temperature, and α_s is the strong

[5]RQMD = Relativistic Quantum Molecular Dynamics

[6]As is often done in such calculations, some constants are left out, i.e. $c = \hbar = 1$.

coupling constant of about 0.5. The first term in the expression for E is the rest energy[7] and the second is kinetic energy.

The *binding radius* of $q\bar{q}$-pair is found by differentiating E with respect to r. With the quark being a c and the antiquark a $\bar{c}$, we try the expression with mass $m = 1.56\ GeV$. This gives a binding radius of $r_{J/\psi} = 0.20\ fm$. Smaller values of α_s and m will result in higher values for $r_{J/\psi}$.

At bigger separation distances the coupling between q and $\bar{q}$ weakens and α_s can therefore be put equal to 0. The expression for the binding radius thus simplifies to

$$r_{J/\psi} = (m\sigma)^{-\frac{1}{3}} \tag{1.10}$$

Substituting the above numerical values gives $r_{J/\psi} = 0.31\ fm$. The radius of a J/ψ at zero temperature is therefore only dependent on the linear term in $V(r)$.

As temperature increases above T_k the string constant σ goes to 0, while the second term in $V(r)$ has to be substituted by its Debye-modified companion. The potential will therefore be given by

$$V(r) = -\frac{\alpha_s}{r} e^{-\frac{r}{r_D}} \tag{1.11}$$

In this expression r_D is the Debye radius which is proportional to the density of color charge. Even in this regime bound states can exist for certain combinations of m, α_s and r_D. By differentiating the total energy E (eq. 1.8) with respect to r, this time with eq. 1.11 as potential, and putting it equal 0, the radius equals $r_{J/\psi} = 1.62 r_D$ Also for other reasonable values of m and α_s we get $r_{J/\psi} > r_D$. The radius of J/ψ being bigger than the Debye-radius means that there will be screening of color charge at temperatures above T_C.

Experimental results

At CERN the NA38 and NA50 collaborations have studied the suppression of charmonium in Pb+Pb collisions at different energies at the SPS. The NA50 collaboration has recently presented results showing clear suppression of J/ψ beyond what can be explained in terms of nuclear absorption of the $c\bar{c}$-pair before it forms the J/ψ state [Kha97]. In fig. 1.8 the suppression is normalized to Drell-Yan[8]. They have estimated the critical energy density at which color charge starts becoming screened to be $\sim 2.3\ GeV/fm^3$ for χ_c and $\sim 3\ GeV/fm^3$ for the more tightly bound J/ψ [NA50]

1.5.4 Strangeness enhancement

Rafaelski and Müller suggested in 1982 that creation of a quark-gluon plasma would lead to an increased outcome of strange particles from the collision [Raf82]. In relativistic heavy ion experiments the beam is made of u and d quarks, so all strange matter detected must have been produced in the collision. Both strange mesons and baryons can be produced. Approximately 70% of the strange particles are kaons, $K^+(u\bar{s})$, $K^-(\bar{u}s)$, $K^0(d\bar{s})$ and $\bar{K}^0(\bar{d}s)$. Strange baryons are also called *hyperons*. Some of the most common hyperons are $\Lambda^0(uds)$, $\Xi^-(dss)$, $\Omega^-(sss)$ and their charge conjugates.

[7] The rest energy E_0 is given by Einstein's famous formula $E_0 = mc^2$, or simply m when $c = 1$.

[8] Drell-Yan is the process where two hadrons collide and create a dilepton.

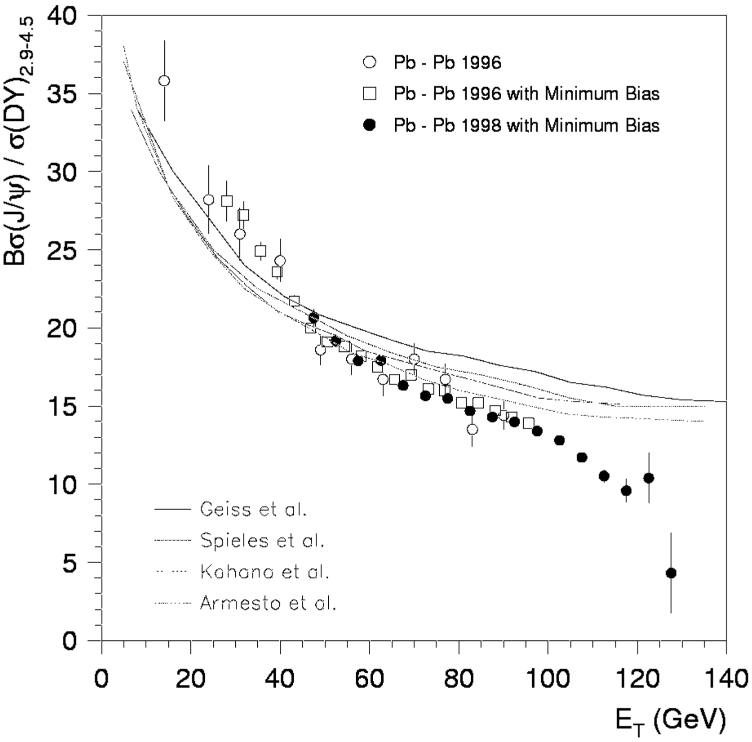

Figure 1.8: *Suppression of J/ψ as function of energy density, normalized to Drell-Yan. The lines indicate conventional calculations of J/ψ suppression based on nuclear absorption.*

When talking about a strange particle, its *strangeness* is an important quantum number. The strangeness, S, of a particle is the number of $\bar{s}$ minus the number of s. Thus $S_{\Lambda^0} = -1$, $S_{\Xi^-} = -2$ and $S_{\Omega^-} = -3$.

There are three ways $s\bar{s}$ can be created in a quark-gluon plasma: 1) quark-antiquark annihilation, 2) gluon fusion and 3) decay of thermal gluon. In a quark-gluon plasma the density of gluons is expected to be very high, especially in the Bjorken picture, and also gluon fusion is a fast process. Therefore the latter two ways of $s\bar{s}$ creation will dominate. The temperature of the plasma will be about the critical temperature, $T_C \sim 150 - 200\ MeV$, which is also by definition the average energy of the particles in it. A gluon fusion will therefore involve $300 - 400\ MeV$ being of similar value as the mass of a $s\bar{s}$-pair ($m_s \sim 150 - 180\ MeV$).

Quarks are fermions and *the Pauli principle* exclude two up or two down quarks from being in the same state. When two nuclei collide, the lower energy states of u and d are therefore rapidly filled. The creation of new $u\bar{u}$ and $d\bar{d}$ will be suppressed by a factor $e^{-\mu_B/3T}$, where μ_B is the *baryo-chemical potential*, an important parameter of the fireball, and T is temperature. Compared to creation of $u\bar{u}$ and $d\bar{d}$, if there was no initial Pauli blocking, the production of $s\bar{s}$ is suppressed by a similar factor $e^{-m_s/T}$ [Løv97]. The two suppression factors are of the same order of magnitude and can therefore lead to similar production rates of $u\bar{u}$, $d\bar{d}$ and $s\bar{s}$.

In a hadron gas strange particles can be created. This however is a more difficult process, especially for baryons. In order to conserve baryon number the creation of a hyperon also includes creation of some other hadron. Therefore the creation of a $\Lambda\bar{\Lambda}$ only takes place if $2 \cdot m_{\Lambda} \approx 2.2\ GeV$ of energy is available. The creation channel $p + n \rightarrow n + K + \Lambda$ need at least $\sim 700\ MeV$ of energy, not including the rest energy of p and n. In a quark-gluon plasma, the creation only "costs" $2m_u + 2m_d + 2m_s \approx 350\ MeV$.

It also takes much longer time on the average to create a hyperon if produced in a hadron gas. The hyperon is usually created in several steps. For the creation of an Ω the following path is typical:

$\pi + \pi \rightarrow N + \bar{N}$, where N is a nucleon

$\pi + N \rightarrow \Lambda + K$

$\Lambda + K \rightarrow \Xi + \pi$

$\Xi + K \rightarrow \Omega + \pi$

The time to make the Ω is on the order of 100 fm/c[9] The time scale for creation of Ω in a quark-gluon plasma is on the order of 1 fm/c, i.e. a factor of 100 smaller. In the QGP picture three strange quarks, that are neighbors in phase space, are frozen out at the same time. For this reason the production rate of hyperons, in particular multi-strange hyperons, may be an important signature of a quark-gluon plasma.

A very sensitive probe of a plasma phase will be strange anti-baryons. The reason is that a quark-gluon plasma will enhance strangeness and rate of anti-baryons. Thus it is expected that the rates of $\bar{\Lambda}$, $\bar{\Xi}^+$ and $\bar{\Omega}^+$ will be highly dependent on the phase of the matter in which they are created.

Experimental results

Enhancement of strangeness in relativistic heavy ion collisions has been studied in several experiments, both at AGS at BNL and at the higher SPS energies at CERN.

Studies of strange meson enhancement has been one of the tasks for the NA49 collaboration. In fixed target experiment at SPS energies they have found a clear increase in K/π for increasing number of participants (fig. 1.9) [NA49b]. They have also investigated the heavier ϕ-meson, which is a $s\bar{s}$-system, and found an even stronger enhancement for this state. The increase in enhancement factor is understandable if the creation of strangeness occurs at quark level and not in a hadron gas.

The yield of strange baryon and antibaryon has also been studied in several CERN experiments. WA85 investigated $p + W$ and $S + W$ collisions at 200 $AGeV/c$, WA94 studied $p + S$ and $S + S$ interactions with the same beam momentum, while WA97 and NA57 have measured the outcome of $p + Be$, $p + Pb$ and $Pb + Pb$ at beam momenta of 40 $AGeV/c$ and 158 $AGeV/c$. From fig. 1.10 it can be seen that the yields of strange baryons and antibaryons have a significant increase for bigger collision systems, i.e. for a higher number of participants in the collision.

From previously mentioned interferometry studies, the lifetime of the fireball in central $Pb + Pb$ at the SPS has been estimated. Current values are around $8 - 10\ fm/c$. This result gives a very strong indication that multi-strange particles such as Ω is produced

[9] fm/c is commonly used a time unit as $1\ fm/c \equiv 10^{-23}\ s$.

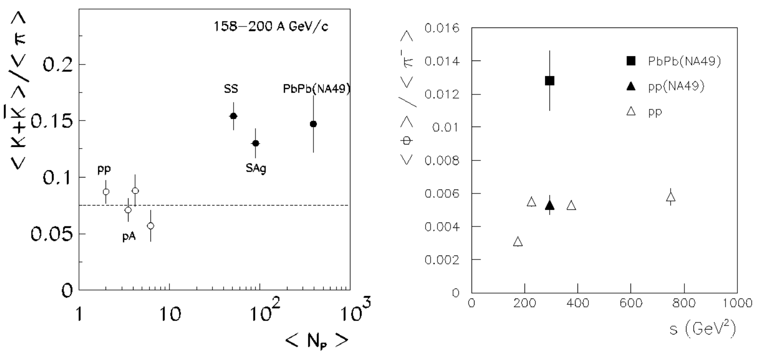

Figure 1.9: *The left panel shows enhancement in K production relative to π as function of number of participants in the collision. In the right panel enhancement of ϕ relative to π^- is shown* [NA49b].

in a new state of matter. The lifetime of the fireball is simply not long enough that the multi-strange particles can be produced in several steps as they would be in a hadron gas.

1.5.5 Electromagnetic probes

The conditions prevailing in the fireball will in any case, whether a quark-gluon plasma is produced or not, imply strong interaction among particles bearing color charge. Particles without color coming from the collision are therefore very interesting, as they can penetrate the fireball from their point of creation without any major interaction. They can provide profound information about conditions in the fireball that is unavailable from detected hadrons, and are referred to as *direct* signatures. The electromagnetic probes include both photons and leptons and may provide a measure of the thermal radiation of the quark-gluon plasma if a region of photon energy or lepton pair invariant mass can be identified from the energy or mass spectra.

There is definitely an "if" to this signature, as there will be a huge background from electromagnetic decays of hadrons and resonances and from bremsstrahlung. It has been anticipated that there will be a window in the invariant mass range around $1-1.5\ GeV/c^2$ where lepton pairs from the quark-gluon plasma can be identified [Ruu91]. Also in the $5-10\ GeV/c^2$ region there may be an opening, but between these intervals the Drell-Yan process from later stages will dominate and probably surpass the thermal outcome in lepton pairs.

Below $1\ GeV/c^2$ down to $0.5\ GeV/c^2$ lepton pairs from decayed hadrons are expected to dominate, which may be a signature in itself. It is anticipated that the width and position of peaks in the lepton pair invariant mass spectra of ρ, ω and ϕ is sensitive to changes in mass spectra of hadronic matter induced in the medium. A *partial chiral symmetry restauration* is presumed to follow the production of quark-gluon plasma. This will lead to a decrease in quark masses, influencing on the mass spectra of the above mentioned particles. E.g. a double ϕ peak will then be a good indication of a long-lived mixed phase [Har98]. Also smearing of the mass peaks will be possible.

The ρ-meson has a lifetime of $\tau_\rho \approx 1\ fm/c$, roughly half the lifetime of the ω-meson.

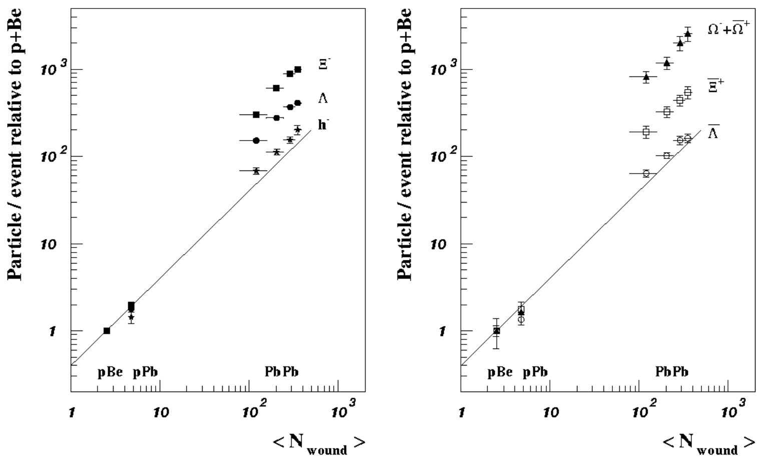

Figure 1.10: *Increase in production of strange baryons relative to the yields in* $p + Be$ *as function of participants.* h^- *is the yield of negatively charged particles* [Ant00].

If the lifetime of the fireball exceeds τ_ρ, then the relative number of ρ in the lepton pair mass spectrum is expected to increase compared to ω. Thus by measuring ρ/ω one has a way to measure the lifetime of the fireball [Hei91].

Direct photons have three main creation channels. They can be created from the annihilation of a quark and an antiquark, $q\bar{q} \to \gamma\gamma$, by interaction between a gluon and a quark, $qg \to q\gamma$, or by interaction between a gluon and an antiquark, $\bar{q}g \to \bar{q}\gamma$. By taking the energy spectrum of the direct photons one should be able to deduce a lot about the thermodynamic conditions in the plasma.

The lepton pairs, or *dileptons* as they are often called, are mainly created in quark-antiquark annihilation processes, $q\bar{q} \to l^+l^-$. Here l^- is a lepton and l^+ its corresponding antilepton, such that total lepton family numbers also after the collision equals 0 ($L_e = L_\mu = L_\tau = 0$).

Experimental results

Several experiments, especially at CERN, have done or are doing measurements on direct photons. So far systematic errors have been to big to give any clear indication of direct photon outcome from the collision. The WA80 experiment has found an excess in the photon distribution of 5.0% of the total photon outcome in the p_T range of 0.5 GeV/c – 2.5 GeV/c. This excess can not be ascribed to decays [WA80]. The collision system is $S + S$ at 200 $AGeV$. But the errors are rather high. It is also possible that high enough energies have not been reached. Temporary results from the WA98 experiment also give an excess, maybe as high as 20%, but more analysis remains on these data.

Future experiments are putting efforts into detecting possible electromagnetic signatures. The PHENIX experiment at RHIC will with use of electromagnetic calorimeter and muon tracking chambers and identifiers look for direct photons and leptons [PhWWW]. Also the ALICE experiment at LHC, CERN, will have a detector dedicated to look for direct photons. This detector is called PHOS (*PHO*ton *S*pectrometer) [Ali99].

1.5.6 Transverse momentum of neutral pions

In a quark-gluon plasma the *partons*[10] will experience a greater specific energy loss than they would in a hadron gas [Guy94]. For this reason the transverse momentum distribution will show an increase for lower values of p_T and a corresponding decrease at high p_T. This process is called *jet quenching.* The WA98 experiment at CERN has measured transverse momentum over a wide range, but so far without being able to conclude that jet quenching has been seen [WA98b]

1.5.7 Exotic signals

In the hadronization stage it may be possible that groups of quarks that are neighbors in phase space and have more than three members can freeze out together. This could lead to strange particles with baryon number higher than 1. Such particles are referred to as *strangelets.* One particle that has been mentioned and looked for is the $H(uuddss)$ with baryon number $B_H = 2$. It should be possible to detect this particle through its decay to two Λs. Strangelets have been looked for in AGS and SPS experiments, but no luck so far.

Strangelets are, if they exist, of great interest in cosmology. The may explain some of the matter in the universe that so far has not been seen, known as dark matter.

1.5.8 Disoriented Chiral Condensates

In relativistic heavy ion collisions the partons are deconfined and as a result their effective mass decreases. This has earlier been referred to as a consequence of partial chiral symmetry restauration. The symmetry is subsequently broken, with as result possibly domains of *disoriented chiral condensates (DCC)* [Bjo92]. DCC implies a coherent excitation of the pion field in certain regions of the fireball, resulting in fluctuations in the ratio between neutral and charged pions. The WA98 experiment has searched for DCC in 158 $AGeV$ Pb+Pb collisions at the SPS, but no large fluctuations have been observed [WA98c]. Only an upper limit on the frequency of DCC production has been established.

1.6 Experimental results and existence of QGP

The past years has given new and profound insight into the evolution of a relativistic nuclear collision. In SPS collisions energy densities of $(3.2 \pm 0.3)\ GeV/fm^3$ have been reached [Hei00], i.e. above the critical energy density for creation QGP found in theoretical calculations. As mentioned already several possible signatures of a quark-gluon plasma have been seen at SPS and AGS experiments, including J/ψ suppression, strangeness enhancement, limits on the lifetime of the fireball, emission of kaons out of the reaction plane, to mention some of them.

These results lead to a seminar at CERN on February 10^{th} 2000 having as title: *A new state of matter: Results from the CERN Lead-Beam Programme.* This seminar

[10] A parton is a particle with strong charge, i.e. a quark or a gluon.

concluded on the basis of available data that a new state of matter has been created [CER00]. However, it was not concluded that this new state of matter is identical to what theoriticians call QGP. More research is necessary to eventually make this conclusion. The expectations to what can be found in experiments at RHIC and LHC are therefore very high.

In June 2000 (presumably) the Relativistic Heavy Ion Collider (RHIC) at BNL will start up with gold beams. At six points on the ring Au+Au collision of 100 $AGeV$ in the center of mass will occur. The luminosity will be on the order of $10^{26}\ cm^{-2}s^{-1}$. Four heavy ion experiments placed along RHIC will start taking data at this point. The PHENIX experiment will mainly focus on detection of electromagnetic signals. STAR is the major tracking device at RHIC, able to perform tracking at high multiplicities. PHOBOS, one of the smaller RHIC experiments will in particular look fore rare signatures by examining a very large number of collisions at low p_T. The last heavy ion experiment at RHIC is BRAHMS, that will be presented in length in the next chapter. RHIC also has a fifth experiment called pp2pp. This experiment will study proton-proton elastic scattering at a later stage with polarized proton beams in the RHIC.

At CERN another great facility for heavy ion experiments is being prepared. This new collider is called LHC, Large Hadron Collider. It will be used for acceleration of protons as well as lead nuclei. During heavy ion runs Pb+Pb collision will give a center of mass energy of $\sim 5.5\ TeV$ per nucleon pair. One experiment at the LHC is dedicated to heavy ion collisions. It is named ALICE (A Large Ion Collider Experiment). When LHC starts up around 2005 ALICE will study both hadronic and electromagnetic signatures.

Chapter 2

The BRAHMS experiment

At Brookhaven National Laboratory (BNL) a new heavy ion collider is in its final preparations. According to the current schedule (March 2000) the physics run will start up in May this year. When running in heavy ion mode four experiments will measure the outcome of the collisions. One of these experiments is BRAHMS, or *B*road *RA*nge *H*adron *M*agnetic *S*pectrometers experiment at RHIC. The BRAHMS experiment will be presented thoroughly in this chapter. But first a look at the collider itself.

2.1 The Relativistic Heavy Ion Collider (RHIC)

In 1983 a colliding beam accelerator project at BNL called ISABELLE was abandoned. This was going to be a $p-p$ collider making it possible to reach $\sqrt{s} = 800\ GeV$. At that time a 3.8 km circular tunnel had been built for the collider. This tunnel and other ISABELLE infrastructure are now being used for the new RHIC collider and its experiments..

RHIC is going to be a versatile collider in the sense that a wide range of nuclei can be accelerated. In the first run period $Au-Au$ collisions will be studied, but RHIC will be able to accelerate nuclei in the whole range from gold down to single protons.

The collider has two separate rings, called the *blue* and the *yellow rings*, where nuclei are accelerated in opposite directions. It will therefore also be possible to study non-symmetric collision, e.g. proton on gold. Possibly in later upgrades RHIC will be able to accelerate nuclei heavier than gold, such as uranium.

RHIC is connected to other accelerators already present at BNL. Nuclei are accelerated in several steps, and at the final stage they reach RHIC. Gold nuclei start up in a Tandem Van de Graf accelerator (fig. 2.1) In the case of Au, ions of charge $Q = -1(e)$ are accelerated from ground potential to 15 MV [RDM98]. Reaching the high voltage terminal they pass a stripping foil liberating the ions of electrons. The number of electrons depend on the element, and Au loose on the average 12 electrons. After further acceleration the ions leave the Van de Graf through a new stripping target giving Au ions charge $Q = +32$. The ions have at this point an energy of $\sim 1\ AMeV$ stacked in pulses of $700\mu s$ or $\sim 4.5 \cdot 10^9$ ions.

The ions are lead through the heavy ion transfer line (HITL) passing AGS to the Booster, a smaller synchrotron. In the Booster the ions are further stacked into eight

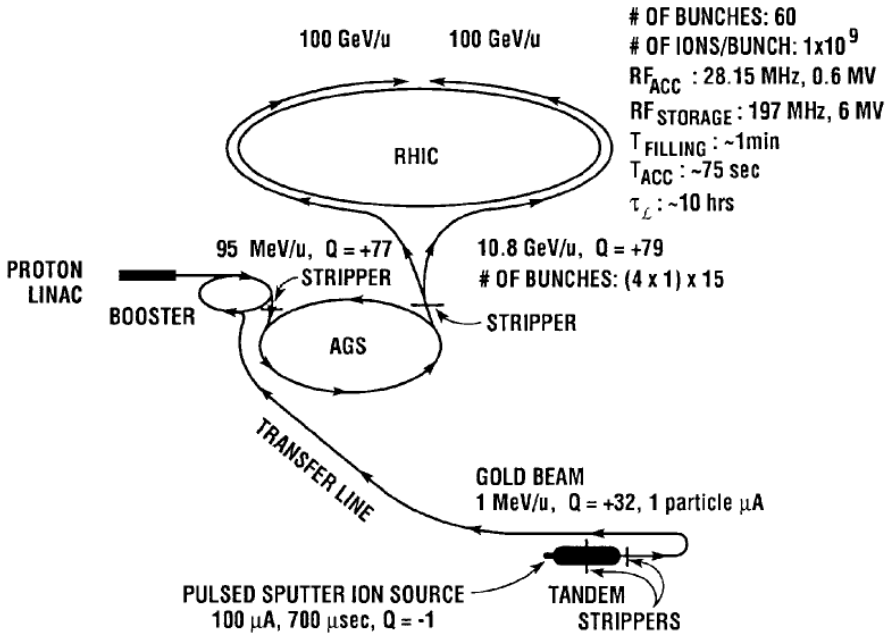

Figure 2.1: *The heavy ions are accelerated at several steps prior to entering RHIC* [RDM98]

bunches with an efficiency of about 50%. That means that $\sim 2.2 \cdot 10^9$ ions are lost at this stage. Upon leaving the Booster the ions have reached a kinetic energy of 95 $AMeV$. The eight bunches are merged into four, and in further stripping in the Booster-to-AGS transfer line (BtA) the ions get a charge $Q = +77$.

Four Tandem/Booster cycles are needed to fill up the AGS. In AGS follows two steps of alternating acceleration and stacking, giving at the end four bunches with kinetic energy of 10.8 $AGeV$. The bunches are then extracted into the AGS-to-RHIC transfer line (AtR), in the beginning of which stripping of the remaining two electrons takes place. In AtR the beam is split to go into either the blue or the yellow ring.

At the end the bunches reach RHIC. In each of the two rings of RHIC there will be 57 bunches. This means that the AGS cycle has to be repeated 60 times, which requires a total of about one minute. In RHIC the ions are accelerated to their max energy of 100 $AGeV$ in about 75 s. When RHIC is loaded and at nominal beam energy, the beam has a lifetime of about ten hours before the whole process of filling and acceleration has to be repeated. Each bunch has $5 \cdot 10^8 - 10^9$ ions. The bunch spacing will be 213 ns.

As mentioned the design of RHIC will also allow acceleration of lighter nuclei. It will typically be able to reach energies of 125 GeV with silicon and oxygen nuclei and 250 GeV with proton beam. One will therefore be able to perform experiments in the entire range from p to Au without gaps.

At six points along RHIC the two beams will cross. At four of these points there are detector systems to register the outcome of heavy ion collisions. One of these detector systems or experiments is BRAHMS.

2.2 BRAHMS detector setup

The BRAHMS experiment is prepared and will be manned by a collaboration of about 50 people from 12 institutions in Europe and the USA. It is situated at the two-o'clock collision point on the RHIC. The dimensions of the experiment and the number of people in the collaboration makes BRAHMS one of the small experiments at BNL.

2.2.1 Two spectrometers

The design of the experiment is based on the measurements to be performed. BRAHMS will measure inclusive and semi-inclusive $p^{\pm}$, $\pi^{\pm}$ and $K^{\pm}$ spectra in the pseudorapidity range $0 \leq \eta \leq 4$ [CDR95]. This range is equivalent to an interval in scattering angle in the lab frame of $2° \leq \theta \leq 90°$.

For this reason the setup has been divided into two rotatable spectrometers or arms, the *forward spectrometer* covering scattering angles from 2.3° to 30° and the *mid-rapidity spectrometer* covering from 30° to 90°. The two arms have a common vertical axis at the nominal collision point (fig. 2.2), and can be positioned to better than 1 mm at the level of the spectrometers. The different labeled components will be explained and described in the following sections.

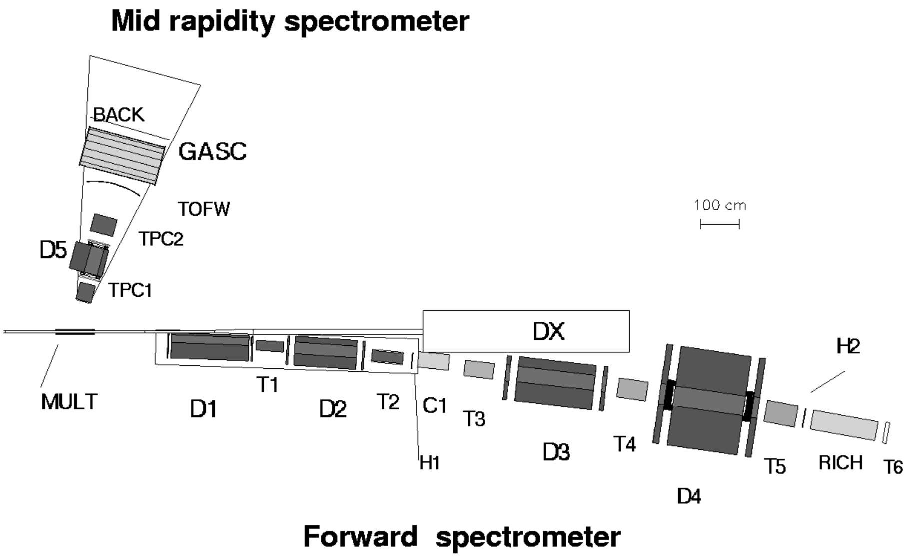

Figure 2.2: *The BRAHMS detector setup as it will be installed in the experimental hall. (DX is a beam focusing magnet and thus not part of the BRAHMS setup.)*

Each spectrometer has tracking and particle identification detectors, as well as magnets. The mid-rapidity arm will be able to measure momenta and identify particles with momentum up to 5 GeV/c, while the forward arm can measure as high as ~ 25 GeV/c.

Furthermore the forward arm is divided into two parts, a front section close to the interaction vertex and a rear section farther away. The division is between detectors C1 and T3. Each section can rotate with axis at the interaction point, but the front section can reach a larger angle than the rear section. There are two main reasons for dividing the forward arm. One is that the front section can identify particle and measure momenta up to $\sim 6\ GeV/c$, i.e. the upper part of scattering angle range of the forward arm. Thus the rear section is not needed for this momentum regime. Secondly the geometry of the interaction hall is such that there is not enough space to move the whole forward arm out to more than $\theta \approx 20°$.

With this detector setup BRAHMS will be able to measure and identify particles in a wide range of rapidity and transverse momenta, as can be seen from the geometric acceptance plots in fig. 2.3. This is one strength of BRAHMS compared to the other RHIC experiments that have lower acceptances both in y and p_T.

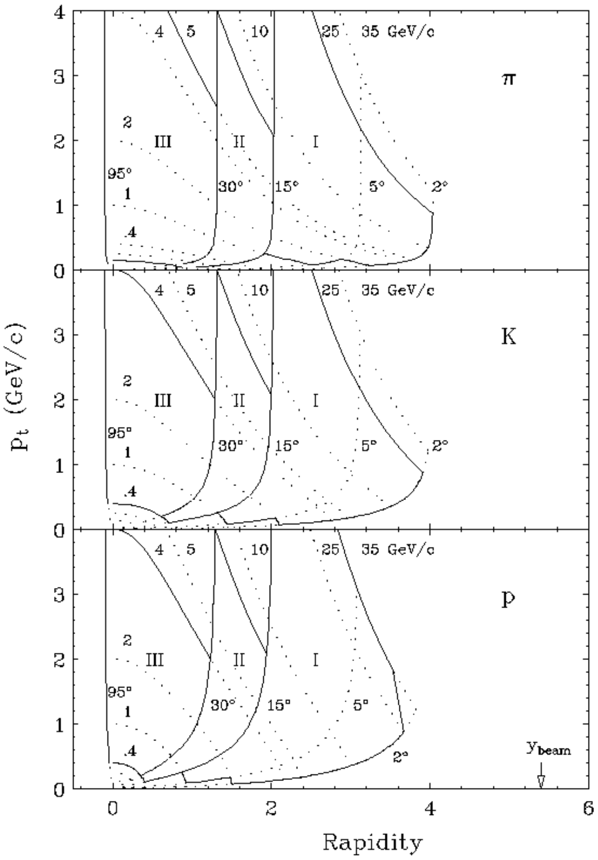

Figure 2.3: *Estimated geometric acceptance of BRAHMS for pions, kaons and protons as function of rapidity and transverse momentum. Region I is with use of the full forward arm, II with only the front section of the forward arm, and III with the mid-rapidity spectrometer.* [CDR95]

2.2.2 Magnets

The detector setup in BRAHMS involves 5 magnets, named D1 through D5. These are all dipole magnets, the bulk mainly made of iron with copper coil and epoxy/glass insulation.

The magnets are used to bend the trajectory of charged particles and are necessary in order to determine their momenta. Several parameters have had to be taken into account when deciding the design of the magnets. Angular acceptance at a given angle mainly controls the horizontal and vertical gaps of the magnets, while the momentum resolution is dependent upon $B \cdot dl$ integrated over the length of the dipoles.

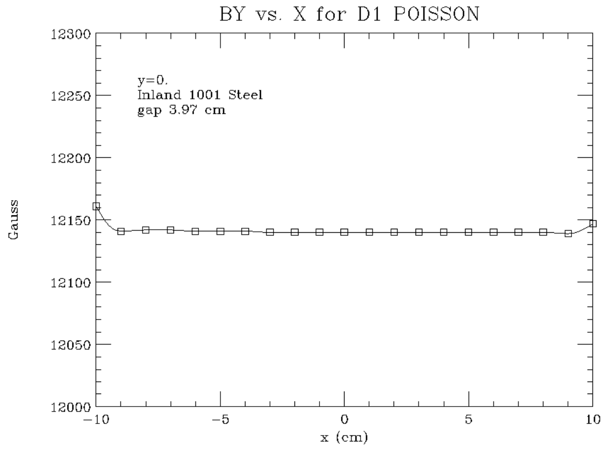

Figure 2.4: *Simulated magnetic field in the aperture of D1 using POISSON. (*$1 Gauss = 10^{-4}$ *T)* [CDR95]

The magnet design is of window frame type. In simulations using the program POISSON this yields a good uniform field in the opening (fig. 2.4) and small fringe field on the outside. In the aperture the magnets typically have a field of $B = 1.2\ T$, and the vertical fringe field component on the collider beam from D1, which is the magnet closest to the beam, has in simulations been calculated to about $7 \cdot 10^{-4}\ T$ [CDR95].

D1 and D2 are mounted on the front section of the forward arm. In addition to rotating around the collision point with the front section, D2, T2, H1 and C1 can be offset relative to the axis of D1. This feature will allow the forward arm to measure smaller momenta, since a low momentum particle will be more deflected in D1 and would not go through D2 if it was not rotated. Typically, in order to measure particles with momenta $p = 2 - 5\ GeV/c$ D2 and its assiciated detectors will be rotated 5° relative to D1.

2.3 Tracking

Several of BRAHMS' detectors are dedicated to tracking, i.e. to reconstruction of the trajectory of a particle through the spectrometer. In the forward arm the tracking detectors are named T1 through T5. T1 and T2 are *time projection chambers* (TPCs), that are more thoroughly dealt with in the next chapter. T3, T4 and T5 are *drift chambers*. The mid-rapidity arm has two TPCs, called TPC1 and TPC2.

Every drift chamber in BRAHMS has three modules, that for each chamber is identical. Also, T4 and T5 are identical, with active measures of $50 \cdot 35\ cm^2$ (width · height), while

T3 measures $40 \cdot 30\ cm^2$. The drift chambers are placed 4 m apart. A module in T3 has 10 detection planes, the modules placed 25.5 cm apart along the intrinsic z-coordinate. The modules in T4 and T5, on the other hand, have 8 planes, and there is a 22.5 cm separation between the modules. T3 is thus longer than T4 and T5. The drift chambers use a gas mixture of 67% Ar, 30% Isobutane and 3% alcohol. A resolution for the drift chambers less than 250 μm is expected. More general features of drift chambers is presented in the next chapter.

Each tracking detector gives several space-points. From the space-points the trajectory of the particle through the detector can be reconstructed. This is done by computers, and referred to as *local tracking*. Outside the magnets charged particles follow straight lines, while they inside magnets are bent due to the strong magnetic field. By extrapolation the different track segments from each detector can be fitted together so as to give a track of the particle through the entire spectrometer. This is called *global tracking* and thus determines the primary collision point. From the deflection of the track in magnets the momentum can be estimated.

2.3.1 The forward spectrometer

The tracking detectors in the forward spectrometer will measure over a large range in momentum. To accomplish this the forward spectrometer will operate in two modes, one for low and one for high momentum.

In the low momentum mode tracking is done in the front section of the arm. The particles are traced in T1 and T2, and the momentum estimated from the deflection of the trajectory through D2. Extrapolation through D1 gives the primary interaction point. The forward spectrometer can run in low momentum mode in its whole angular range.

To measure higher momenta the entire forward spectrometer has to be used. Dipoles D1 and D2 sweep particles in the forward direction towards the rear part of the spectrometer, where T3, T4 and T5 do the tracking. The momentum of the particles is estimated from the deflection their trajectories get when going through D3 and D4. The particles are then traced back to T2, and by extrapolating back toward the primary interaction point it can be decided whether the particles originate from the primary or from secondary interactions. In this mode hits in T2 are required but not in T1. The forward arm can only run in high momentum mode in the angle range of the rear section of the arm.

High accuracy measurements is of paramount importance. The accuracy in position determination in the tracking detectors is a major factor in the resolution of global tracking. In order to achieve the desired resolution of mm for the collision vertex, the tracking detectors have to give positions to better than 300 μm.

Multiple scatterings as particles go through air and other gases in the spectrometer is bound to occur and will deflect the particles somewhat. However, for high momentum particles multiple scattering gives only a minor contribution to uncertainty. It has been estimated that for particles going through 4 m of air with momenta above 2 GeV/c the contribution from multiple scattering is less than 1 mm [CDR95].

The momentum resolution depends upon both accuracy in determination of space-points in the tracking detector and $B \cdot dl$ integrated over the length of the magnets used in momentum determination. From simulations with GEANT with 10 GeV/c pions emitted from the interaction point, and with nominal magnetic fields and position resolution in the tracking detectors, momentum resolution on the order of 1% are typical.

Also important for the design of the detectors is the expected multiplicity. Close to the interaction point a high multiplicity is expected in central $Au - Au$ collisions. From GEANT simulations it has been estimated that T1 may have to cope with densities on the order of 0.2 $particles/cm^2$, while T2 will be down at 0.05 $particles/cm^2$ on the average. T3-T5 being farther from the interaction vertex will experience even lower multiplicities. High multiplicity has therefore been an important factor in designing the TPCs and also in the development of software to translate the ADC signal from the detectors to space-points.

The particles detected are not all coming from the primary interaction. Some are results of multiple scattering in gas, as previously mentioned. Also some particles emerge from scattering in magnets and detectors. Simulations have shown that T3 is likely to get a large background. The major contribution to this background is particles going through the first part of the forward spectrometer scattering off the beam magnet DX. Furthermore, T2 will be used in both low and high momentum mode, and it is therefore important in the overall tracking. The lowest possible background is thus desirable. It is possible to shield off some of the background, and in the initial setup T1 and T2 has lead shielding on the sides facing the beam pipe.

2.3.2 The mid-rapidity spectrometer

In the range of the mid-rapidity spectrometer the momenta of the particles will be lower, but the multiplicities will generally be higher. This represents a compromise in the design of the spectrometer. Due to the low momentum it is desirable to have the tracking detectors as close to the interaction point as possible. But also should the detectors cope with high multiplicity, which for the TPC should not exceed 0.3 $particles/cm^2$. TPC1 has therefore been placed at 90 cm from the nominal interaction point. TPC2 being placed further back is far from reaching its limit in multiplicity.

The highest multiplicity will occur at small angles. This is the reason why in $Au - Au$ collisions the mid-rapidity arm will not rotate below 30°. For lighter beams it will be able to cover down to 20°.

Between the two TPCs dipole magnet D5 will be placed, operating with a magnetic field up to 1.0 T. The momentum of the particles will be determined also in the mid-rapidity spectrometer from the deflection of the particle tracks when going through the magnet. In order to lower the energy loss of low momentum particles when going through D5, the magnet may be installed with a helium bag inside its aperture.

In general, wherever possible the same technology is used in the forward and the mid-rapidity spectrometer. By using similar technology comparison of results from the two arms will be easier. Since the spectrometers will be able to overlap at 30°, one will be able to search for systematic differences in performance, which should be as small as possible.

2.4 Particle identification

Both spectrometers in BRAHMS will do particle identification (PID), and as with tracking the techniques used in either of them are of similar kind. In both arms time-of-flight hodoscopes and Čerenkov detectors will be used. The hodoscopes will do the low momentum part, while different Čerenkov solutions are used for high momentum particles. With such a combination of detectors particle identification in wide ranges in y and p_T is possible.

2.4.1 The forward spectrometer

The forward arm has four detectors for particle identification. It has two hodoscopes called H1 and H2, a segmented Čerenkov detector, C1, and a ring-imaging Čerenkov detector, RICH.

The hodoscopes are arrays of vertical staves of scintillating material, with fast photo-multiplication tubes (PMTs) at the ends for read out. H1 has 40 staves of $1 \cdot 1 \cdot 25\ cm^3$, while H2 has 16 staves of $1.5 \cdot 3 \cdot 40\ cm^3$. In the case of the BRAHMS experiment both time and pulse height information will be read out from the hodoscopes. The PMTs and scintillating staves have been tested for accuracy and have proved to give time signals to better than 75 ps. H1 and H2 are situated 9 and 19.5 m from the interaction vertex respectively.

Right behind H1 the first Čerenkov detector, C1, is situated. This segmented Čerenkov detector uses C_4F_{10} at 1 $atm.$ pressure as radiator gas. When a particle goes through C1 with velocity higher than the speed of light in the gas, Čerenkov radiation characteristic for the particle and its energy will be emitted. C1 will be read out with 32 photo-multipliers.

Almost at the end of the forward arm the RICH will be situated. In this detector the radius of the Čerenkov wave emitted by a traversing particle will give the particles ID. The RICH will be filled with a mixture of C_4F_{10} and C_5F_{12} at a pressure of 1.0 $atm.$ Radiation emitted by the incoming particle will be reflected in a focusing mirror and read out with in 4 sections, as shown in fig. 2.5. Each section has 20 photo-multipliers that each reads out 2×2 pixels. Every pixel has a cross section of 0.8 cm^2. This arrangement gives a total of 320 pixels for read out from the RICH.

In a similar manner as with tracking, the forward spectrometer will do PID in two different modes depending upon momentum. In low momentum mode particles will be identified in the front section of the forward arm. H1 will be able to do π/K up to 3.3 GeV/c and K/p up to 5.7 GeV/c, i.e. when a separation of 4σ is required, ($\sigma = 75\ ps$). C1 will handle π/K up to 9 GeV/c, but not K/p between 5.7 and 9 GeV/c. In the separation of K and p there will therefore be a gap in this range when running in low momentum mode.

Going to higher momenta and high momentum mode, the rear section will do the task. H2 can do π/K up to 5.0 GeV/c and K/p up to 5.7 GeV/c with 4σ cut. The RICH will be able to separate π, K and p up to 30 GeV/c.

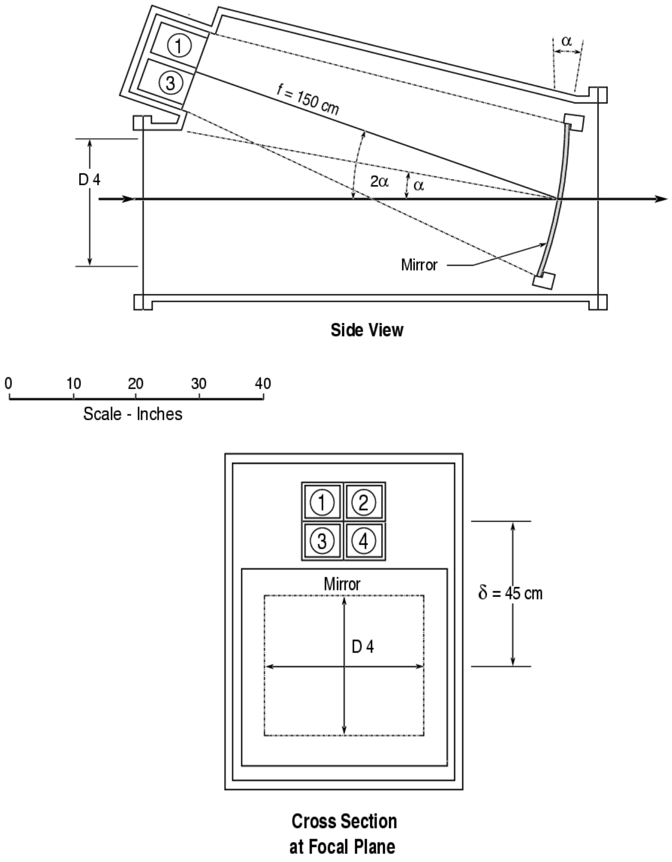

Figure 2.5: *A sketch of the RICH detector in the forward spectrometer of BRAHMS* [CDR95]

2.4.2 The mid-rapidity spectrometer

In the mid-rapidity spectrometer there are two PID detectors. The low momentum particles are identified in a time-of-flight wall, TOFW. The TOFW can identify π/K up to 2.2 GeV/c and K/p up to 3.7 GeV/c, i.e. with 4σ separation. Higher momentum particles are identified in the segmented threshold Čerenkov detector, GASC. In this detector pions with momentum up to 5 GeV/c, kaons up to 3.7 GeV/c and protons up to 11 GeV/c can be identified. A summary of BRAHMS ability to identify pions in the mid-rapidity and forward arm is presented in fig. 2.6, and a summary for kaon and proton ID in fig. 2.7.

The time-of-flight wall is situated 4.35 m away from the interaction point. The wall is made of scintillator segments, each segment 22 cm high and with a cross section of $1.27 \cdot 1.3\ cm^2$. In the initial setup of BRAHMS there is 84 scintillating slats, but more slats will be added to regions with high background at a later stage.

The GASC detector is to be placed behind the TOFW. However, this detector was not part of the initial funding of the experiment and will not be included until later. Therefore the mid-rapidity spectrometer will not be able to measure the higher momenta

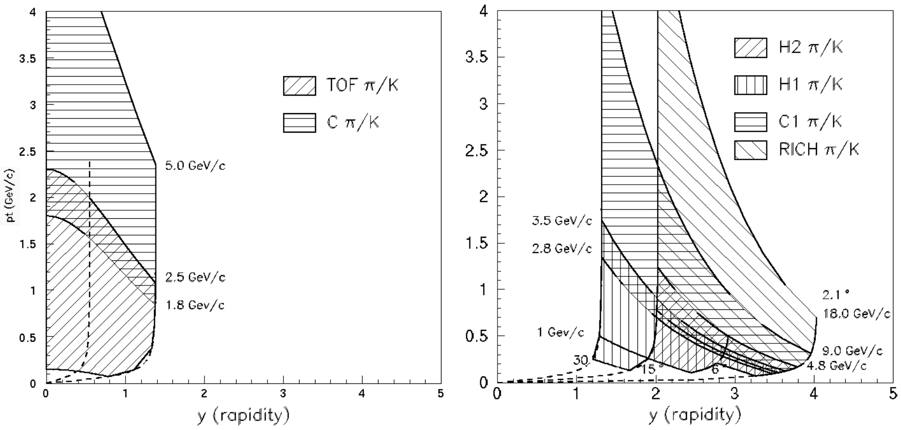

Figure 2.6: *Acceptance in identification of pions in the mid-rapidity spectrometer (left) and the forward spectrometer (right)* [CDR95]

within its acceptance interval. If the GASC which is currently on the drawing board it to be built, it will be filled with Freon-12 gas at a pressure of 4 *atm*.

2.5 Global detectors

In addition to tracking and particle identification detectors the BRAHMS setup includes some global detectors. The global detectors include beam-beam counters, centrality detector and zero-degree calorimeters. These detectors characterize the events and provide low level hardware triggers. The centrality detector measures multiplicity few centimeters away from the primary interaction vertex. The beam-beam counters will provide start-signal for the hodoscopes, as well as for TPCs and drift chambers, and also measure the position of the collision vertex to 1 *cm*. The zero-degree calorimeters (ZDCs) will measure the longitudinal energy of spectator neutrons.

2.5.1 Centrality detector

Surrounding the beam vertex a centrality or multiplicity detector (MULT on fig. 2.2) will be placed. Its main task will be to determine the multiplicity of each event and to provide a first level trigger to the other detectors. The multiplicity of an event is directly correlated to the impact parameter, i.e. the centrality of the collision. In addition this detector will provide an estimate of the number of charged particles per unit pseudorapidity, $dN/d\eta$, which will be used to find out which theoretical model that best describes the collision scenario.

The centrality detector is a hybrid in the sense that it is made of both plastic scintillating tiles and wafers of silicon strips. The above mentioned tasks are shared such that scintillating tiles will provide a fast signal for event selection, while the Si strip detectors will record data for off-line determination of multiplicity and $dN/d\eta$. The scintillating tiles and Si wafers are placed in a two layer structure as can be seen on fig. 2.8.

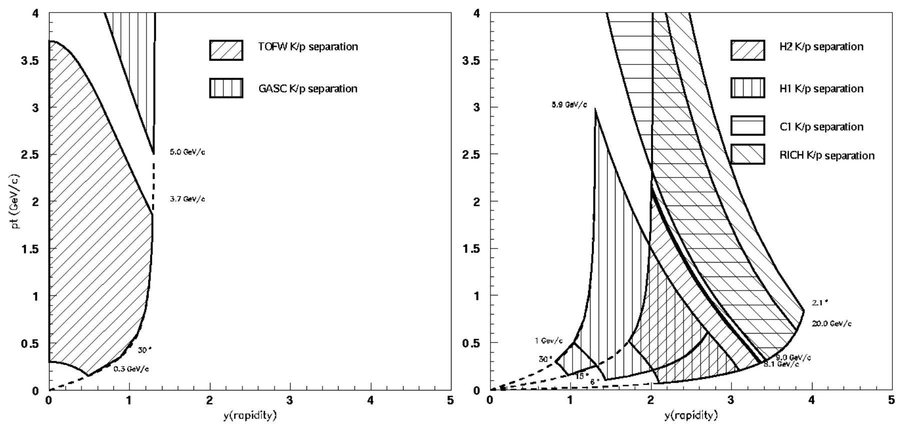

Figure 2.7: *Acceptance in identification of kaons and protons in the mid-rapidity spectrometer (left) and the forward spectrometer (right)* [CDR95]

Each of the 5 rows of strip detectors has 6 wafers, measuring 6 $cm \cdot 4\ cm \cdot 300\ \mu m$. Every wafer has 7 strips, giving a total of 42 bins in η. The wafers are placed at 4 cm from the center of the beam pipe. The read-out chain for the Si strips includes preamplifiers and shapers, placed between the scintillating tiles.

The ladders of plastic tiles has 8 tiles each, thus resulting in 8 bins of η and a total of 40 tiles. The tiles are quadratic with sides of 12 cm and 5 mm thick, and the radius of the barrel is 11 cm. In the initial setup tiles covering the same interval in η are read out with the same photomultiplier, but read-out may be refined at a later stage to have one channel per tile. Signals from the tiles are lead in fiber-optic conductors to photomultipliers placed above and below the barrel. With this setup event selection within 250 ns is expected.

The inner barrel of Si wafers has a length of 40 cm, while the outer tile barrel has a lengh of 99 cm. A range in pseudo-rapidity of $-2.2 < \eta < 2.2$ will be covered with this geometry. From simulations it is expected multiplicities as high as 200 particles per tile per event.

2.5.2 Beam-beam counters

At 2.25 m from the nominal beam vertex the two beam-beam counters will be placed, one on each side of the vertex (fig. 2.9). Each of the beam-beam counters is an array of Čerenkov detector modules. The left detector (farthest away from the forward arm) consists of 44 Čerenkov modules, covering a range in pseudorapidity of $3.0 \leq \eta \leq 4.5$. The right beam-beam detector has 35 modules. It covers the same range in pseudorapidity, but not symmetrically in azimuthal angle, as can be seen from fig. 2.9. The geometry of the right detector is chosen so that is does not interfere with the forward arm at low θ settings. The right detector has a higher density in modules to compensate somewhat for the smaller range in azimuthal angle.

The Čerenkov detector modules are made of $2 - 4$ cm thick lucite, designed to detect

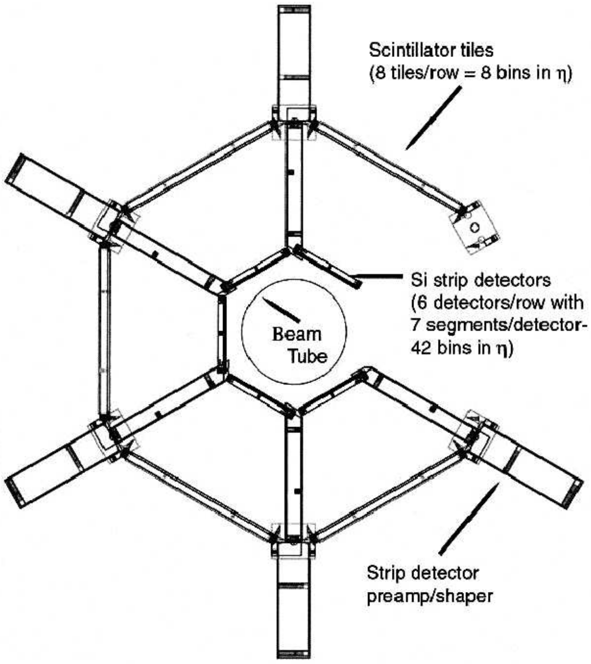

Figure 2.8: *Front view of the BRAHMS' centrality detector*

particles with velocity $\beta \approx 1$. For read-out good photo-multiplier with timing resolution $\sigma \leq 50\ ps$ are used. Four different sizes of radiators are used, with diameters from 1.9 to 6.4 cm.

With beam-beam counters the time-of-flight detectors, TPCs and drift chambers will get a start-time. This time signal is also the level 0 trigger of BRAHMS. Furthermore, the outcome of the counters will lead to a determination of the main collision vertex with a resolution of 1 cm. Multiplicity determined from beam-beam counters will complement what is deduced in the lower pseudorapidity range from the centrality detector. The beam-beam counters thus fulfill several tasks in the setup.

2.5.3 Zero-degree calorimeters

Behind the beam magnets DX there will also be detectors, one on each side of the collision vertex. These detectors are zero-degree calorimeters. As their names indicate they will be placed at zero scattering angle, from where they will measure emitted spectator neutrons from the collision. These neutrons will continue in the beam direction after the collision, since they are not deflected by the magnetic field in the DX magnets. Also they will have energy of 100 GeV, the same as the nucleons in the beam. The positions of the ZDCs are indicated on figure 2.10.

All the RHIC experiments have identical ZDCs. That way comparison of collision parameters deduced from ZDCs in different experiments is easy. The zero-degree energy measured with ZDCs is strongly correlated with the impact parameter in the collision, not so much in energy of each neutron but in multiplicity and thus in total energy deposited

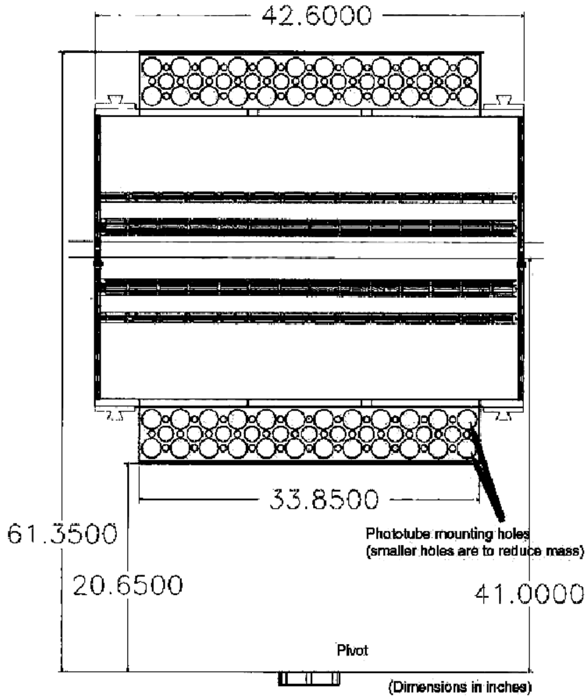

Figure 2.9: *Side view of the BRAHMS' centrality detector*

in the ZDC. The ZDC can thus complement the centrality detector in estimating the impact parameter. This technique has been used with success in the NA49 experiment at the CERN SPS to characterize 158 $AGeV$ $Pb + Pb$ events [NA49c].

ZDCs will serve as the main device for measuring luminosity when RHIC is running with heavy ions. Also ZDCs can detect beam-gas interactions, as they will be asymmetric in energy distribution and thus deposit different amount of energy in the left and the right ZDC. Finally the amount of zero-degree energy will help in determining the stopping of colliding nuclei.

The ZDCs in the RHIC experiments are of tungsten/Čerenkov fiber sandwich design.

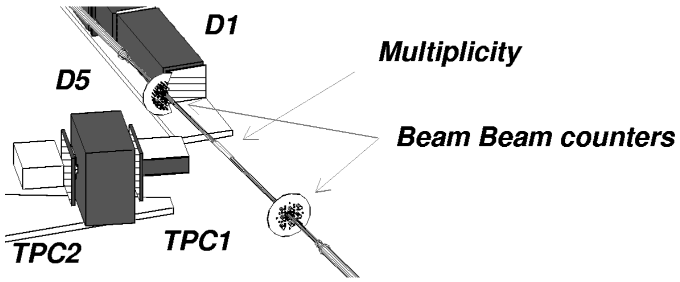

Figure 2.10: *The central region in the BRAHMS setup showing position of the multiplicity and the beam-beam counters.* [CDR95]

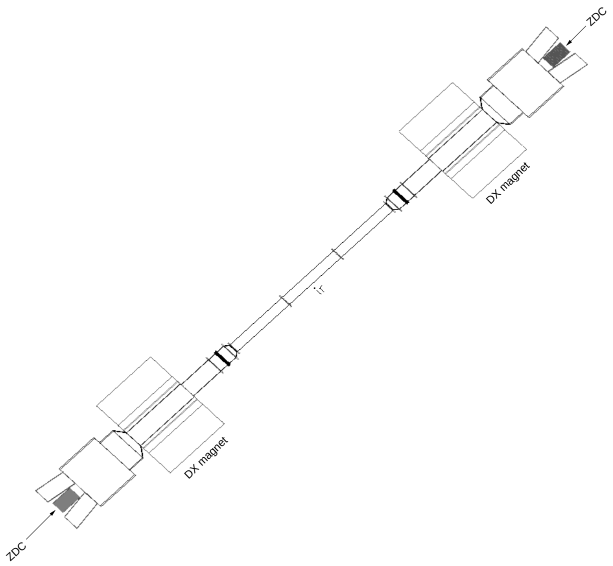

Figure 2.11: *The ZDCs are placed behind the DX magnets, detecting neutrons in the interaction* [ZDC98]

They consist of 3 modules, each of 29 layers of 5 mm tungsten and 0.5 mm PMMA Čerenkov radiating fiber. The modules will be read out with photo-multipliers, one for each module.

Chapter 3

The Time Projection Chamber

The *Time Projection Chamber*, or TPC, is a detector type used in nuclear and particle physics experiments worldwide. TPCs are among the most sophisticated gaseous ionization detectors, capable of providing very accurate space points in three dimensions. They are therefore most used as tracking detectors. In addition they may provide information about the specific energy loss, dE/dx, of traversing particles. For this reason the TPC has sometimes been referred to as an electronic bubble chamber.

In this chapter the development of TPCs from former gaseous detectors will be briefly touched. The main principles of TPCs are presented. Finally the TPCs to be used in BRAHMS are described.

3.1 Principle of operation

Gaseous ionization detectors are based on the principle that when energetic radiation goes through a gas, it will ionize it, resulting in liberated gas ions and electrons. If an electric field is applied, the ions and electrons will move in opposite directions. Electrons being lighter and also less interacting than ions will move faster. Therefore most gaseous ionization detectors are made to read out signal induced by liberated electrons.

Electrons in such a detector are lead toward one or more anode wires where charge is deposited. In some detectors, e.g. *ionization chambers*, there is no amplification of the primary signal around the anode wires. In other detectors the electric field gradients around the wires are so high that avalanches occur, and the primary charge is amplified. The charge read out from a gaseous ionization detector may thus be orders of magnitude higher than the charge liberated by the ionizing radiation. The ratio of amplification depends on the type and amount of gas in the detector, as well as the electric field and thus on the voltage applied to the anode wire. Proportional counters operate with a high amplification, but as the name implies, the charge read out is proportional to the free charge from the primary ionization. The gain in a proportional counter is typically $10^3 - 10^6$. Ascending above a certain voltage on the anode wire, the amplification is so high that a saturation is reached. In this regime the amount of charge read out is no longer proportional to the primary ionized charge. It is also in this regime that we find Geiger-Muller counters.

3.1.1 Multi-wire Proportional Chambers

In 1968 a so called *Multi-wire Proportional Chamber (MWPC)* was invented by G. Charpak among others. This type of detector has a plane of many closely spaced anode wires and a cathode plane on either side of the anode plane. Typical distances are 2 mm between the anode wires and 8 mm between anode wires and cathode plane [Leo94].

A MWPC is read out through the charge disposed on the anode wires and/or charge induced in the cathode planes. In many MWPCs also the cathode planes are arrays of wires. The positive charge resulting from an avalanche around an anode wire, will induce charge on the cathode wires, which may subsequently be read out. By having one cathode plane with wires along the anode wires, and the other cathode wires orthogonal to the anode wires, position of the discharge on the anode may be read out in two dimensions (fig. 3.1).

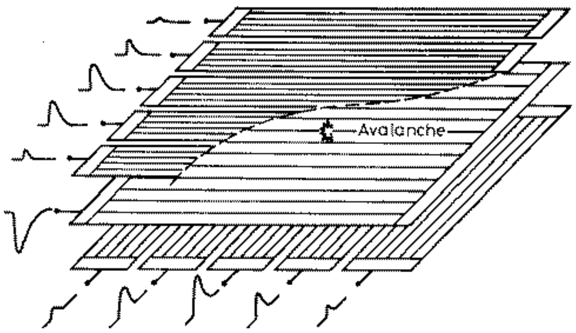

Figure 3.1: *Multi-wire proportional chamber that gives a space point in two dimensions. Eventually, several MWPCs of this kind may be combined to form a telescope and thus reconstruct a particle's track in three dimensions.* [Leo94]

3.1.2 Drift Chambers

Early in the development of MWPC it was realized that also the drift time of electrons from an ionizing event could provide spatial information. With the appropriate drift velocity of a few $cm/\mu s$, the resolution from drift time measurements can cope with the one from MWPCs. Detectors based on this principle are called *Drift Chambers*.

Drift chambers usually operate with drift distances of $5 - 10$ cm. They often have fast scintillating detectors as triggers. In order to cover a wide area, many adjacent drift chambers or cells can be combined. MWPCs have many wires that have to be read out, and therefore need much electronic for the data acquisition. With the use of drift chambers one can reduce the amount of read out electronics, since the number of channels read out is greatly reduced.

However, drift chambers are more sensitive to the working conditions. Since the electrons have to drift longer than in a MWPC, electrons are more likely to be captured in the gas. Drift chamber thus require purer gas than a MWPC. The resolution in a drift chamber also depends to a higher degree on diffusion in the electron cloud, both in transverse and longitudinal direction. The width of the cloud goes as the square of the drift distance times the diffusion coefficient of the gas. Using a gas mixture with low diffusion coefficient, diffusion can be reduced to a minimum.

3.2 Time Projection Chambers

Based on ideas and experience from use of MWPC and drift chambers, the Time Projection Chamber (TPC) was proposed by D.R.Nygren in the middle of the seventies. Its basic principles are illustrated in fig. 3.2.

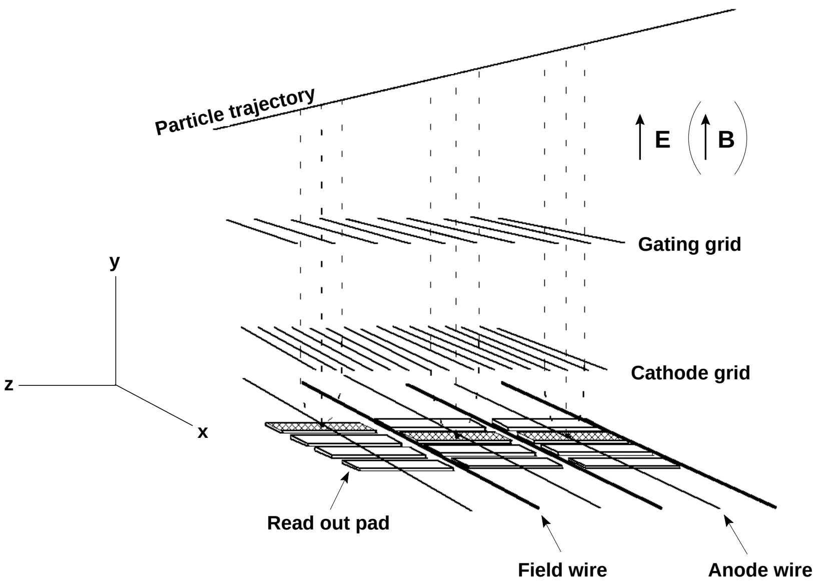

Figure 3.2: *The basic principles for detection in a TPC* [CDR95]

Incoming energetic ionizing particles goes through the drift region of the TPC. The liberated charge is subject to the electric field, and electrons will drift opposite the direction of $\vec{E}$. Close to the anode wire, the field gradient is high enough for creation of an avalanche, its charge being proportional to the number of liberated electrons in the primary ionization. The avalanche will also induce charge on the pads below the anode wire. The anode wires may provide the z-coordinate of the primary ionization if they are read out, and the pads give the x-coordinate. The drift velocity in the gas is also here on the order of $cm/\mu s$, and the time from the primary ionization to the deposition on the anode wire thus gives the y-coordinate. Since TPCs operate in the proportional range of gas amplification, also TPCs can be used to measure the specific energy loss of the incoming particle in the gas. If the momentum of the particle is known, the information about dE/dx can be used to identify the particle. The cathode grid and field wires are used to get the appropriate electric fields.

In many TPCs also a magnetic field parallel to the electric field is applied to the drift region, as indicated on fig. 3.2. With parallel electric and magnetic fields, drifting electrons with transverse velocity components are subject to the $\vec{v} \times \vec{B}$ term in the Lorentz force[1]. These electrons will spiral around the magnetic field lines, thus reducing the transvers diffusion by a factor [Kle87]

$$\frac{1}{(1+\omega^2\tau^2)} \tag{3.1}$$

where

$$\omega = eB/m_e \tag{3.2}$$

is the cyclotron frequency of the electrons and τ the mean free time between two collisions. This reduction factor has typically a numerical value about 10. It is therefore possible to let electrons drift much longer in a TPC than in a drift chamber, and TPCs with drift lengths of several meters have been built. With an applied magnetic field, it is also possible to find the momentum of the ionizing particle from the curvature of the track.

Typically the anode wires have a diameter of less than 100 μm and a separation of a few mm up to a cm. Between the anode wires there are often field wires to shape the electric field. The gap between the anode wires and the pads is on the order of a few mm. The pads may be quadratic or have some other rectangular shape, but usually with a surface less than 1 cm^2. Some TPCs operate at normal gas pressure of 1 atm. Others operate at pressures up to 10 atm. The electric drift field may be several hundred kV/m and the magnetic field a few Tesla. The value of the fields and the pressure depends very much on the chosen gas mixture.

In some TPCs both anode wires and pads are read out, in others only the pads. In any case, the TPC provides three-dimensional space points that can be fitted to reconstruct the track of the particle. The resolution of the TPC highly depends on the width of the clusters detected and also on the spread of the avalanche. As can be seen on fig. 3.3, the clusters from a track are smeared out over several pads. The distribution of charge over

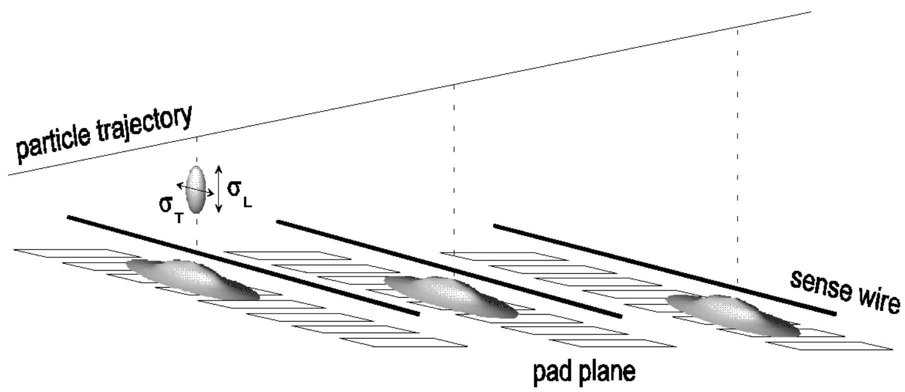

Figure 3.3: *The charge from clusters is smeared out over several pads.* [CDR95]

several individual pads is called the *Pad Response Function* (PRF). As fig. 3.3 indicates,

[1]The Lorentz force is the vector sum of electric and magnetic forces on an electric charge q: $\vec{F} = q(\vec{E} + \vec{v} \times \vec{B})$

the charge distribution over pads is Gaussian, and the PRF is therefore approximated by the Gaussian

$$P_i = A \cdot e^{-\frac{(x-x_i)^2}{2\sigma_x^2}} \tag{3.3}$$

where x is the centroid coordinate of the cluster and x_i it the coordinate of the i^{th} pad along the pad row. By the use of the center of gravity method the position of the cluster centroid along the pad row can be estimated from read out data. Also in the time direction the signal read out is Gaussian and the center of gravity method is used. A typical signal from a TPC as function of pad number in a row and ADC time bin, i.e. to which the center of gravity is applied, is given in fig. 3.4.

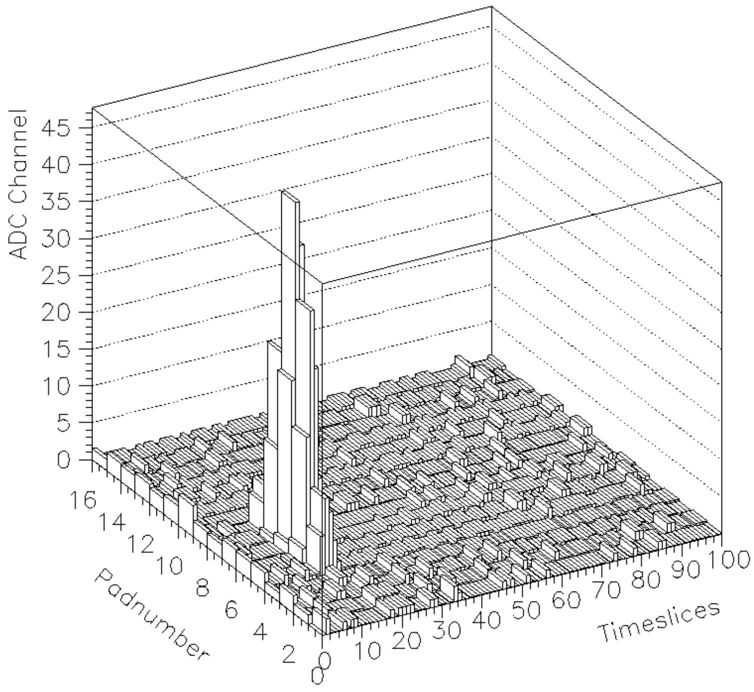

Figure 3.4: *A typical TPC signal from a cluster as function of pad number in a row and time bin.* [ATP95]

As avalanches occur in the proportional region of the TPC, there will be a large amount of positive ions drifting relatively slowly in the direction of the electric field toward the drift region. At low rates of incoming ionizing particles, this is no problem. The problem occurs mainly at higher rates, where the ions lead to non-uniformity in the electric field and increased electron capture. Most TPCs are therefore built with an additional wire array, the *gating grid*, situated a few millimeters above the anode wires (fig. 3.2). With this grid installed the connection between proportional and drift regions in the TPC may be closed when there is nothing to read out, preventing ions from entering the drift region. The gating grid is opened only when a trigger signal indicates that there is data to read out. The trigger signal may come from scintillating detectors, as mentioned in the case of drift chambers.

Also, since the drift distance is so long in a TPC compared to other gaseous detectors, having the correct gas mixture is of paramount importance. The mixtures should have low level of electron capture, low diffusion coefficient, giving drift velocity for electrons of a few $cm/\mu s$ in the applied drift field. Impurities in the gas may lead to distortions in the signal, and gas parameters therefore have to be monitored during experiments. Typical gas mixtures used are $Ar/CH_4, Ar/CO_2, Ne/CH_4, Ne/CO_2$. Some TPCs have used isubutane instead of methane, leading to smaller diffusion both in transverse and longitudinal directions. Also more complex mixtures have been tried, e.g. $Ar/He/Ne/CH_4$.

TPCs have proved to be very accurate detectors. They apply to a wide range in momentum, and the particles that are detected have to penetrate only a minimum of material. Most TPCs operate with a spatial resolution of less than $200 - 300\ \mu m$.

TPCs produce a lot of data that has to be recorded and analyzed. A good read out and data acquisition (DAQ) system is therefore necessary. In the beginning TPCs were read out using *Charged-Coupled Devices* (CCDs), devices that store the analogue signal, and thereafter digitized with slow ADCs. Later on faster *flash ADCs* were used, directly coupled to the wires and pads. Nowadays, however, most TPCs are read out using *Front End Electronic* (FEE) cards, i.e. printed circuit cards, with built in preamplifiers, shapers, ADCs, amplifiers and in some cases storage devices. The FEE cards are mounted directly on the TPC.

When a TPC is read out, charge from the ionizing particle is deposited only on a small fraction of the wires and pads. Also data is recorded for a longer time than it takes to deposit the charge, as can be seen on fig. 3.4. Most of what is read out is therefore noise, so called *pedestals*. This noise is of no interest in the reconstruction of particle tracks. In order to reduce the amount of data, the DAQ system in modern TPCs usually perform pedestal subtraction, called *zero suppression*, from the raw data, before the data is stored or additionally processed. The DAQ also operates with a certain signal threshold. Any signal induced in a read out channel that is below the threshold is not recorded.

Before a TPC can be used to collect data in an experiment, it has to be tested and calibrated. E.g. the actual resolution must be estimated. This can be done with radioactive sources or cosmic radiatiation. Even better is the use of ultra-violet lasers. Especially if the TPC has an applied magnetic field, the use of laser beam is favorable, since the beam is not bent in the magnetic field. One therefore gets straight tracks from which it is easier to get an estimate of the resolution.

3.3 Experiments using TPCs

Many of the recent nuclear and particle physics experiments have used or are using TPCs for tracking. These experiments include ALEPH and DELPHI at LEP, where the TPCs have a toroidal shape surrounding the interaction point. The toroidal TPCs are usually divided in two drift regions, where electrons drift in opposite directions. At the end caps of the toroid the electrons are deposited at anode wires, and signals from particles emanating from the interaction region are read out. The end caps are usually divided into several sectors.

Also the upcoming ALICE experiments at CERN and STAR at BNL will have toroidal TPCs as their main tracking detectors. Fig. 3.5 shows a sketch of what the TPC in ALICE looks like on the drawing board.

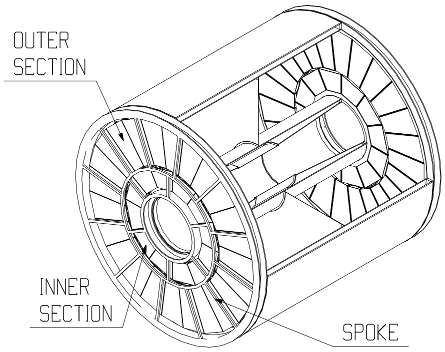

Figure 3.5: *The TPC to be placed in the ALICE experiment at LHC, CERN. The end caps are divided into several sectors.* [ATP95]

Other experiments, such as the NA35 and NA49 experiments at CERN, have used non-toroidal TPCs. The layout of NA49 is shown in fig. 3.6.

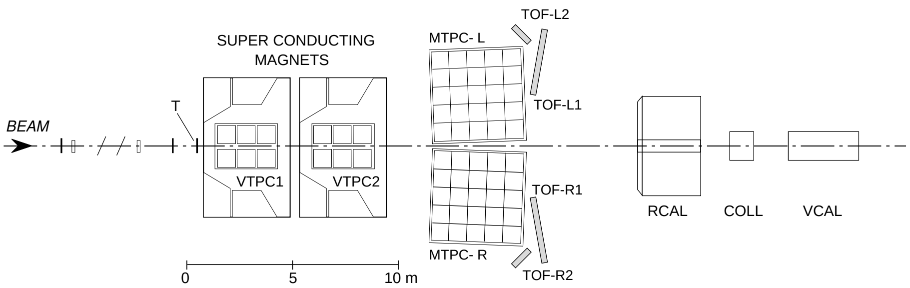

Figure 3.6: *The detector layout for the NA49 experiment. Two kinds of TPCs are used, the vertex TPCs (VTPCs) in a magnetic field and the main TPCs (MTPCs) with no magnetic field.*

The vertex TPCs are submerged in magnetic fields, and charged particles are therefore bent while traversing them. In the main TPCs there is no magnetic field, and particles therefore follow straight lines.

3.4 TPCs in BRAHMS

In the BRAHMS setup there are four TPCs. TPCs T1 and T2 are placed in the forward arm, on either side of dipole magnet D2 (fig. 2.2). MTPC1 and MTPC2 are the tracking detectors in the mid-rapidity arm, on either side of D5.

3.4.1 Physical dimensions

The TPCs in BRAHMS are all rectangular, with drift lengths of about 20 cm. As gas mixture, 90% Ar/10% CO_2 at atmospheric pressure has been chosen. The cages are made of plexi glass, with entrance and exit windows of 25 μm mylar foils. The amplification and read-out is on the top.

All TPCs are placed outside magnetic fields. Tracks from traversing particles are therefore straight. From the different local track segments in the TPCs, along with hits from TOFs, the particles trajectory through the dipoles is extrapolated. From this trajectory the momentum of the particle can be estimated. With this setup a momentum resolution of 1% is expected.

As previously mentioned, especially the TPCs in the forward arm will experience high track density in peripheral collisions and thus at small scattering angles. Events with up 0.2 $particles/cm^2$ in T1 have been simulated. With this in mind the TPCs have been designed to operate with a two-particle resolution of less than 1 cm.

The read-out regions of the TPCs include gating grid, cathode grid, a grid of alternate anode (sense) wires and field wires, and pad plane. The anode and field wires in T1, T2 and MTPC2 have radii of 15 μm and 100 μm, respectively, spaced at 4 mm. Between the anode wires and the pad plane there is a space of 4.5 mm. MTPC1 has wires of the same radii, but they are spaced at 2.95 cm and with a gap from anode wires to pad plane of 4.0 mm.

The TPCs have from 12 to 20 pad rows, each pad being 3.0 mm wide and with a pitch of 3.5 mm. In the forward arm the pads have a length of 2.90 cm, while in MTPC1 and MTPC2 they are 2.95 cm and 2.40 cm respectively. The reason for having shorter pads in MTPC2 is the maximum crossing angle of 22°, while in the mid-rapidity TPCs the crossing angle will not exceed 5°.

A homogeneous drift field is generated by aluminum plates at the bottom of the TPCs and aluminized mylar foil strips along the walls. The nominal voltage applied to the aluminum plates is -5000 V. The strips are very thin, and incoming particles therefore do not lose much energy when going through. Resistors placed between the strips give the right voltage on each strip. With this design a uniform electric drift field of about 250 V/cm with positive direction vertically downwards is generated, resulting in drift velocity for the electrons of $1.6 - 2.0$ $cm/\mu s$.

In developing the TPCs their dimensions have been limited by the available space, particularly T1 in the forward arm. In addition to the detectors mentioned so far, there also has to be room for detectors to monitor the performance of the TPCs. Drift chambers will be used to calibrate the position measurement in time direction. The calibration drift chambers in the forward spectrometer arm come from the AGS experiment E866. Drift velocity is subject to changes with temperature, pressure and impurities, and therefore has to be monitored frequently. Gas from the outlets of the TPCs will therefore be lead through small drift velocity monitors positioned next to the each TPC. Final dimensions of the TPCs are listed in table 3.1. With the listed dimensions there is space enough for monitoring detectors.

The widths and heights of the TPCs are chosen in order to match the angular acceptance of TOFs and dipole magnets. As mentioned in the previous chapter the magnetic fringe field of the dipole magnets is small. Values for fringe fields of D1 in the volume of

TPC	Width (x) [cm]	Height (y) [cm]	Length (z) [cm]	No. Rows	Pads per row
T1	33.60	19.80	56.00	14	96
T2	39.60	19.80	75.50	16	112
MTPC1	38.40	20.00	36.60	12	96
MTPC2	67.68	19.80	50.00	20	144

Table 3.1: *Summary of dimensions of the TPCs in BRAHMS. The spatial dimensions are active inner dimensions.*

T1 have three dimensional simulations using TOSCA shown to be at most 10^{-4} T.

As T2 is particularly long, its length causes high tensions on the read-out plane, which is therefore divided into two parts, each of 8 pad rows, with a supporting structure in the middle. The supporting structure causes a dead area of 7.5 cm.

3.4.2 Read-out

The read-out of the TPCs will be done by the use of STAR FEE cards. Each FEE card has 32 channels, and reads 16 pads from two adjacent pad rows. The number of pad rows for each detector is therefore even, and the number of pads per row a multiplum of 16. Also, in deciding the dimensions for the TPCs one has had to take into account the necessary space for the FEE cards.

Each FEE card is a $5 \cdot 10$ cm^2 printed circuit card that include charge sensitive preamplifier, shaping amplifier, 512 samples analog storage in Switched Capacitor Array and ADC. In each FEE card data are multiplexed and sent to the read-out board.

The read-out board, also originally designed for the STAR experiment, has 32 connectors for FEE cards, which amounts to a total of 1152 channels. This means that not all pads on a TPC will be read out. It has been proposed to read out 1152 channels from the mid-rapidity arm TPCs and 768 channels, or 24 FEE cards, from the forward arm TPCs. This lower number in the forward arm is mainly due to budget restrains.

In the read-out board signal from the entire TPC is multiplexed and sent on optical link to a VME receiver board specially designed for BRAHMS. This receiver board and VME crate is situated in the nearby fast electronics hut, right outside the interaction hall.

In the receiver board the data from the FEE card are sorted into time-ordered sequences. This procedure also implies zero-suppression of the data. I.e. only if two consecutive time bins each have ADC value above 6, a sequence is generated. Also two time bins before the first good bin and two bins after the last good bin are stored. Generated sequences are stored on data files

Some online analysis will be done in order to reduce the amount of data stored. Later on probably track reconstruction will be done online, thus making it necessary to store only the track information and not the data for each cluster. In the initial runs only pedestal subtraction and zero-suppression is implemented. Track reconstruction and data is presented in more detail in the next chapter.

Chapter 4

Analysis tools

The BRAHMS experiment and test setups give their output in computer data files. In order to analyze this data, appropriate software is needed. The BRAHMS collaboration has chosen to base the analysis on ROOT, an object oriented (OO) framework made at CERN. With ROOT as a base the BRAHMS collaboration has made classes and tools specific for the BRAHMS experiment. This software is gathered in the *BR*ahms *A*nalysis *T*oolkit, or BRAT.

In this chapter I present the basic features of ROOT and BRAT. I also outline most of the changes I have done to my local copy of BRAT. This chapter assumes some knowledge of OO programming and C++.

4.1 ROOT

The new generation of experiments at LHC at CERN will need analysis power a couple of orders of magnitude larger than former experiments. Also, former analysis tools have mostly been procedural-based, programmed in Fortran 77.

To cope with the new demands in analysis power, the ROOT project was started at CERN. ROOT is object oriented, programmed in C++ [RoWWW]. It consists of libraries of several hundred classes organized in hierarchies, thus making use of inheritance. The hierarchies include classes for histograms, mathematical functions, N-tuples, vectors, input/output, storage, graphical user interface, documentation and system tools, among others. ROOT thus fulfills many tasks in typical nuclear and particle physics experiments.

ROOT is also an interactive program where all commands and macros are C++ statements. Therefore C++ it the sole computing language one need to use when working with ROOT. The use of C++ as command and macro language is made possible through CINT, the C/C++ interpreter. CINT is able to interpret about 95% of ANSI C and 85% of C++.

One of many useful features in ROOT is that it has a well developed Runtime Type Information System. When using ROOT as an interactive program it is easy to get information about local and global variables, functions, classes and data and function members of classes. This information is stored in a memory resident dictionary. When running a ROOT based application, one therefore has good control over its performance.

Also documentation is emphasized in ROOT. Classes exist for making documentation in Postscript and HTML format. Documentation is often a time consuming task, which is much easier with ROOT's automatic document generation. In ROOT it is also possible to make useful graphical visualizations, e.g. of the inheritance tree in a class hierarchy.

ROOT can be downloaded from the ROOT web pages [RoWWW] and installed to work on most currently used operating systems. It is still under development.

4.2 BRAT

4.2.1 General features

The BRAT library is made by and for the BRAHMS collaboration. Currently it contains about 120 classes, but as with ROOT it is still being developed and is subject to changes. When new versions of BRAT are ready, they are "checked into" a CVS repository at a BNL computer (ref. App. B). Each version is tagged with a version number for easy reference. The version I have used is named VER-1-5. BRAHMS collaboration member can thereafter log on to the BNL computer and download BRAT.

BRAT serves many purposes in BRAHMS. It is used both in simulations and in analysis of test data and real experimental data. Simulations of detector performance in BRAHMS is mainly done in GBRAHMS, BRAHMS' version of the GEANT simulation package [1]. Data files produced in GBRAHMS simulations can be read into BRAT and analyzed. Doing this it also possible to test the performance on analyzing algorithms to be used also on real data.

Included in BRAT are classes for data objects, containers, graphical user interface, input/output, detector specifications, monitoring and data processing. The BRAT classes are compiled into shared object files that can be loaded into ROOT (ref. App. A).

As with ROOT one can use BRAT in both interactive sessions, typically in macros, and in compiled programs. In my use of BRAT I have only made macros, and I will therefore not discuss compiled programs. However, the approaches are almost identical, i.e. very few adjustments have to be made to a macro in order to compile it, since C++ is used in both approaches. This is a strength of ROOT based applications.

When starting an interactive session the BRAT classes are loaded into memory (ref. App. B). The BRAT classes can then be used in the same way as ROOT classes. Instances of classes can be declared and Run Time Type Information (RTTI) is easily accessible. Many of the BRAT classes fit nicely into the inheritance hierarchies for ROOT classes.

4.2.2 Using BRAT on TPC data

In tests of the BRAHMS TPCs many data files have been produced. The raw data files I sometimes refer to as *dat-files*, as they by convention are named with suffix ".dat". The format of data stored in the files has changed during development and testing. The format of the data files I have used in my analysis is described in App. C. With the use of BRAT

[1] In my work I have not used GBRAHMS. It is therefore outside the scope of my thesis to give a detailed description of GBRAHMS, and I will therefore only briefly touch this subject. For further information I refer to [BrWWW].

reading data from raw data files is done with an instance of the class **BrRawDataInput**[2]. Knowledge about the format of TPC data files is thus not strictly necessary when using BRAT.

Different detector parameters and geometry have to be known to the analyzing software. E.g. the drift velocity in a TPC is used in calculations of local y-coordinate, and the position of the detectors in one of the spectrometer arms is necessary to know in order to follow a particle through the entire arm. However, drift velocity changes with external conditions such as temperature and pressure, and the spectrometers are able to rotate about the main interaction vertex. In the earlier versions of BRAT the necessary parameteres are given in data files loaded upon startup of the session or program, or eventually later if parameters have been changed during analysis. In the new versions of BRAT, however, the analysing software will get the necessary parameters from databases. The databases and their interface are still under construction and therefore not used in the analysis presented in this thesis.

When raw data files are read into BRAT, data from each read-out pad is stored as instances of **BrTPCSequence**, that I shall refer to simply as *sequences*. This class has data members for row number, pad number, time for first time bin, an array of ADC values and number of time bins, i.e. number of ADC values. Sequences from one event are stored in instances of the container class **BrEvent**, which inherits from **BrEventNode**.

Reading raw data into sequences has a time consuming task, since for many of the data files zero-suppression was not applied. Therefore the data files I have analyzed have first been converted into **BrTPCSequence** format. The instances of **BrEvent** have then been stored in data files. When I do the actual analysis I load these converted files instead, and the analysis is thus speeded up.

The converted files I rather refer to as *root-files*, since they are all named with suffix ".root". In the conversion to root-files, the data is resequenced. This means that ADC values below a certain limit, or *cut*, is rejected. Only interesting ADC values are stored in the root-files. This procedure reduces the amount of data considerably and thus also speeds up the analysis. Typically the root-file has a size of less than 0.4% of the corresponding dat-file. This ratio, however, I expect will change for data files from beam tests and BRAHMS runs, as in normal data taking zero-suppression will always be applied.

When reading data from root-files, an instance of the class **BrEventIO** is used and not **BrRawDataInput**. However, whether data is read through **BrEventIO** or **BrRawDataInput**, the data from the file is available in **BrTPCSequence** form, stored in instances of **BrEvent**, one instance per event read from file. After reading from dat-files, one can resequence the data in the **BrEvent**, as mentioned above. Resequencing data speeds up cluster and track finding, which is the next step. As data is now stored in as **BrTPCSequence** form in a **BrEvent**, further data processing is independent of file type.

Tools for cluster and track finding in TPC data are assembled in the class **BrTPCTrackingModule**, which inherits from **BrLocalTrackingModule**. As an instance of **BrTPCTrackingModule** is created the previously loaded geometry and detector parameters are made available to the instance. There are four TPCs in BRAHMS, and if

[2] As a general naming scheme, all classes in BRAT have names starting with "Br". For plain ROOT classes another scheme is used, where all class names start with "T".

parallel analysis of data from more than one TPC is to be done, one instance of **BrTPCTrackingModule** has to be created for each TPC. I have analyzed data from only one TPC, and therefore only created one instance of **BrTPCTrackingModule** in each session. I will in the following refer to this instance as the *tracking module*.

From BRAT VER-1-5 there are two choices for cluster finding algorithms and two choices for track finding algorithms. One cluster finding method (cluster method 0) and one track finding method (track method 0) are SONATA[3] methods rewritten in C++. The other two methods (cluster method 1 and track method 1) are mainly developed by the BRAHMS collaboration, even though some algorithms have been taken from Sonata also for these methods. At present no extensive comparison has been done between the respective methods since methods 1 were made available in march this year. However, track method 1 is likely to be better in finding steep tracks. The methods are chosen with the **BrTPCTrackingModule::SetClusterMethod(Int_t val)** and **BrTPCTrackingMethod::SetTrackMethod(Int_t val)** methods, where the integer **val** is the method number, i.e. 0 or 1.

The output from track finding is also an instance of **BrEvent**, with entries of **BrDetectorTrack**, that I refer to simply as *detector tracks*. The data objects used to generate detector tracks, i.e. instances of **BrDetectorHit**, are available. I call these instances *detector hits*. The detector hits, however, are generated from data objects more closely related to the TPC, i.e. instances of **BrTPCHitCluster**. I shall in the following refer to these instances as *clusters*. The output from **BrTPCTrackingModule::GetTPCClusters()** is a **BrDataTable**, also a container class, filled with clusters from the event just analyzed.

To be specific, instances of **BrEvent** contain instances of **BrDataTable**, which then contain instances of **BrTPCSequence**, **BrDetectorTrack**, some other data class or container class. It is therefore possible with storage at several levels in instances of **BrEvent**. With unique names for the different instances of **BrDataTable** it is possible to find the tables by using **BrEventNode::GetDataTable(const Char_t* ObjectName)**, where **ObjectName** is the name of the data table.

4.3 Modified BRAT

In doing my analysis of TPC test data files, I have done some modifications to the BRAT code. This I started with in a version of BRAT earlier than VER-1-5, but I have later done the same changes in VER-1-5. For this reason I have in my analysis only used cluster and track finding methods 0, since these are carbon copies from the previous BRAT version. In order to be able to use also cluster and track finding methods 1, the necessary changes should also be done for these methods.

To be able to get the desired output from analysis I have done changes in several BRAT files. The modified files are listed in table 4.1, where $BRATSYS is the directory where all files and subdirectories of BRAT are situated (ref. App. B).

BrTPCHitCluster.h - I needed to add functionality to the **BrTPCHitCluster** class to

[3]SONATA is a simulation and tracking program made by Flemming Videbæk. It is was used in the early preparation for the BRAHMS experiment.

File	Directory relative to $BRATSYS	Description
BrDetectorHit.h	track/inc/	Storage of data from digitized hit in any detector, used in track finding algorithms.
BrDetectorTrack.h	track/inc/	Storage of data for particle track in a detector.
BrTPCHitCluster.h	tpc/inc/	Storage of data from digitized hit in any TPC.
BrTPCTrackingModule.cxx	tpc/src/	Module with interface for cluster/hit finding and track recognition in any TPC.

Table 4.1: *List of BRAT files that have been modified for the analysis.*

be able to store the width of a cluster in number of pads and number of time bins, as well as the maximal ADC value in the cluster. This is done by adding three new data members **fNpads**, **fNbins** and **fPeak**, and their respective getters and setters, i.e. **GetNpads()**, **SetNpads(Int_t i)**, **GetNbins()**, **SetNbins(Int_t i)**, **GetPeak()** and **SetPeak(Float_t x)**. Also to ease my plotting routines, I have added data members to store information related to the track the particular cluster belongs to. By belonging to I mean that the particular cluster is one of the clusters used to fit the track. These data members are:

- **fTanBeta** - $tan(\beta)$ for the track.
- **fTanLamda** - $tan(\lambda)$ for the track.
- **fY** - the y-coordinate of the track at z = 0.
- **fXRes** - the clusters residual in the x-direction.
- **fYRes** - the clusters residual in the y-direction.

The **BrTPCHitCluster** class I have also equipped with getters and setters for these track-related data members.

BrDetectorHit.h - When fitting a track, the tracking module uses detector hits as input to the fitting functions. After fitting the detector tracks and hits are easily accessible in the output instance of **BrEvent**. Calculations of residuals, which is an essential part in the analysis, are done with information from the track and its corresponding hits. In order to store the residual of a hit, I added functionality to the **BrDetectorHit** class to be able to store residual in x and y, and provided getters and setters. The data members I have called **fXResidual** and **fYResidual**. The above mentioned residual data members of clusters get their values from **fXResidual** and **fYResidual** of their corresponding detector hits.

BrDetectorTrack.h - Also for the **BrDetectorTrack** class I have added functionality to be able to store information about residual. I have added four data members to this class. They are **fXResidual** and **fYResidual** to be able to store the averaged residual, not RMS, for the track. These values should be close to zero, and I have used them mainly for testing my algorithms. Then come **fXResidualSq** and **fYResidualSq**. These are the averaged squared residuals in x and y directions. To the **BrDetectorTrack** class I have also added getters and setters for these data members.

BrTPCTrackingModule.cxx - Finally, I had to make some adjustments to some of the member functions of the tracking module. These member functions are:

- **FindClusters(BrEventNode* InputNode)** - finding clusters from instances of **BrTPCSequence** in the input table.
- **ScanMultiHitClusters(Int_t irow)** - scan through clusters that have been marked as multi-hit clusters in the FindCluster function.
- **ClusterHitsToDetectorHits()** - transform clusters into detector hits.

In the FindClusters function I have had to add a couple of lines to call the **BrTPCHitCluster::SetPeak(Float_t x)**, **BtTPCHitCluster::SetNpads(Int_t i)** and **BtTPCHitCluster::SetNbins(Int_t i)** member functions. To get arguments to these two function calls I have used the local variables **adcmax**, **pmax**, **pmin**, **tmax** and **tmin** already present in the BRAT code downloaded from BNL.

The ScanMultiHitClusters function has been changed in a very similar way, one difference being that I have added local variables **pdadc** and **adcmax** to look for maximum ADC value in a cluster, as was already implemented in the FindClusters function of the original code. Furthermore I have added a couple of lines to do the actual search for maximum ADC value. These lines are just carbon copied from the FindClusters function. Finally the same cluster member function calls as in the FindClusters function are added. In addition the clusters created in this function are also given a unique ID, i.e. an integer. This was only implemented in the FindClusters function.

The only adjustment to the ClusterHitsToDetectorHits function is that the detector hits are given the same ID as the clusters they are derived from. This eases the later matching of cluster and hits. **BrDetectorHit** already had a data member **fID**, but it was not used.

In doing my adjustments, I may have broken some guidelines and conventions agreed upon by the collaboration when programming BRAT. It is therefore a question whether some of the necessary changes rather should be made by declaring new classes with inheritance from the original BRAT classes. This may be done at a later stage if the added functionality is convenient for other analysis as well. Nevertheless, in order to be able to get some test results before RHIC starts running, I have chosen to do the changes in the original BRAT classes.

Some of the changes have been used for testing purposes or to ease the analysis, and do therefore not show up directly in the plots of chapter 5. Also, a few additional changes related to cuts in data are presented in chapter 5. These changes have been done at a later stage and not prior to the analysis as is the case for the changes in this chapter.

Chapter 5

Analysis of TPC test data

The BRAHMS experiment has four TPCs. Before the TPCs start taking data from $Au - Au$ collisions in RHIC, they have to be tested to check their performance. I have in particular investigated the performance of T1, the first TPC in the forward arm. The geometry and certain parameters of T1 known prior to my analysis are given in section 3.4. Other parameters not known "a priori" but necessary for the use of TPCs have been my task to investigate. These parameters are presented as I go along.

5.1 Detector test

5.1.1 Test setup

Several tests with T1 have been carried out at BNL, generating data files that have been used in this analysis. I have had available files from tests in December 1999 and in January and March 2000. All of these tests have detected cosmic rays, using the dedicated read-out electronics to be included in the final setup in the interaction hall (interaction region, *IR*). T1 was placed vertically on a table, as indicated in fig. 5.1. Scintillating tiles were placed on top and underneath the detector cage, and coincidence was demanded in order to read out the pads. Fig. 5.2 shows where reconstructed tracks from the January test cross surfaces at the z-coordinates where the tiles were placed. The shapes of the tiles are obvious. Both tiles are quadratic, the upper tile with sides of 6 $''$ (15.2 cm) and the lower with sides of 12 cm.

In all tests a drift voltage $V_D = 5000\ V$ was applied. The gating grid was not pulsed, but the multiplicity when detecting cosmic rays is so low that build up of space charge in the drift region is not likely to hamper T1's performance. One of the intentions with the tests was to find the optimal voltages applied to the anode and field wires. These voltages are referred to as V_A and V_F, respectively. The influence from anode and field voltages on the detector performance has therefore been investigated to some extent.

Another reason for doing these tests with T1 is that T1 has not been able to hold the desired voltages. From time to time electric sparks have occurred in the upper high voltage grid in the read-out region, i.e. the grid of alternate anode and field wires. To be more specific, the sparks have been found to occur on the bus where anode and field wires are soldered. As a result of a spark a great amount of charge, exceeding the saturation

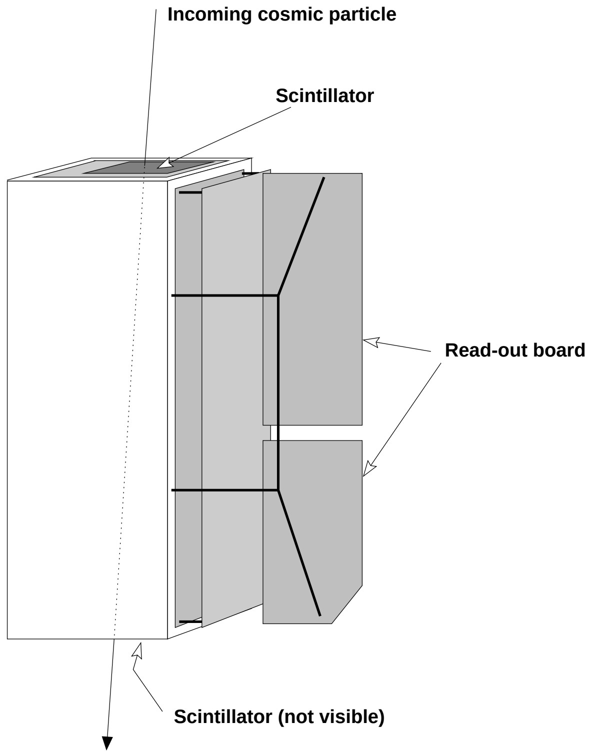

Figure 5.1: *A sketch of the setup of T1 in a BNL lab. The lower trigger scintillator is not shown, but is of similar size at the upper scintillator.*

limit of the read-out electronics, is induced on pads lying above the sparking wires. A few of these events have been found in the data, but they do not in general occur during the short time window from coincidence till the event is read out. The sparks therefore do not seem to hamper the performance of T1 when detecting cosmic rays. However, these sparks that are recorded are useful when looking for the saturation limit in different FEE cards.

The gas mixture used in these tests was 90% Ar and 10% CO_2, i.e. the same mixture as will be used in the IR. However, the gas to be used in the IR will be purer than the one used in the tests.

The testing of TPCs in the lab, as it has been done at BNL, can of course not completely reflect the conditions under which the TPCs will run in the IR. Especially the multiplicity from cosmic radiation is far below what the TPCs will experience when used to detect the outcome from heavy ion collisions. Also the amount of background radiation and operating temperature are different. The differences have to be kept in mind when analyzing the test data.

5.1.2 Data files

Several data files with varying number of events were generated in each of the test runs. The files have thereafter been converted to root-files. The input macro thus reads from

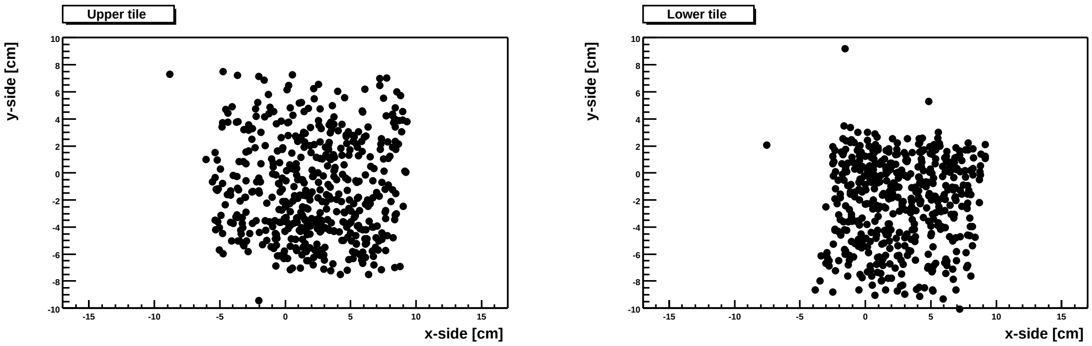

Figure 5.2: *The tiles used as trigger in the January test of T1. The points indicate crossings of reconstructed tracks at local coordinate z = -30 cm and z = 30, i.e. approximate position of the upper and lower tiles respectively.*

root-files. Each file contains data from events registered with only one anode and one field voltage setting. The available voltage settings and corresponding data files are listed in table 5.1.

Anode voltage, V_A [V]	**Field voltage, V_F [V]**	**File**	**No. events**	**Month of recording**
1247	300	a1247f300.root	42	Dec. 1999
1450	450	a1450f450.root	501	Dec. 1999
1450	500	a1450f500b.root	285	Dec. 1999
1600	700	a1600f700.root	499	Dec. 1999
1650	750	a1650f700.root	871	Dec. 1999
1250	0	jana1250f0.root	1392	Jan. 2000
		jana1250f0-2.root	687	Jan. 2000
		jana1250f0-3.root	763	Jan. 2000
1200	10	mar1200f10.root	1215	March 2000
1220	10	mar1220f10.root	879	March 2000
1250	10	mar1250f10.root	57	March 2000
		mar1250f10-2.root	664	March 2000

Table 5.1: *Overview of the voltage settings and data files used in the analysis.*

As can be deduced from the table, the statistics at each voltage setting varies quite much. This has to be taken into account when reading the results presented in this chapter. The setting used in the January test with ($V_A = 1250\ V, V_F = 0\ V$) has best statistics. After this setting comes the ($V_A = 1200\ V, V_F = 10\ V$) setting in March. These two settings are therefore most used when describing the general features for all settings.

5.2 Premises

The design of BRAHMS' TPCs has been chosen in order to do tracking in events with high multiplicity. However, in the lab using cosmic radiation one will not in general have high multiplicity. From time to time there is a shower of particles going through the detector, but they are too few to give good statistics. Therefore these showers have been rejected and attention is drawn toward single track events instead. Using only single track events one find of course very few multi-hit clusters. This allows a better analysis of diffusion, since multi-hit clusters often are wide, both in transverse and longitudinal direction[1]. Also, they generally contain more charge than single-hit clusters, influencing on the study of electron capture.

The tracks studied are straight tracks. The angle between the projection of a track in the pad plane and the z-direction is limited to $-5° < \beta < 5°$. Similarly the dip angle of a track, i.e. the track's angle with the pad plane, is limited to $-5° < \lambda < 5°$. The reason for choosing straight tracks only is that some parameters, e.g. width of clusters and residuals, depend on the angle of the track. In a first approximation the angular dependence can be neglected when the angles are limited to the above intervals.

However, the true angular distributions, i.e. without cuts in β and λ, are wider and limited by the trigger scintillators. The tracks reconstructed from the January data files give angular distributions shown in figs. 5.3.

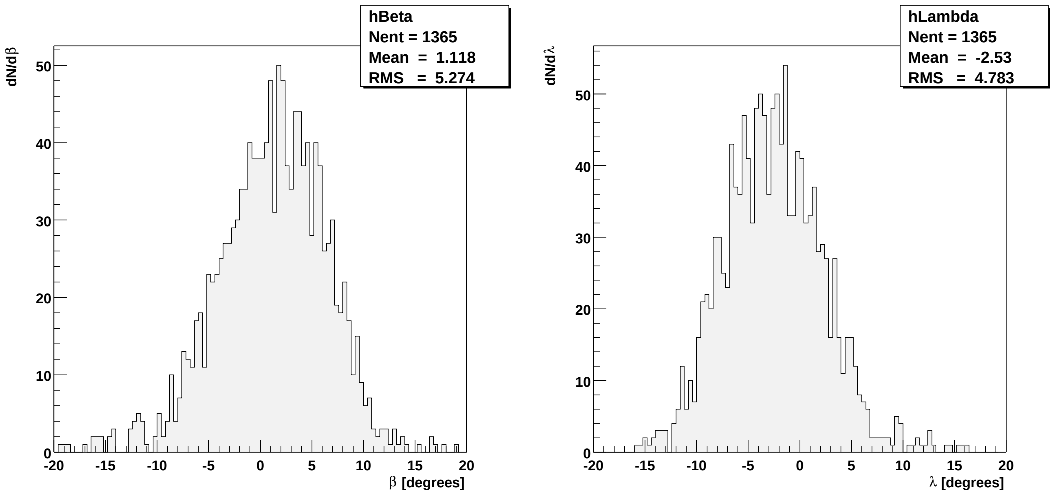

Figure 5.3: *Angular distributions of reconstructed tracks from the January test of T1. The angles are limited by the size of the trigger tiles.*

In addition to modifications in the BRAT code mentioned in section 4.3, a few more modifications have been made to the cluster finding algorithm. In the original brat code, clusters are considered to be noise if they have a width, i.e. a weighted standard deviation σ, either in transverse or longitudinal directions below certain limits. These

[1] Generally the term "transverse" is used along the pad-direction, i.e. x-direction, and "longitudinal" along the time- or y-direction.

lower limits in widths are entered into the instance of **BrTCPTrackingModule** by the user/programmer, and typical low limits used are $\sigma_{T,min} = 0.6$ pad in the transverse direction and $\sigma_{L,min} = 1.0$ time bin in the longitudinal direction.

However, one may argue that width of a cluster should not be used when deciding whether it is noise or not. If a cluster is too wide it may be checked to see if it is a multi hit cluster, but if it is narrow it may still be a good cluster. In any case it is not clear what values to use as lower limits for cluster width.

Rather than using the weighted standard deviation to check for noise, the number of pads and max number of time bins in one pad has been used to decide whether a cluster is noise. Clusters that stretch out over less than 2 pads and 3 time bins are rejected as noise. In a sense this is also a "width cut" similar to $\sigma_{T,min}$ and $\sigma_{L,min}$, but it puts less limitations on the shape of the cluster. If the charge of the cluster is concentrated in few pads and/or time bins it may still be considered a good cluster according to my modified cut, but it is likely not to go through the original algorithm.

In order to check for multi hit clusters, on the contrary, the weighted standard deviations σ_T and σ_L are still used. The limits above which it is checked to see if a cluster may be a multi hit cluster are $\sigma_{T,max} = 1.6$ pad and $\sigma_{L,max} = 2.0$ time bins.

By using this modified algorithm one can see that the number of clusters the algorithm is able to find, does no change much. This number includes good clusters and noise clusters. Nor is there any significant change in the number of reconstructed tracks . The number of hits per track seems to increase somewhat at low voltages. It thus seems that doing this change also results in improved efficiency at low voltages. Table 5.2 summarizes the change in numbers of found clusters, reconstructed tracks and number of hits in reconstructed tracks from the January and March test data. The cuts discussed below are applied to the algorithm for these comparisons.

V_A [V]	V_F [V]	Algorithm	No. clusters	No. tracks	No. track hits	No. hits per track
1250	0	1	15104	1489	8461	5.7
		2	15089	1477	8390	5.7
1200	10	1	5065	614	3281	5.3
		2	4769	612	3474	5.7
1220	10	1	3499	464	2581	5.6
		2	3649	466	2637	5.7
1250	10	1	2605	335	1890	5.6
		2	2604	331	1864	5.6

Table 5.2: *Number of found clusters, reconstructed tracks, track hits and number of hits per track using the original BRAT cluster finding algorithm (1) and the modified algorithm (2). Here data from only 6 pad rows is investigated, ref. section 5.3.1.*

From the table it seems that the modified version of the cluster finding algorithm assures a better efficiency at low anode voltage settings, while there is no significant change for the higher voltage settings.

5.3 Applied cuts

5.3.1 The "edge effect"

Other people within the collaboration have also studied the performance of the TPCs in BRAHMS. It was early discovered that there is some unexpected behavior in signals from pads close to the edges of the pad plane. The observed behavior has therefore loosely been referred to as the "edge effect". It seems that the drift time for electrons deposited close to the edges is longer than for electrons deposited elsewhere in the pad plane. When visualizing tracks of particles through the TPCs one clearly sees the hits' time-component deviating from the straight line in the first and last pad rows, fig. 5.4. Also in the other pad rows the longitudinal component of the position of hits deviate more than the transverse component.

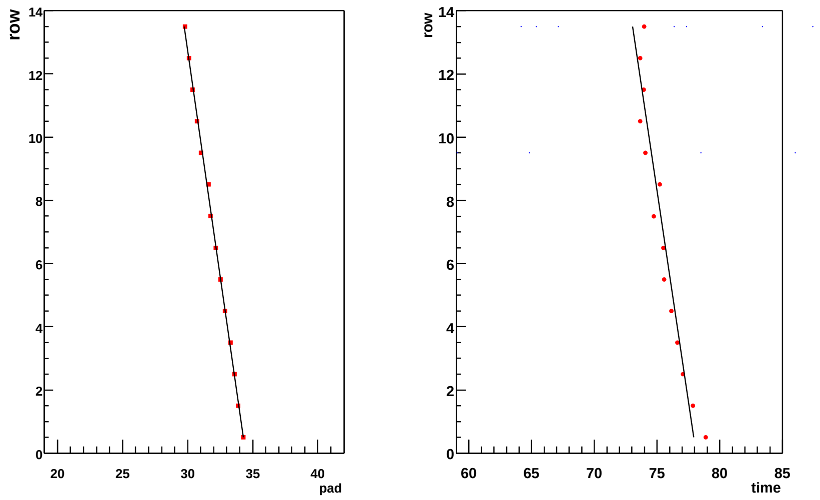

Figure 5.4: *Reconstructed track in T1. The time components of hits in the first and last pad rows show clear offset from the straight line fit.*

When plotting the residuals of tracks as function of row number, one can easily see systematic deviations especially in the first and last pad rows, but also to some extent in other pad rows close to the first and last rows. In figs. 5.5 data only from the ($V_A = 1200\ V, V_F = 10\ V$) setting in March is used, but the same pattern is found in data from other settings in March as well as in December and January. The y-component of hits in the first and last pad rows are typically offset by $2 - 3\ mm$ from the straight line, even though these hits are included when the line is fitted.

The reason for the edge effect seems to be due to a wrong resistor in the resistor chain that generates the drift field in the TPCs, section 3.4. The distance between the aluminized foil strips is constant, but the gap between the lower strip and the aluminum plate is smaller. In MTPC2 the strip separation is 14 mm, while the gap from the lower

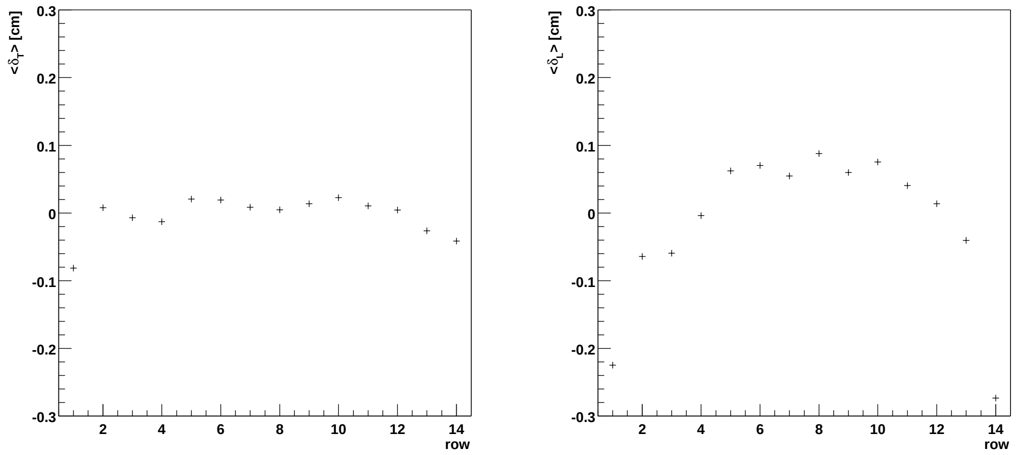

Figure 5.5: *Averaged transverse (left panel) and longitudinal residuals as function of pad row, using all pads rows.* ($V_A = 1200\ V, V_F = 10\ V$)

strip to the aluminum plate is 8 mm. However, the same resistor has been used in this gap as between the foil strips, even though the correct resistance would be the present resistance multiplied by a factor 8/14. In Garfield simulations this misplaced resistor has shown to give an inhomogeneous drift field, which is especially bad close to the strips, i.e. it affects mainly the electrons close to the edge of the pad plane.

In order to cope with the edge effect, the remainder of this analysis has been limited to the six middle pad rows in T1. From figs. 5.5 one can see that these rows do not differ to much in residuals. In the following the first four and last four pad rows are therefore disabled. This is done in the detector parameter file, thus discarding clusters from the disabled rows. When redoing plots of residual as function of row number, the interval in averaged residuals is narrower, figs. 5.6. (Note the change of scale.)

5.3.2 Additional high residuals

However, even when using only the six middle rows, there are still tracks with high residuals . In plotting averaged squared residuals for tracks there are still a few tracks with residuals of high values, both in transverse and longitudinal directions, figs. 5.7. For all the files combined the following overall extrema are found,

$$Max\ transverse\ RMS\ residual: \ \delta_{T,RMS}^{max} = 0.33\ cm \tag{5.1}$$

$$Max\ longitudinal\ RMS\ residual: \ \delta_{L,RMS}^{max} = 0.36\ cm \tag{5.2}$$

where the average is over all clusters used to fit a track. To eliminate these high residuals, a cut in RMS residuals of tracks is applied. The same cut is applied in both transverse and longitudinal directions. The cut value is set at $\delta_{C,RMS} = 0.08\ cm$, i.e. $\delta_{C,RMS}^2 = 0.0064\ cm^2$ pointed out on figs. 5.7. At this value the distributions of squared averaged

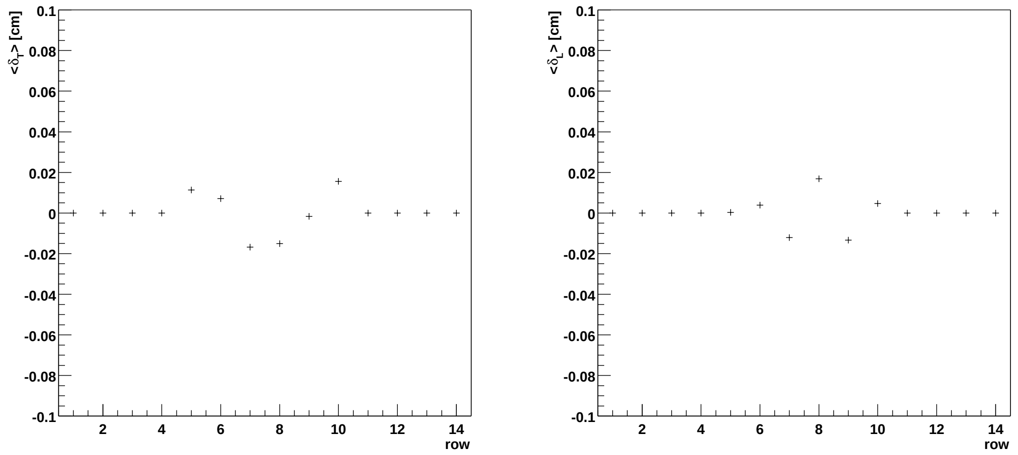

Figure 5.6: *Averaged transverse (left panel) and longitudinal residuals as function of pad row, using only 6 middle pad rows. ($V_A = 1200\ V, V_F = 10\ V$)*

residuals have flattened out and therefore few tracks are lost when applying this cut. In the following this cut is applied.

5.3.3 Saturation

Plotting the number of pads and time bins in a cluster, there are tails up to high number of pads and time bins, figs. 5.8. These plots include all the test files, and one can see that there are clearly clusters with up to 16 pads and up to 15 time bins that go through the cluster finding algorithm.

Looking more closely into clusters with high number of pads and bins, one finds that many of them are saturated. They are all flat on top. The limit for saturation varies somewhat from one FEE card to another, but typically saturation is reached at zero-subtracted ADC values between 650 and 850. Most saturated clusters are wide clusters, but there are clusters down to a width of 6 pads and other clusters stretching over 7 time bins that are saturated. Fig. 5.9 shows sequences which in the cluster finding algorithm have been translated into a cluster that stretches out over 6 pads.

In deducing clusters from data one should probably avoid saturated clusters, as it is difficult, if not impossible, to get a satisfactory estimate for the centroid if doing Gauss fit or similar parameters if other methods are used. For this reason a cut to discard saturated clusters has been introduced in the source code of the **BrTPCTrackingModule** class. The cut implies that good clusters can have at most one pixel with ADC value above 700. In the following this cut is applied.

Using this cut one can see that saturation varies a great deal from one setting to another, fig. 5.10. In plotting the max ADC of clusters in the December $V_A = 1650\ V$ setting and the January $V_A = 1250\ V$ setting, fig. 5.11, the saturation is clearly visible. In the other settings saturation is hardly visible or not visible at all from the distribution

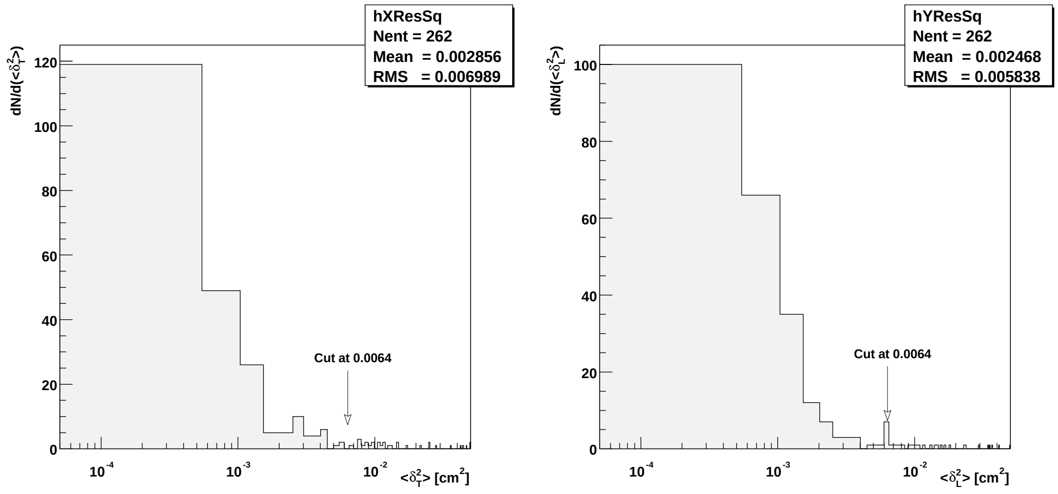

Figure 5.7: *Averaged squared transverse (left panel) and longitudinal residuals for reconstructed tracks, using only 6 middle pad rows. ($V_A = 1200\ V, V_F = 10\ V$)*

of max ADC. Fig. 5.12 shows the pad and time bin distributions of saturated clusters, and as can be seen saturated clusters are generally wide.

It is possible that the saturation observed to some extent is due to δ-electrons from the ionization process in the gas of the TPC. Several of the groups of sequences that generate saturated clusters typically have a tail, often on just one side as in fig. 5.13, where the tail is along the pad row. A δ-electron with energy in the range of keV is likely to lose all its energy in a few cm in the gas, and may possibly explain the tail. This tail in fig. 5.13 is about 13 pads, i.e. $\sim 4.5\ cm$.

5.3.4 Summary of cuts

Going through the available data files, I have found it necessary to introduce several cuts in the tracks and clusters. The following cuts are applied to data used in plots throughout the rest of the analysis:

Multi-track cut: Only single track events are considered.

Angular cut: Tracks with angles β and λ above $+5°$ and below $-5°$ and their corresponding clusters are discarded.

Row cut: Hits in pad rows $1-4$ and $11-14$ are discarded and not used in track finding.

RMS residual cut: Tracks with RMS residuals $\delta_{T,RMS} > 0.08\ cm$ or $\delta_{L,RMS} > 0.08\ cm$ and their corresponding clusters are discarded.

Saturation cut: Clusters with more than 1 ADC value above 700 are discarded and not used in track finding.

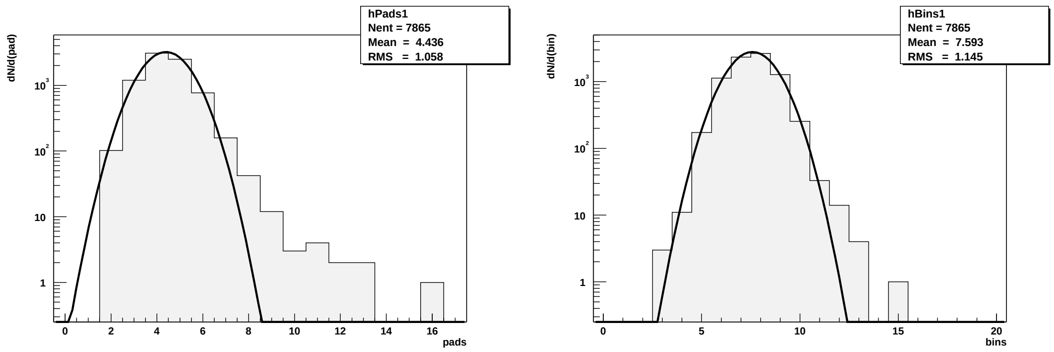

Figure 5.8: *Distributions of number of pads and number of time bins in each cluster for all available voltage settings, both distributions fitted with Gauss curves.*

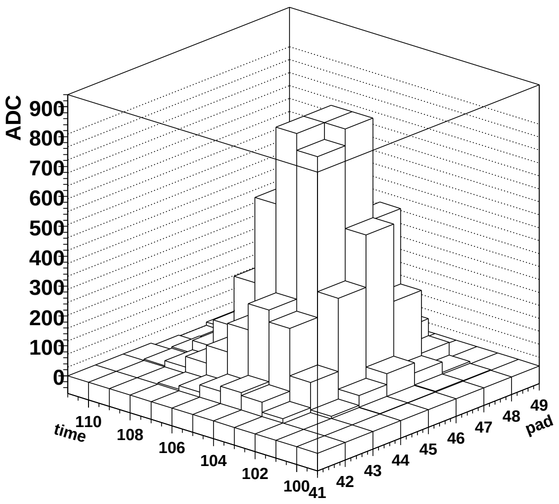

Figure 5.9: *Sequences read from data file from which the cluster finding algorithm creates a 6-pad cluster. ($V_A = 1650\ V, V_F = 700\ V$)*

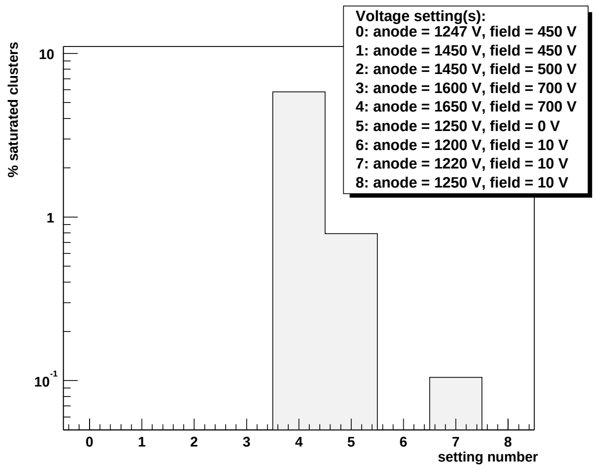

Figure 5.10: *Percentage of saturated clusters for the tested voltage settings. A cluster is considered saturated when it has more than 1 ADC value above 700.*

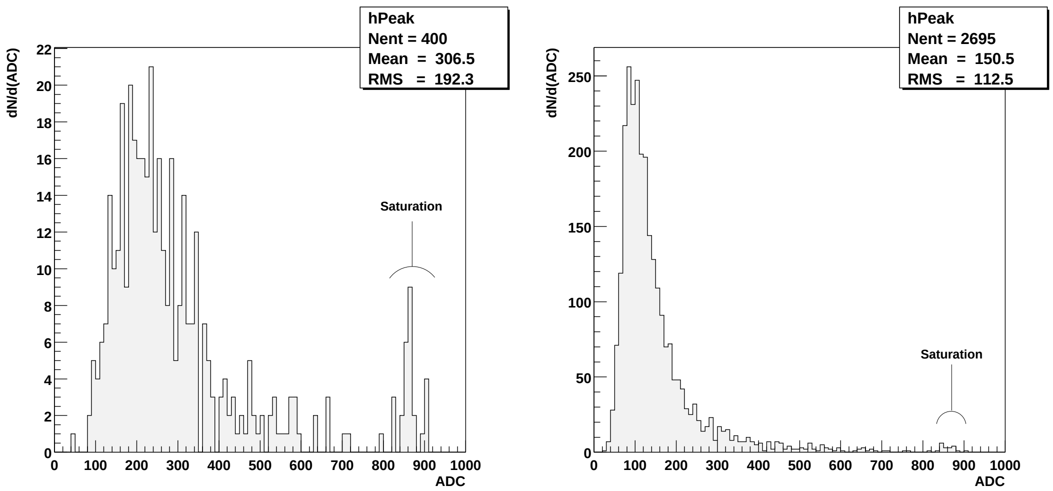

Figure 5.11: *Distribution of max ADC of clusters for ($V_A = 1650$ V, $V_F = 700$ V) (left panel) and ($V_A = 1250$ V, $V_F = 0$ V). The saturation is seen as the upper limit on ADC values in both plots.*

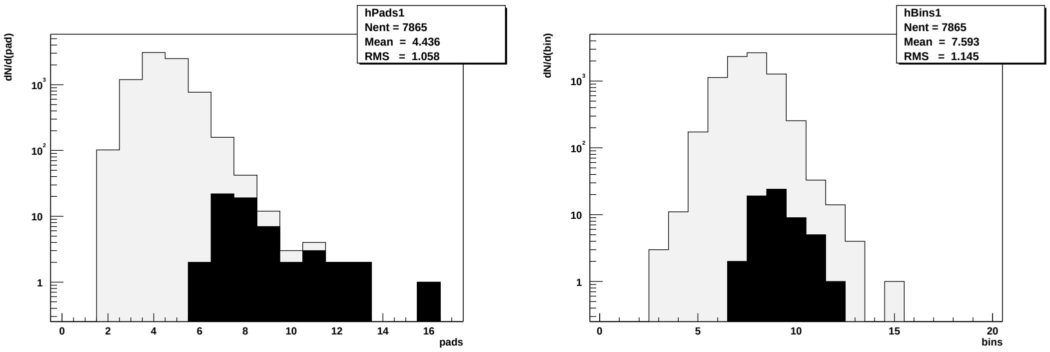

Figure 5.12: *Distributions of number of pads and number of time bins in each saturated cluster (black) and all clusters for all available voltage settings.*

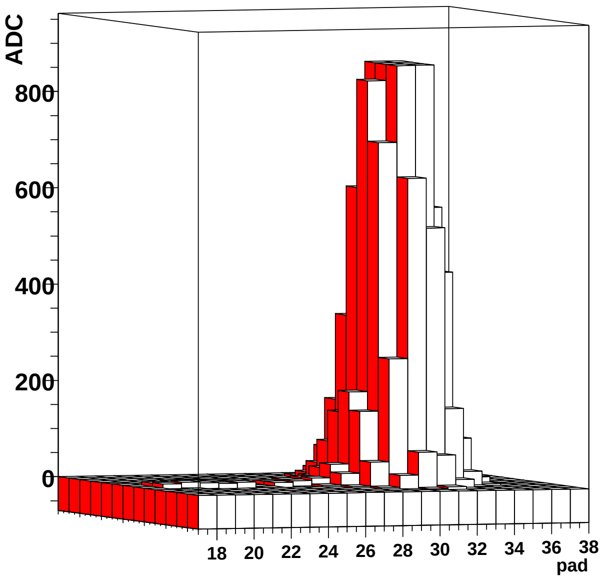

Figure 5.13: *Sequences read from file that result in a cluster stretching over 11 pads. A possible reason for the long tail along the pad row is a δ-electron with velocity component in the x direction.*

5.4 Cluster size

The TPCs have been designed with a gap between anode wire and pad plane of 4.5 mm. As a result of this choice, the TPCs favor clusters with 4-5 pads in most of the voltage settings tested so far, as can be seen from fig. 5.8. The number of pads increases with amplification around the anode wires. This can be seen in figs. 5.14 where the relative distribution of clusters with 2, 3, 4 and more than 4 pads is plotted for different anode voltage settings.

In general, the more pads read out, i.e. the more pads in a cluster, the more noise is included in the data. This noise mainly comes from the read-out electronics. One should therefore, as a rule of thumb, emphasize the clusters with a low number of pads. However, in order to do a Gauss fit along a pad row, one needs signals from at least 3 pads. The most probable number of pads in a generated cluster should therefore be 3. From figs. 5.14 one can see that at ($V_A = 1200\ V, V_F = 10\ V$) there are equally many 3- and 4-pad clusters, and from the results for higher anode voltages, on can assume that in a range in V_A below $V_A = 1200\ V$, and with $V_F \approx 10\ V$, 3-pad cluster will dominate. In order to enhance the number of 3-pad clusters, one could therefore possibly operate the T1 at a lower anode voltage, e.g. $V_A = 1100 - 1150\ V$ and field wires at $V_F = 0 - 10\ V$.

Lowering the voltage, one may face loss in efficiency. It is therefore a question whether anode voltages down toward $1100 - 1150\ V$ limits the efficiency of the T1. As shown in table 5.2 the change made to the cluster finding algorithm has, it seems, improved efficiency at low voltage settings. Therefore, from the numbers in this table, there is no sign of efficiency loss at low voltages.

A loss in efficiency should also affect the percentage of reconstructed tracks per event. By dividing the number of reconstructed tracks by the number of events for any voltage setting, one should be able to see if the investigated settings show any loss in efficiency at lower voltages. Table 5.3 shows a summary of the number of recorded events and reconstructed tracks for the different voltage settings. Especially when comparing the settings tested in March 2000, with constant $V_F = 10\ V$, there is no sign of loss in efficiency when going from $V_A = 1250\ V$ down to $V_A = 1200\ V$. Therefore it may also be possible to lower the anode voltage further, down to a voltage where 3-pad clusters become dominant, without significant loss in tracking efficiency.

5.4.1 Drift distance dependence

The TPCs in BRAHMS have a drift volume which allows a cloud of electrons to drift not more than 20 cm. As the cloud drift towards the read-out region in the upper part of the cage, they are subject to their mutual repulsion and collisions with gas atoms and molecules. Both these effects lead to a widening of the cloud along its path, both in transverse and longitudinal directions. As the electric field is along the longitudinal direction, the widening in transverse direction is reduced to some extent, but not more than it should be possible to detect.

In theory the following relations between width of clusters and drift distance have been established [Loh91]

Anode voltage, V_A [V]	Field voltage, V_F [V]	No. events	No. reconstructed tracks	Percentage of reconstr. tracks per event
1247	300	42	0	0
1450	450	501	49	9.8
1450	500	285	24	8.4
1600	700	499	44	8.8
1650	750	871	71	8.2
1250	0	2842	489	17.2
1200	10	1215	226	18.6
1220	10	879	162	18.4
1250	10	721	110	15.3

Table 5.3: *Number of events, number of reconstructed tracks and percentage of reconstructed tracks per event for each of the tested voltage settings.*

$$\sigma_T^2 = \sigma_{PRF}^2 + D_T^2 \cdot s_{Drift} + \frac{l^2 \cdot tan^2(\beta)}{12} + \frac{d^2 \cdot (tan(\alpha) - tan(\Psi))^2}{12} \cdot cos^2(\alpha) \tag{5.3}$$

$$\sigma_L^2 = \sigma_0^2 + D_L^2 \cdot s_{Drift} + \frac{l^2 \cdot tan^2(\lambda)}{12} \tag{5.4}$$

Here σ_T and σ_L are the transverse and longitudinal width, respectively, $\sigma_{PRF} = \sigma_x$ in the pad response function, eqn. 3.3, σ_0 is the minimal longitudinal width, D_T and D_L are diffusion coefficients and s_{Drift} is drift distance. l is the length of a pad and d is the distance between two adjacent anode wires. The angles β and λ are the previously mentioned angles between track and z-direction in the pad plane and the dip angle of the track, respectively. Angle α is the angle between the normal to the anode wires and the projection of the track in the pad plane, which in the BRAHMS TPCs is equal to β. Angle Ψ is the Lorentz angle[2].

As a result of the angular cuts applied, the angular dependence from α, β and λ on the width of clusters can be neglected. Since the TPCs do not have any applied magnetic field, $\Psi = 0$, resulting in the more compact equations

$$\sigma_T^2 = \sigma_{PRF}^2 + D_T^2 \cdot s_{Drift} \tag{5.5}$$

$$\sigma_L^2 = \sigma_0^2 + D_L^2 \cdot s_{Drift} \tag{5.6}$$

σ_0 can also be expressed by

[2] The Lorentz angle applies to cases where charged particles drifting in an electric field are also subject to a magnetic field. The Lorentz angle is defined as the angle between the electric field and the drift velocity.

$$\sigma_0^2 = \left(\frac{\sigma_{Shaper}^{FWHM}}{2.36}\right)^2 + \left(\frac{\Delta_{TB}}{\sqrt{12}}\right)^2 \tag{5.7}$$

where σ_{Shaper}^{FWHM} is the width of the shaper signal, and Δ_{TB} the drift distance corresponding to a time bucket.

At first, plotting the with of clusters as function of drift distance for all track clusters, no matter the number of pads in each cluster, one can see that diffusion is very small, both in transverse and longitudinal directions. In figs. 5.15 the clusters used to reconstruct tracks are divided into 5 groups depending upon the drift length. Thereafter average transverse and longitudinal width of clusters in each group is plotted as function of averaged drift distance. The number of clusters in each group is as close to identical as possible.

From fig. 5.15 one can see that the change in width of clusters is small, only a few percent. Typically when looking at the other voltage settings a 10% change from the lowest to the highest averaged width is found, in transverse and longitudinal directions. It has been argued that when investigating the influence from drift distance on cluster parameters, one should always include all track clusters. Otherwise, due to diffusion the result would be biased. I.e. if one only looks at 4-pad clusters and plots their width as a function of drift distance, the plot will be biased since a cloud in the bottom of the TPC with "potential" of generating a 4-pad clusters, will diffuse and generate a wider clusters when read out.

Figs. 5.15 rather seem to allow investigation of at least smaller groups of clusters, since the diffusion is only a 10 % effect. When looking at the distribution of pads in track clusters in figs. 5.16, one find that 4- and 5-pad clusters make up 80 % of all track clusters in the $(V_A = 1250\ V, V_F = 0\ V)$ settings, while 85 % of the track clusters in the $(V_A = 1200\ V, V_F = 10\ V)$ setting are 3- or 4-pad clusters. One would therefore not do any big mistake by making plots with only these groups of clusters.

In the following I have therefore on several occasions plotted or used results generated from limited groups of clusters. At each setting these groups include clusters with only certain numbers of pads, and in that setting they account for more than 80% of the track clusters. They are chosen from the distribution of number of pads in each cluster, i.e. from the numbers of pads with highest probability. Selecting a limited group of clusters, that however account for a significant percentage of all clusters in a setting, one is able to study the effect from particularly wide or particularly narrow clusters.

From figs. 5.15 there seems to be a limited dependence for transverse width and a stronger dependence for longitudinal width. Looking through all settings it is generally found that longitudinal width is close to the expected behavior with increasing drift distance, while the transverse width goes up or down in an unsystematic way. Plotting squared cluster widths for the limited groups of clusters does not alter the dependence significantly.

Using the limited groups of clusters at each voltage setting, the longitudinal width of clusters has been plotted. Table 5.4 summarizes the resulting longitudinal diffusion coefficients and σ_0, i.e. the lower limits for σ_L. Theoretically from eqn. 5.7 $\sigma_0 = 1.5\ mm$. Looking specifically at the $(V_F = 10\ V)$ settings, there seems to be an increase in D_L with increasing anode voltage. This effect is expected and due to the fact that at higher anode voltages the electrons gain higher energy during amplification and thus the electron cloud gets wider.

V_A **[V]**	V_F **[V]**	**No. pads in plotted clusters**	**(No. plotted clusters) / (all clusters) [%]**	D_L $[\mu m/\sqrt{cm}]$	σ_0 $[mm]$
1450	450	3-5	91.9	$(2.1 \pm 0.4) \cdot 10^2$	2.3 ± 0.6
1450	500	3-4	91.2	$(2.3 \pm 0.6) \cdot 10^2$	2.0 ± 0.6
1600	700	4-5	80.1	$(1.7 \pm 0.5) \cdot 10^2$	2.3 ± 0.5
1650	750	5-6	82.7	$(2.1 \pm 0.4) \cdot 10^2$	2.3 ± 0.5
1250	0	4-5	80.4	$(2.4 \pm 0.1) \cdot 10^2$	2.3 ± 0.3
1200	10	3-4	84.9	$(2.0 \pm 0.2) \cdot 10^2$	2.0 ± 0.3
1220	10	3-4	80.7	$(2.1 \pm 0.2) \cdot 10^2$	2.1 ± 0.3
1250	10	4-5	86.7	$(2.4 \pm 0.3) \cdot 10^2$	2.2 ± 0.4

Table 5.4: *Squared longitudinal diffusion coefficients and σ_0 for groups of clusters that account for more than 80 % of all clusters at the given voltage settings.*

From plots of the squared transverse cluster width as function of drift distance, the gradient of the squared width, $d\sigma_T/ds_{Drift} = D_T^2$, is found to vary between $(-3.5 \pm 1.2)\ \mu m^2/cm$ and $(2.1 \pm 1.4)\ \mu m^2/cm$. There does not seem to be any systematic behavior for D_T^2. It seems that the dependence from drift distance on the transverse cluster width is somewhat farther from consistency with theoretical predictions than for the longitudinal cluster width.

In figs. 5.17 are shown some estimates for the transverse and longitudinal diffusion coefficients as function of reduced drift fields, E/P, where P is atmospheric pressure measured in atm. In the case of BRAHMS' TPCs they are operated at 1 atm pressure, so that the values of their reduced drift fields equal the ones of their drift fields. The T1 has a drift field of $E = 250\ V/cm$, and so the results in figs. 5.17 have to be extrapolated some 50 V. Comparing with results in table 5.4, one can see that the values of D_L from the cosmic data are not far from the estimate. I.e. D_L in some settings is somewhat below the estimated value, but not more than acceptable. Comparison of D_T does not make any sense as it D_T^2 in many settings has negative value.

5.4.2 Angular dependence

Finally, it can be seen from eqn. 5.3 that the squared transverse width depends quadratically on $tan(\beta)$. For once the general limits of $\pm 5°$ for β and λ is abandoned and increased to $\pm 20°$, as was also done in figs. 5.3. Plotting squared transverse residuals as function of $tan(\beta)$ one can see that there is an obvious dependence as expected, figs. 5.18.

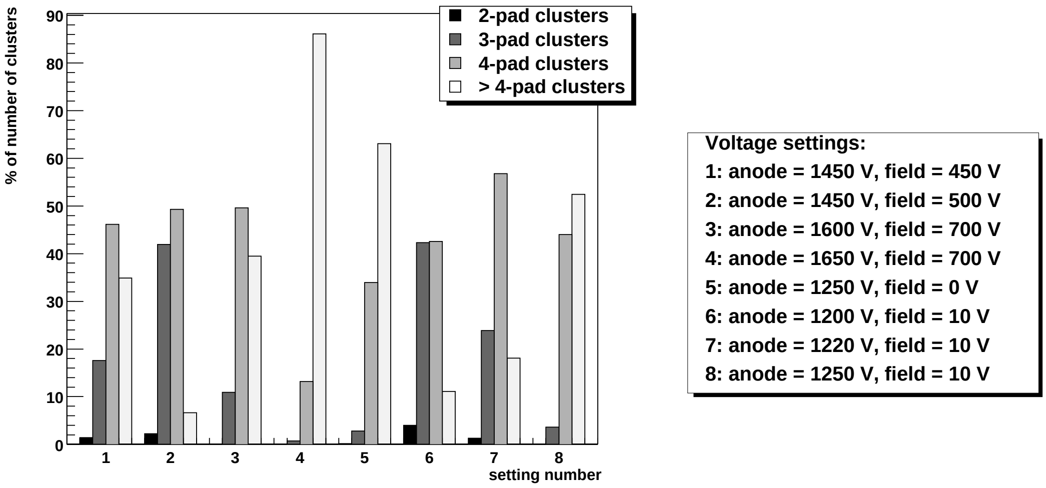

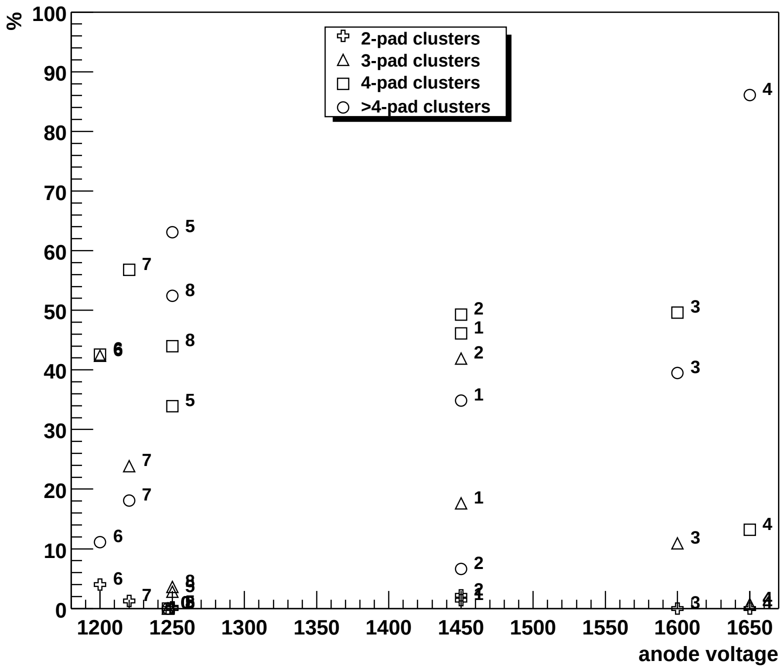

Figure 5.14: *Relative distribution of number of pads in track clusters as function of anode voltage. The numbers next to the markers in the lower plot corresponds to the setting number.*

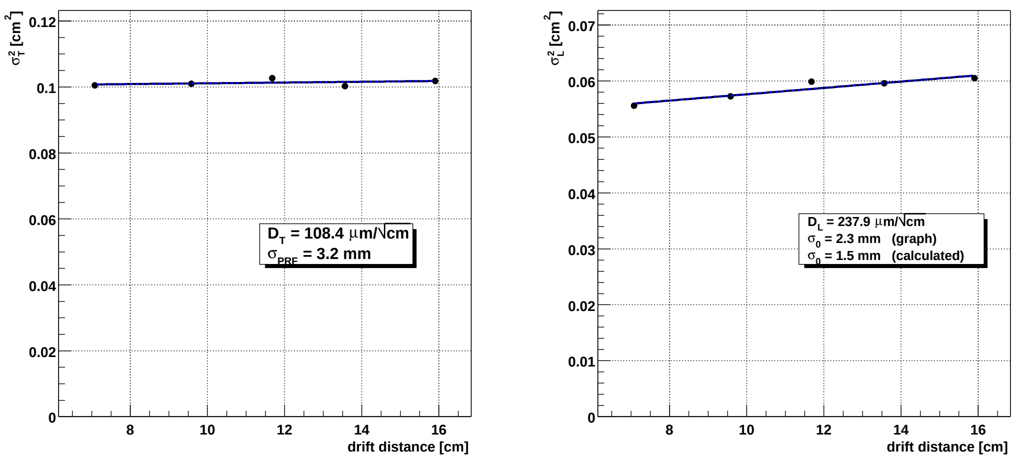

Figure 5.15: *Width of clusters along transverse (left panel) and longitudinal directions, for the* ($V_A = 1250\ V, V_F = 0\ V$) *setting.* D_T *and* D_L *are diffusion coefficients,* σ_{PRF} *the width of the pad response function and* σ_0 *the minimal width in longitudinal direction of any cluster.*

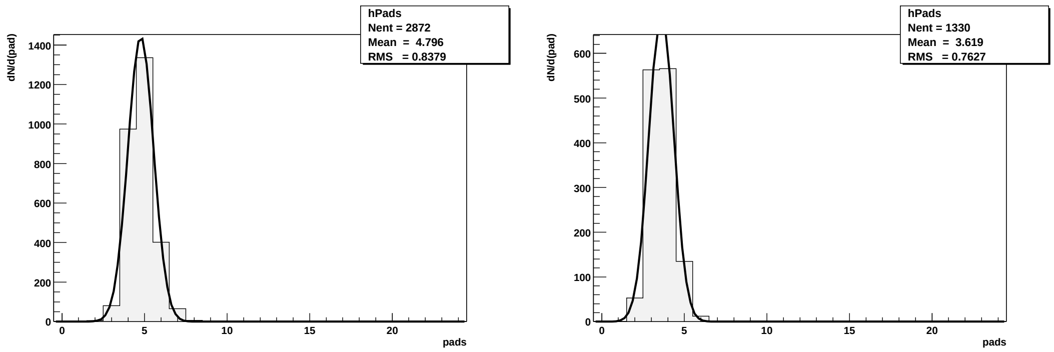

Figure 5.16: *Distribution of number of pads in clusters for* ($V_A = 1250\ V, V_F = 0\ V$) *(left panel) and* ($V_A = 1200\ V, V_F = 10\ V$).

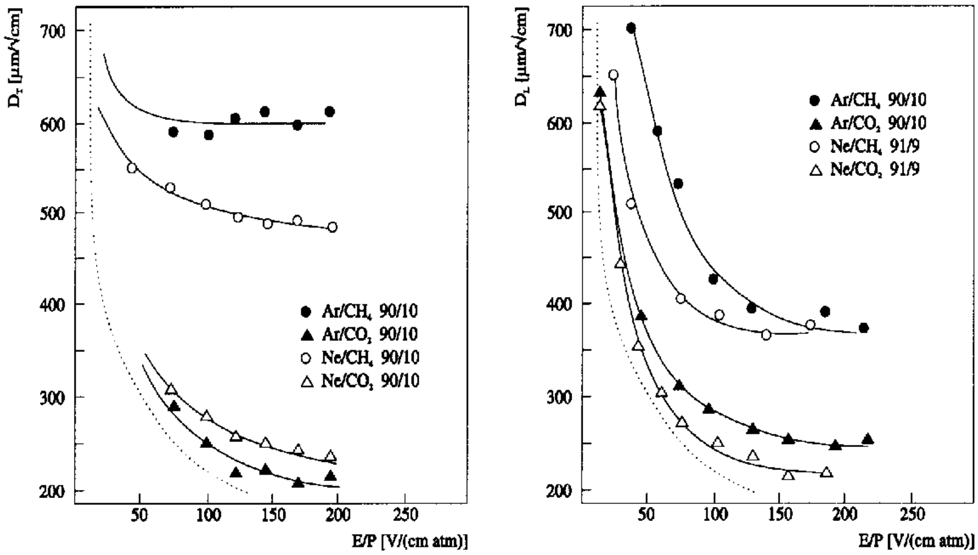

Figure 5.17: *Estimated diffusion coefficients in transverse (left panel) and longitudinal directions for different values of reduced drift field E/p and different gas mixtures. The dotted line is the thermal limit [Küh95].*

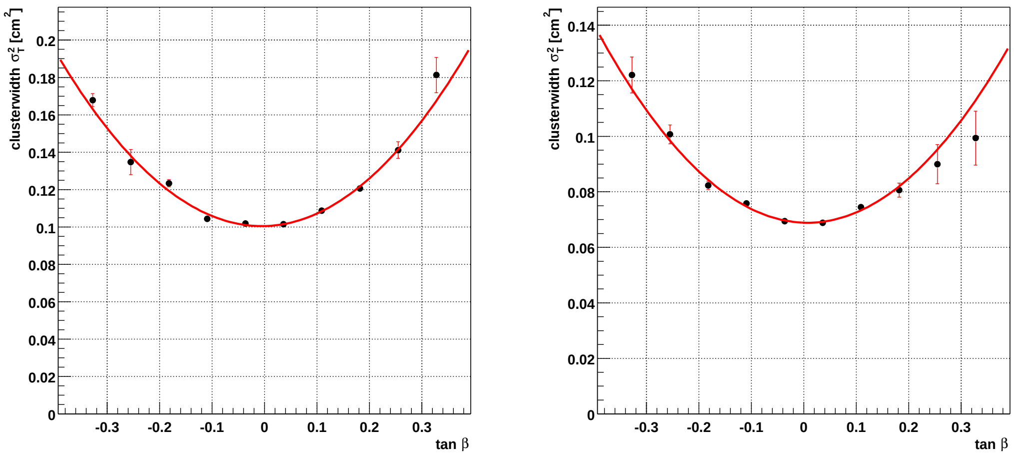

Figure 5.18: *Transverse width of clusters as function of tan(β) for all clusters in the ($V_A = 1250\ V, V_F = 0\ V$) (left panel) and ($V_A = 1200\ V, V_F = 10\ V$) settings. Angles β and λ for tracks are in these plots limited to $\pm 20°$. A parabola is fitted to the experimental data at both settings.*

5.5 Cluster charge

The charge loss in an interaction between an incoming particle and the gas follows a Landau distribution [Leo94]. The distributions for max ADC value and total charge in clusters should therefore also follow Landau distributions, i.e. if the amplification in the TPC is in the proportional range. As shown in the former plots, figs. 5.11, the distribution of max ADC in clusters is a clear Landau distribution except for the saturation at high ADC values. However, saturated clusters are now eliminated. In figs. 5.19 the total charge in clusters is plotted, also showing a Landau distribution.

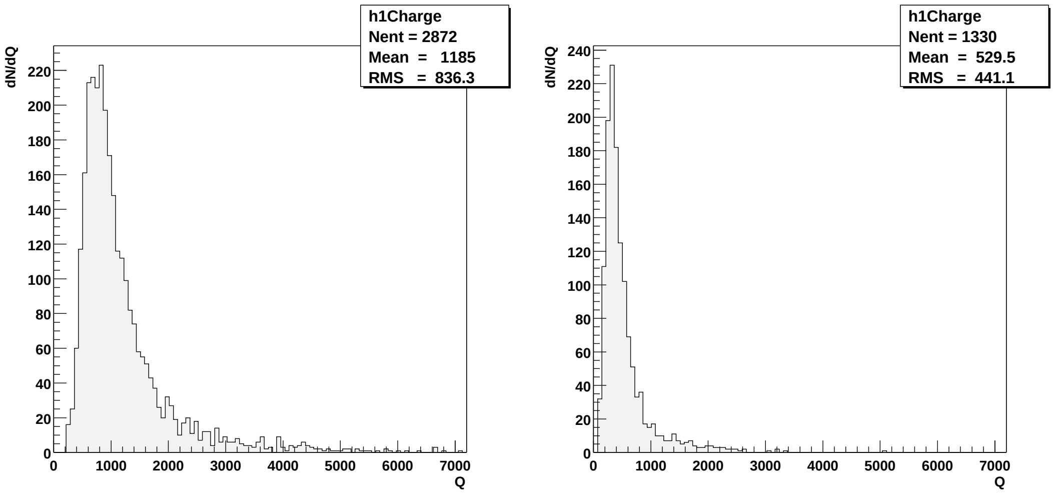

Figure 5.19: *Distribution of total charge in a cluster for ($V_A = 1250\ V, V_F = 0\ V$) (left panel) and ($V_A = 1200\ V, V_F = 10\ V$).*

Since the origin for both the distribution of max ADC and for total cluster charge is the Landau distribution of the charge loss in a particle-gas interaction, there should be a strong correlation between these two values in any given cluster. One can see in fig. 5.20 that there is a clear a correlation between max ADC and total cluster charge. Similar patterns are found also at other voltage settings.

The max ADC of a cluster is also expected to depend on the amplification voltage. Therefore there should be an increase in the max ADC value with increasing anode voltages. Plotting averaged max ADC value for the available voltage settings, fig. 5.21 one can see two distinct patterns. The averaged max ADC values in the settings of this year (2000), with field wires at 0 or 10 V seem to follow one curve, while the averaged max ADC values from last year settings with V_F from 450 V to 700 V follow close to another curve. Both curves are of exponential kind, indicating rapid increase in amplification as function of voltage.

Fig. 5.21 also shows a reduced max ADC at higher field voltages. This feature one may expect as the field gradient decreases when increasing V_F and at the same time keeping V_A constant.

As the cloud drifts toward the proportional region, the electrons are subject to electron

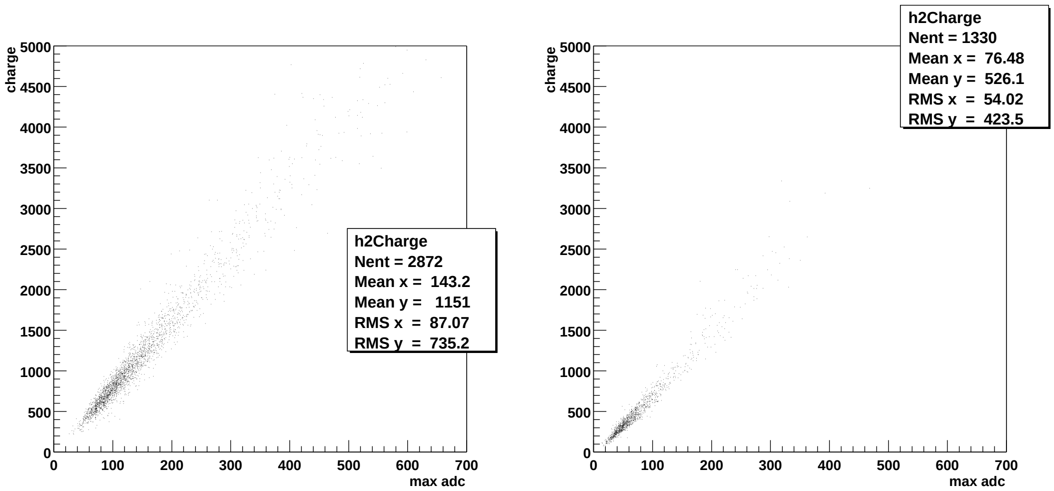

Figure 5.20: *Correlation between max ADC and total charge in a cluster for (V_A = 1250 $V, V_F = 0$ V) (left panel) and ($V_A = 1200$ $V, V_F = 10$ V).*

capture in the gas. The amount of electron capture depends very much on the gas mixture. As a result of electrons being picked up along the drift path of the cloud, one should be able to detect a reduction in the average charge of clusters for clusters generated from clouds with longer drift paths.

The amount of electron capture with a given gas mixture may allow to get some knowledge about the purity of the gas. Before the data is taken, T1 has been flowing gas for hours to exchange air with the $Ar - CO_2$ mixture. Figs. 5.22 show the average charge of track clusters as a function of drift distance, for all clusters and for the above mentioned groups of clusters (i.e. depending on the number of pads in the clusters.)

Worth noticing in these plots is that plotting total cluster charge as function of drift distance for all clusters the dependence is not linear in drift distance. However, doing the same plot for the clusters with dominating width, i.e. 4-5 pads at ($V_A = 1250$ $V, V_F = 0$ V) and 3-4 pads at ($V_A = 1200$ $V, V_F = 10$ V) the dependence is much closer to linear.

In fact, doing the same plot for all clusters up to and including 5 pads at (V_A = 1250 $V, V_F = 0$ V), and up to and including 4 pads at ($V_A = 1250$ $V, V_F = 0$ V), does not change much from the plots on the right hand side in figs. 5.22. But when also including up to 7-pad clusters for the ($V_A = 1250$ $V, V_F = 0$ V) setting and up to 6-pad clusters in the ($V_A = 1250$ $V, V_F = 0$ V) setting, figs. 5.23, the dependence on drift distance gets unclear. Similar results is found when plotting cluster charge as function of drift distance in other settings. It seems that clusters that are wide in the transverse direction, have some feature resulting in unusual amount of electron capture. I have not been able to identify the reason for this feature.

Also to notice is the very big loss of charge over only a few centimeters. The lower right panel on figs. 5.22 shows a decrease of almost 24% in 6 cm drift. Such a high charge loss indicate that there may have been too much impurities in the gas mixture. As a gas of better purity will be used during physics runs in the IR, the amount of energy loss may

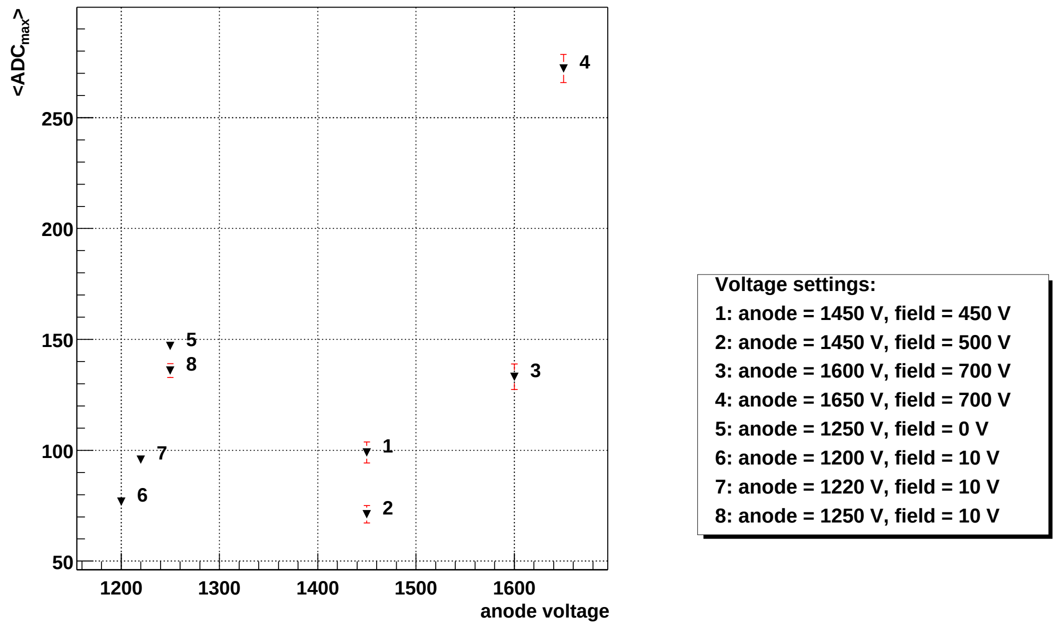

Figure 5.21: *Max ADC of clusters as function of anode voltage. Settings 1-4 have V_F in the range $450 - 700\ V$, while settings 5-8 have V_F in the range $0 - 10\ V$.*

decrease. However, if there is a significant amount of impurity in the gas, it may also be due to leakage, in T1 itself or in the tube system providing gas to T1. I have tried to look for differences in the charge loss for the different tests, to see if any differences in the test setups could explain the charge loss. Table 5.5 lists the charge loss in 6 cm, from $s_{Drift} = 14\ cm$ to $s_{Drift} = 8\ cm$, at the different voltage settings. From the table there may seem to be a somewhat higher loss in the data from March, especially if one looks at the loss in the limited group of clusters at each setting. However, in clusters from the December data there is significant fluctuations in charge loss. It is therefore hard to say if the increased loss in clusters from the March data is due to increased amount of impurity or other factors.

Anode voltage, V_A **[V]**	**Field voltage,** V_F **[V]**	**Charge loss [%] (All clusters)**	**No. pads in limited clusters**	**Charge loss [%]**
1450	450	-16.4	3-5	-11.7
1450	500	1.9	3-4	-5.6
1600	700	-18.9	4-5	-15.6
1650	750	-12.6	5-6	-8.6
1250	0	-8.4	4-5	-8.5
1200	10	-33.6	3-4	-23.7
1220	10	-13.5	3-4	-13.1
1250	10	-16.1	4-5	-17.1

Table 5.5: *Charge loss over 6 cm drift length, i.e. between 14 cm and 8 cm from read-out, for all track clusters and limited number of track cluster at the different voltage settings. The first 4 settings were tested in December 1999, the* 5^{th} *setting in January 2000 and the last 3 in March 2000.*

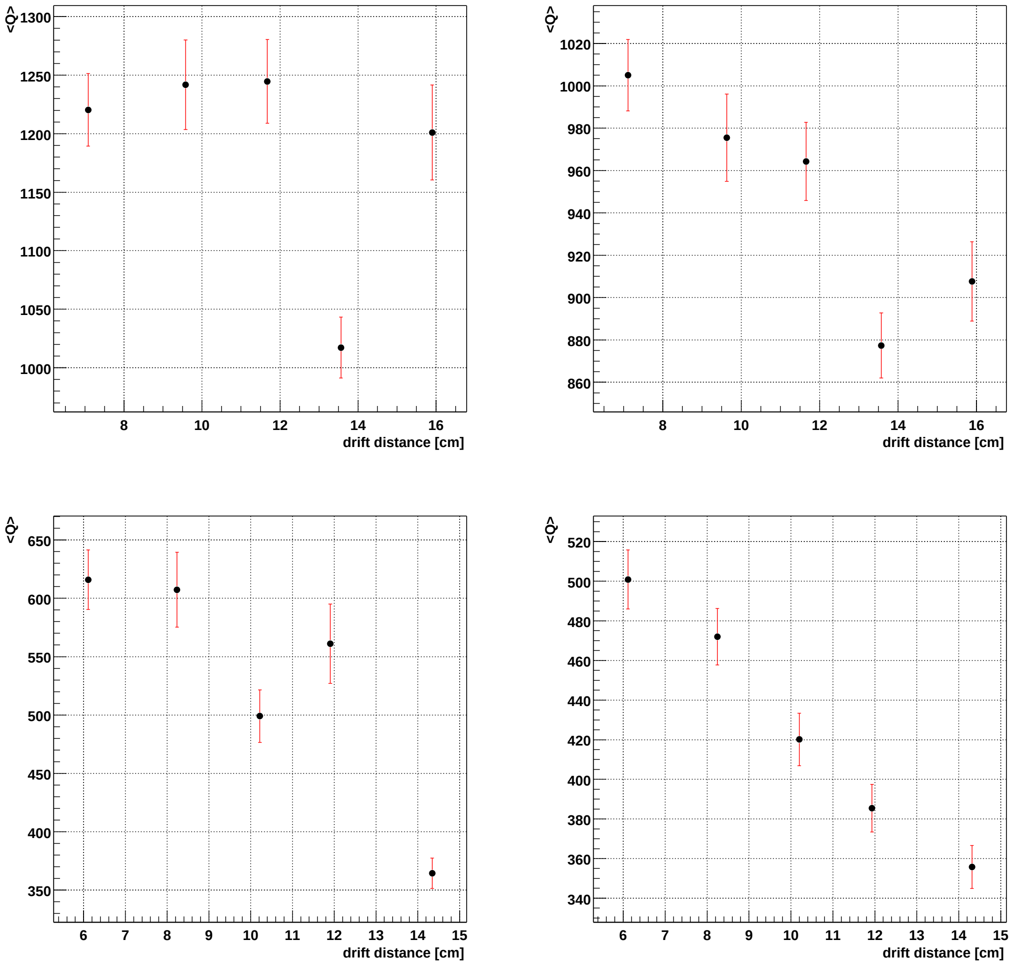

Figure 5.22: *Averaged charge in track clusters as function of drift distance for* (V_A = 1250 V, V_F = 0 V) *(upper panels) and* (V_A = 1200 V, V_F = 10 V). *The left panels show plots where all track clusters are included. In the upper right panel only 4- and 5-pad clusters are included, while the lower right plot is for 3- and 4-pad clusters only.*

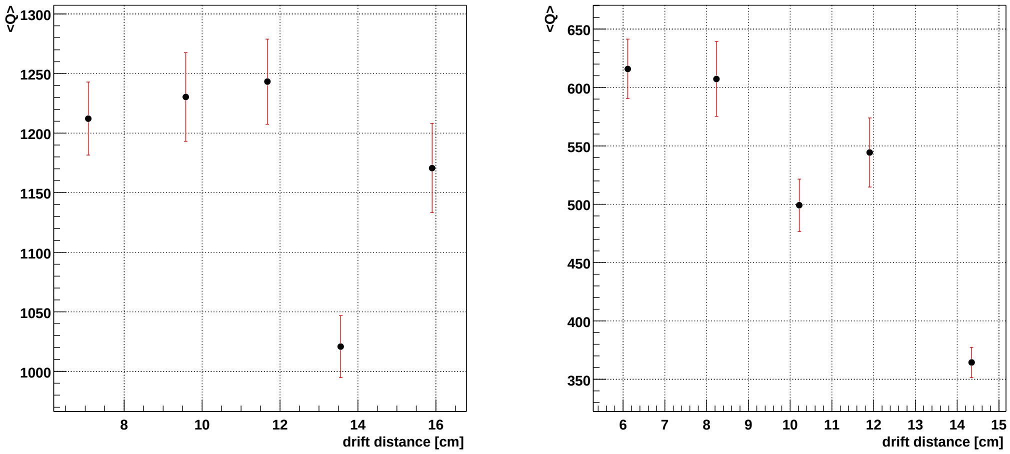

Figure 5.23: *Averaged charge in track clusters as function of drift distance for clusters with 3-7 pads at ($V_A = 1250\ V, V_F = 0\ V$) (left panel) and 2-6 pads at ($V_A = 1200\ V, V_F = 10\ V$).*

5.6 Residuals

Residuals generally also depend on drift distance. Landau fluctuations of cluster centroids, due to electron-gas interactions along the path from the ionized track to the read-out region, make the square of residuals in both transverse and longitudinal directions depend linearly on the drift distance. The theoretical predictions for transverse and longitudinal residuals, δ_T and δ_L respectively, are given by

$$\delta_T^2 = \delta_{T,0}^2 + \frac{D_T^2 \cdot s_{Drift}}{l \cdot N_{e^-,tot}} + \frac{l^2 \cdot tan^2(\beta)}{12 \cdot N_{e^-,eff,Pad}} + \frac{d^2 \cdot (tan(\alpha) - tan(\Psi))^2}{12 \cdot N_{e^-,eff,Wire} \cdot N_{Sense}} \cdot cos^2(\beta - \alpha) \quad (5.8)$$

$$\delta_L^2 = \delta_{L,0}^2 + \frac{D_L^2 \cdot s_{Drift}}{l \cdot N_{e^-,tot}} + \frac{l^2 \cdot tan^2(\lambda)}{12 \cdot N_{e^-,eff,Pad}} \quad (5.9)$$

Here $N_{e^-,tot}$ is the number of electron-ion pairs per cm track length, $N_{e^-,eff,Wire}$ is the number of primary charge units along an anode wire on which the cluster charge is deposited, $N_{e^-,eff,Pad}$ is the number of primary electrons in the gas "column" below the pad and N_{Sense} is the number of anode wires crossing the pad. As for the width of clusters the angular terms may be neglected, giving the following expressions

$$\delta_T^2 = \delta_{T,0}^2 + \frac{D_T^2 \cdot s_{Drift}}{l \cdot N_{e^-,tot}} \quad (5.10)$$

$$\delta_L^2 = \delta_{L,0}^2 + \frac{D_L^2 \cdot s_{Drift}}{l \cdot N_{e^-,tot}} \quad (5.11)$$

Plotting squared residuals as function of drift distance for all clusters in the ($V_A = 1250\ V, V_F = 0\ V$) and ($V_A = 1200\ V, V_F = 10\ V$) settings, figs. 5.24, one can see there is an obvious dependence for transverse residuals. For longitudinal residuals, on the contrary, the dependence is not that obvious. As a general characteristic the dependence upon drift distance for transverse residuals seem to be closer to the theoretical prediction than for longitudinal residuals.

Also here the same limits on clusters as when plotting the drift distance' influence on width of clusters have been investigated. The plots in figs. 5.25 show that there is some improvement in longitudinal dependence when plotting the most common clusters at a given voltage setting. Typically, when plotting squared residuals as function of drift distance for the most frequent numbers of pads in clusters at a given voltage setting, the results which are far from the theoretical description get closer. The results that are already close to the theoretical prediction for all clusters in a given voltage setting usually do not change much when plotting for the limited numbers of clusters.

However, the plots of squared residuals as function of drift distance show promising results of the overall resolution in T1. The "minimal" residuals in transverse and longitudinal directions, $\delta_{T,0}$ and $\delta_{L,0}$ respectively, are often below 350 μm which BRAHMS Conceptual Design Report assumes for resolution in T1. I call it "minimal" in quotation marks since for some settings, where there seem to be a decrease in residual as function of distance, it is not the actual minimal. It is only the estimated residual at 0 drift distance. $\delta_{T,0}$ and $\delta_{L,0}$ for the different voltage settings are summarized in table 5.6. It remains to see whether resolution below 350 μm is possible using all pad rows.

V_A [V]	V_F [V]	**No. pads in plotted clusters**	**(No. plotted clusters) / (all clusters) [%]**	$\delta_{T,0}$ $[mm]$	$\delta_{L,0}$ $[mm]$
1450	450	3-5	91.9	0.29 ± 0.19	0.25 ± 0.19
1450	500	3-4	91.2	0.17 ± 0.24	0.16 ± 0.24
1600	700	4-5	80.1	0.21 ± 0.17	0.22 ± 0.23
1650	750	5-6	82.7	0.11 ± 0.13	0.19 ± 0.14
1250	0	4-5	80.4	0.22 ± 0.09	0.35 ± 0.12
1200	10	3-4	84.9	0.25 ± 0.13	0.27 ± 0.13
1220	10	3-4	80.7	0.26 ± 0.14	0.20 ± 0.15
1250	10	4-5	86.7	0.30 ± 0.15	0.46 ± 0.19

Table 5.6: *Minimal residuals in transverse and longitudinal direction in groups of clusters that account for more than 80 % of all clusters at the given voltage settings.*

Another way to look at residuals is to plot the distribution of residuals, as is done for the ($V_A = 1250\ V, V_F = 0\ V$) and ($V_A = 1200\ V, V_F = 10\ V$) settings in figs. 5.26. Here the plots are for all clusters. Plotting for the same limited numbers of clusters as has been done earlier does not change the result very much. Table 5.7 summarizes the FWHM values of the Gauss curves fitted from distributions of residuals. From the table one may notice that the distribution of longitudinal residuals is quite broad in the ($V_A = 1250\ V, V_F = 0\ V$) setting, compared to the other settings. This can also be seen in the upper right histogram in figs. 5.26. From reading the log book I have not been able to find an explanation for this feature. One would assume that the $FWHM_L$ in this setting would be rather close to the value of the ($V_A = 1250\ V, V_F = 10\ V$) setting from March this year, but it is actually about 40% bigger. The value of $FWHM_L$ from the ($V_A = 1250\ V, V_F = 10\ V$) setting is rather consistent with the other values.

V_A [V]	V_F [V]	$FWHM_T$ $[mm]$	$FWHM_L$ $[mm]$
1450	450	0.57 ± 0.04	0.63 ± 0.05
1450	500	0.68 ± 0.09	0.59 ± 0.10
1600	700	0.57 ± 0.05	0.62 ± 0.07
1650	750	0.45 ± 0.02	0.53 ± 0.03
1250	0	0.49 ± 0.01	0.83 ± 0.01
1200	10	0.59 ± 0.02	0.58 ± 0.02
1220	10	0.51 ± 0.01	0.61 ± 0.02
1250	10	0.48 ± 0.02	0.59 ± 0.02

Table 5.7: *FWHM of Gauss curves fitted from transverse and longitudinal residual distributions of all clusters in the tested settings.*

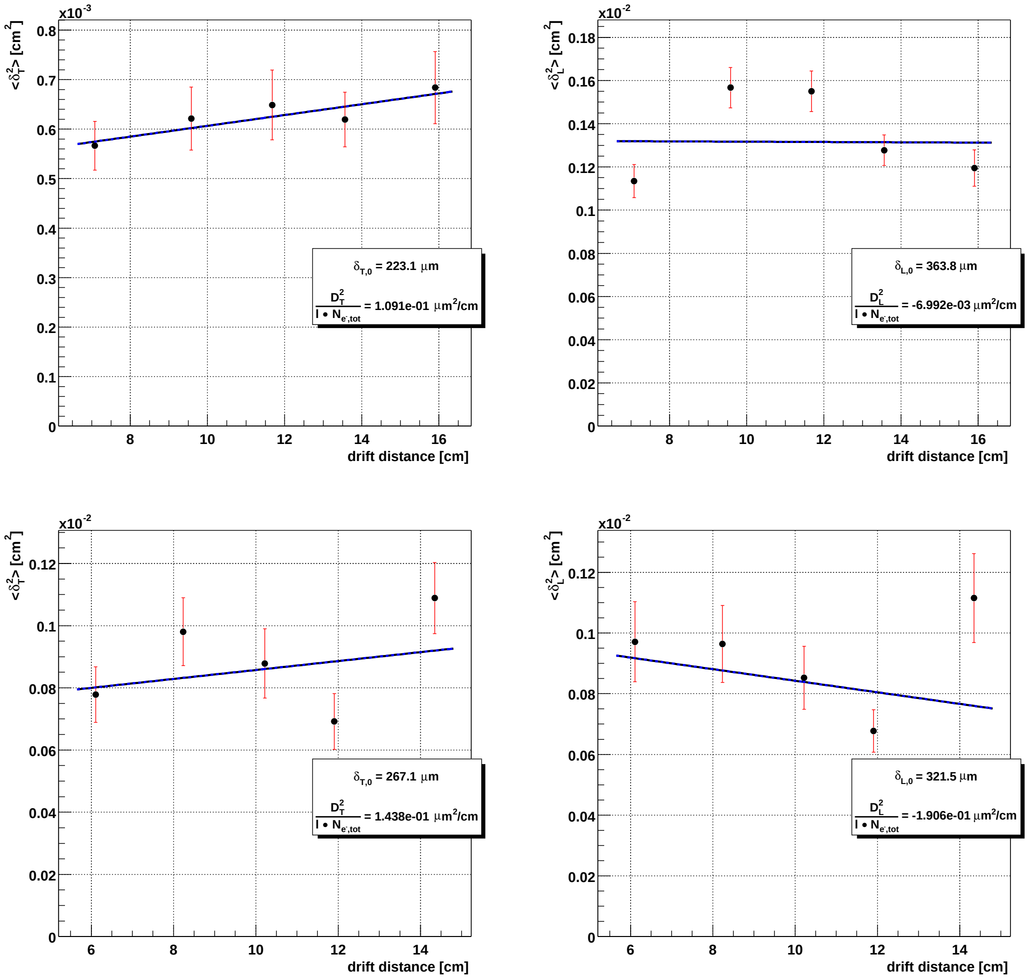

Figure 5.24: *Averaged squared transverse (left panels) and longitudinal residuals as function of drift distance for all clusters in the ($V_A = 1250\ V, V_F = 0\ V$) (upper panels) and ($V_A = 1200\ V, V_F = 10\ V$) settings.*

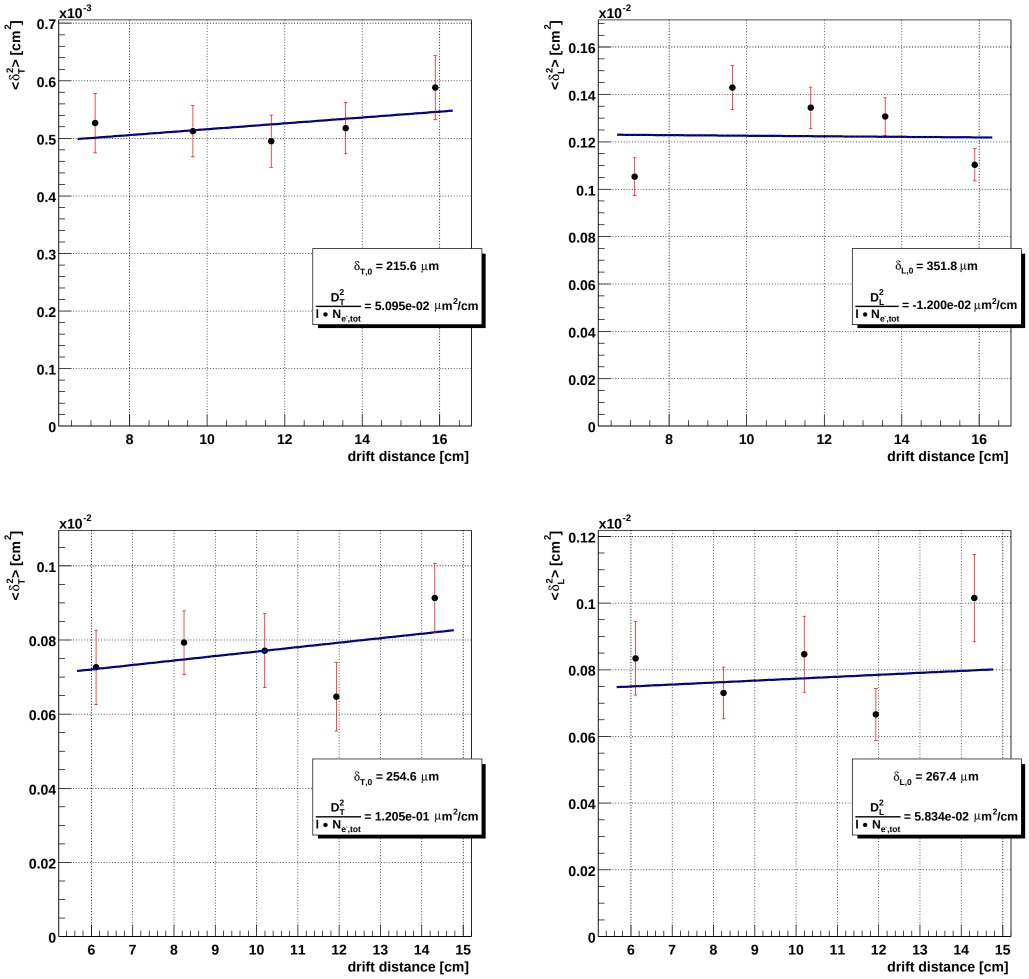

Figure 5.25: *Averaged squared transverse (left panels) and longitudinal residuals as function of drift distance for 4- and 5-pad clusters in the ($V_A = 1250\ V, V_F = 0\ V$) setting (upper panels), and 3- and 4-pad clusters in the ($V_A = 1200\ V, V_F = 10\ V$) setting.*

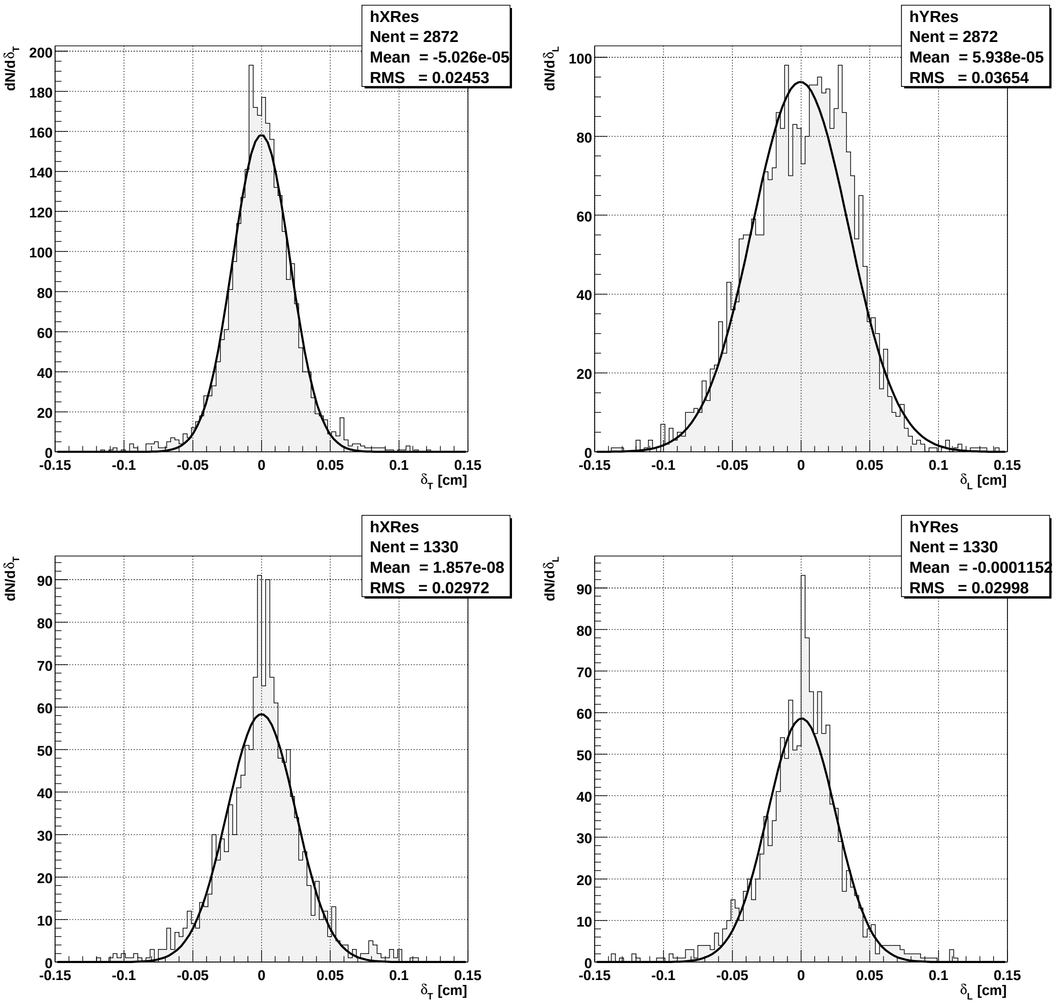

Figure 5.26: *Distribution of transverse (left panels) and longitudinal residuals for all clusters in the ($V_A = 1250$ V$, V_F = 0$ V) (upper panels) ($V_A = 1200$ V$, V_F = 10$ V) settings. The histograms are fitted with Gauss curves.*

Chapter 6

Conclusion

In chapter 5 several features of T1 have been investigated. In order to get the fullest possible understanding about the functionality of T1, these results have to be combined with results generated by other people in the collaboration.

As mentioned, the reason for the "edge effect" has been identified. Simulations, where appropriate resistors have been substituted for the ones with obviously too high resistances, show promising results. It is however not probable that actual substitution in the TPCs will be done prior to this year's physics run.

There are at least two possible ways to avoid the systematic errors from wrong drift times of electron clouds close to the aluminized drift strips. One way is to do as has been done in this analysis, i.e. not use the pad rows closest to the strips. Using only the 6 middle rows on the test data shows promising results for the resolution in T1. However, during physics runs the entire width of the TPCs will be used. I.e. all pads in a row are likely to get hits, and not only the ones between the trigger slats used in tests. It is therefore probable that pads close to the strips also in the middle rows will show similar behavior as pads in rows 1 and 14.

Also, a low number of hits per track is likely to worsen the momentum resolution, as the angles of the track segment through T1 get increased uncertainty. The amount of increase is not certain. But since 1% momentum resolution for the entire BRAHMS setup is expected, according to the Conceptual Design Report, it is possible that using only 6 pad rows may lead to too high uncertainty in momentum determination.

Alternatively off-line corrections to the drift time may be applied. The correction term will have to be a function of pad number and row number. Simulations with Garfield may provide good estimates of these values. Also the plots of residuals as function of row number may lead towards appropriate values for row correction. Such a correction is probably the best way of dealing with the edge effect at present.

Even though the TPCs have been designed to detect mainly 4- and 5-pad clusters, it may also be possible to alter the voltage settings in order to enhance the number of 3-pad clusters. The results in section 5.4 show that with the alternative cluster selection method applied in this analysis, there does not seem to be any loss in efficiency at the current low limit of anode voltage.

Also, as shown for total cluster charge, cluster width and residuals as function of drift distance, I get some peculiar results when the wider clusters are included. Reducing the width of clusters may lead to results closer to the theoretical predictions.

The chosen voltage settings also affect saturation. With a lower anode voltage there will be a smaller amplification, and thus probably fewer saturated clusters. Especially if there is no significant efficiency loss for clusters with little charge when lowering the anode voltage, this may be a good thing to do.

Finally, since T1 has had problems holding high voltage, lower voltage on the anode and field wires is likely to enhance T1's stability, i.e. lower the frequency of sparks.

However, only test of T1 at lower anode voltages will show if its performance at these voltages is satisfactory. It would be interesting to test T1 at $(V_A = 1100 - 1150\ V, V_F = 0 - 10\ V)$.

If the T1 is to be operated at any of the voltage settings with high ratio of saturated clusters, at least a saturation cut should be included in the cluster finding algorithm. Since a significant portion of the saturated clusters have long tails, many on just one side, it is not easy to find the centroid. In my opinion these clusters should be discarded.

As shown in thesis T1 may be operated with a position resolution of about 300 μm as it is today. According to the Conceptual Design Report this is what is expected for T1.

Appendix A

ROOT

ROOT is an object-oriented framework made at CERN mainly for analysis of data from nuclear and particle physics experiments. The framework is still under developments, and new classes and functionalities are added regularly. In addition to tools for analysis, ROOT also provide features for data acquisition, event reconstruction and generation and detector simulation.

Information about ROOT is available from the ROOT web pages [RoWWW]. From this site root can be downloaded, either in source code or in compiled versions for different operating systems. The site provides documentation, e.g. tutorials and list of classes in ROOT.

In order to install ROOT on a computer system, one can thus either download the source code and compile it, or one can download ROOT compiled for the appropriate operating system. For both installation methods one must download a tar ball compressed with gzip, i.e. a file with suffix ".tar.gz". For my analysis I have used ROOT compiled for RedHat Linux version 6.1. The ROOT version is 2.23/12.

After downloading the tar ball, the installation can be done in one or two steps. The `tar` command can usually also decompress, so installation can be done with the following command on the command prompt[1] from the directory in which the tar ball is placed:

```
> tar -xvzf root_v2.23.Linux.2.2.10.tar.gz
```

Here `root_v2.23.Linux.2.2.10.tar.gz` is the tar ball to be installed. This command un-compresses the tar ball and extracts the ROOT files. A directory called *root* is created in which all extracted files are placed in a hierarchy of subdirectories. (Synopsis for `tar` can vary from one UNIX-based system to another. In case of error the manual should be consulted, i.e. `> man tar`.) Alternatively, installation can be done with:

```
> gunzip root_v2.23.Linux.2.2.10.tar.gz
> tar -xvf root_v2.23.Linux.2.2.10.tar
```

The first command un-compresses the tar ball, while the second command extracts files from the archive and place them in directory *root*.

Before running ROOT two environment variables have to be set in the shell from which ROOT is run either as a interactive session or as a compiled program. The *ROOTSYS*

[1] ">" is not to be typed. It is just to indicate the command prompt.

variable has to be equal to the main ROOT directory, i.e. the directory *root* created in extracting files from the ROOT tar ball. Also the *LD_LIBRARY_PATH* variable has to be set to the directory in *root* where the shared object files are placed. This is typically *root/lib*, which should have many shared object files, with suffix ".so". If the main ROOT directory is placed under */usr/local/* these environment variables can be set with:

```
> setenv ROOTSYS /usr/local/root
> setenv LD_LIBRARY_PATH $ROOTSYS/lib:$LD_LIBRARY_PATH
```

The last command assures that if *LD_LIBRARY_PATH* already has a value, it will no be overwritten. It is also possible to include the two sentenv statements in a file read by the shell on startup. If the Berkeley UNIX C shell, *csh*, is to be used, the statements should be put in *.cshrc* in the users home directory.

ROOT can now be run with command `root` or used in compiled programs. In addition to the ROOT web pages, examples on using ROOT is provided in subdirectories *tutorials* and *test* in the main ROOT directory.

Appendix B

BRAT

B.1 Getting BRAT source code

The BRAT package is programmed by many people in the BRAHMS collaboration. Different people work with different parts of the package, and it is therefore important to keep track of changes done to the source code. To ease this book keeping the reference source code is placed in a *CVS repository* on a computer at the *RHIC Computing Facility* (RCF). From there source code can be downloaded and new source code, new classes or just updates, can be uploaded. CVS keeps track of updates, and it is therefore possible to get access to previous version of the source code.

In order to download the BRAT code from the CVS repository, one needs an *AFS*[1] account on the RCF computer system. An AFS account one can get by contacting managing people at RCF.

Having an AFS account at RCF, with `<user_name>` and `<password>`, the procedure is straight forward. Use a shell to log in to a local computer that also has AFS installed, using commands `rlogin` or `telnet`. At the Department of Physics at the University of Bergen, the machine named *asfys4.fi.uib.no* has AFS installed. Once logged in to the computer with AFS, type the following commands

```
> setenv CVSROOT /afs/rhic/brahms/BRAHMS_CVS
> klog -c rhic -pr <user_name>
Password:
```

As 'Password:' is written on the prompt you enter your password (`<password>`) and go to the directory in which you want to download BRAT, if you have not done it already. Then finally you type

```
> cvs checkout brat
```

Then the most recent version of BRAT is downloaded to you current working directory and placed in subdirectory *brat*. CVS allows also other options [Ced93], but this basic procedure presented above lets you download BRAT in an easy manner. If later update of the source code is requested, just use CVS option `update` instead of `chekout`.

[1]AFS is a file system that makes it possible to include e.g. hard disks on remote computer systems in the local file system.

B.2 Compiling BRAT

When BRAT is downloaded it only contains source files and therefore has to be compiled. However, it contains makefiles for compilation, so eventually only minor changes have to be done.

Before compilation some environment variables have to be set in the shell. These variables could also be included in the users shell initialization files, as mentioned in App. A. Otherwise these environment have to be initialized every time a new shell is started.

BRAT depends on some libraries, but there is a choice in libraries. The *BRAHMS_ARCH* environment variable describes this choice. If you want to compile BRAT with the *glibc2* library, set *BRAHMS_ARCH* to

```
> setenv BRAHMS_ARCH linux
```

If you rather want to compile it with *egcs/gcc* you do

```
> setenv BRAHMS_ARCH linuxegcs
```

The ROOT environment variables in App. A have to be set. I.e. the *ROOTSYS* and *LD_LIBRARY_PATH* have to be set to the mentioned values.

Assuming that the BRAT source code is placed in directory */usr/local/brat*, set the following environment variables and values

```
> setenv BRATSYS /usr/local/brat
> setenv BRATHOME /usr/local/brat
> setenv LD_LIBRARY_PATH $LD_LIBRARY_PATH:/usr/local/brat/lib/BRAHMS_ARCH
```

Make sure the downloaded package includes files *mkconfig.linux* if you want to compile with *libc2* and *mkconfig.linuxegcs* if you want to compile using *egcs/gcc*. If the file you need is missing, copy the one to the other and change names. I.e. if you need *mkconfig.linuxegcs* and only *mkconfig.linux* is present, then do

```
> cp mkconfig.linux mkconfig.linuxegcs
```

Finally, you should be able to compile. Assuming you are in the $BRATSYS directory, */usr/local/brat*, you do

```
> gmake
```

BRAT will then compile, and shared object files are generated in *$BRATSYS/lib/$BRAHMS_ARCH*.

B.3 Starting a BRAT interactive session

BRAT classes can be used in the same way as original ROOT classes. I.e. they can be used in compiled programs or in an interactive session. In an interactive session they may be used on the command prompt or in macros. When starting a ROOT session where BRAT is to be used, referred to as a 'BRAT session', the BRAT classes have to be loaded into memory. This is not done automatically as it is with many of the ROOT classes.

The BRAT classes are loaded as shared object files. Since many BRAT classes inherit from and depend on other BRAT classes, the order in which the BRAT shared object files are loaded is important. For this reason a macro has been generated to load these files. The macro is called *BratLoad.C* and is placed in *$BRATSYS/test* directory.

Starting ROOT from this directory makes ROOT read from the included *rootlogon.C* placed there. Once reaching the ROOT prompt do the following to load the BRAT classes[2]

```
root [0] .X BratLoad.C
```

Provided the function returns 0 all BRAT classes are now loaded into ROOT.

B.4 Documentation

ROOT has good functionality for generating documentation from C or C++ source code. This is also useful when generating BRAT documentation.

In the *$BRATSYS/test* directory there is a macro named *BratDocument.C*. Loading this macro into ROOT by doing

```
root [1] .x BratDocument.C
```

documentation about all BRAT classes may be generated with

```
root [2] BratDoc()
```

The documentation generated with this function is placed in the *$BRATSYS/html* directory and can be read with a web browser, e.g. Netscape.

[2] 'root [n]' is not to be typed. It just indicates the ROOT command prompt, which is not the same as the shell command prompt. The number n is the command number.

Appendix C

File formats

During development of the data acquisition system for the TPCs in BRAHMS, the format of the TPC data files has been updated several times. In my analysis the files are in one format only. It remains to be seen whether this is the final format.

In the current format there are two kinds of records, the header record of length of 88 bytes and the data record of 1186572 bytes, per TPC event. Information about these data records is summarized in table C.1.

The header record contains information about the length of the event data, i.e. the two records combined, as well as length, ID and flags of the header record.

Next comes the data record. This record starts with 12 bytes for record length, ID and flags. In this it is kept track of which pad and time bin the ADC values represent. The pads are named by their row number and position in the row. This is stored as a 2 byte word following the data record flags. Then come the number of the first bin and number of time bins for the pad, both stored in 2 byte words. Finally come ADC values. After the last ADC value from the first pad listed, comes another 2 byte word with row and pad number, and the pattern is repeated for all instrumented pads.

Record	**Word**	**Length** [bytes]	**Position** [bytes]	**Description**
Header		88	0	Event length, no. records, record length, ID, flags, record data
Data		1186572	88	
	record length	4	88	Length of data record
	record ID	4	92	ID of data record
	record flags	4	96	Flags for data record
	pad and row	2	100	Row number and pad number
	first bin	2	102	Time of first bin (here 0)
	number of bins	2	104	No. bins (here 512)
		$(No.bins) \cdot 2$	106	ADC values
......				
	pad and row	2	1130	Row number and pad number
......				
		4	1186660	4 bytes separation after last ADC in event
Header		88	1186664	Event length, no. records, record length, ID, flags, record data
......				

Table C.1: *Overview of the format of TPC test data files.*

References

[Alb92] Albrecht, Z. Phys. **C56** (1992) 339

[Ali99] The PHOS collaboration: Technical Design Report for the Photon Spectrometer (PHOS), CERN/LHCC 99-4 (1999)

[Ant00] F. Antinori et al., CERN preprint CERN-EP-2000-002 (2000).

[ATP95] ALICE Technical Proposal (1995), CERN/LHCC 95/71

[Bjo92] J.D. Bjorken, Acta Phys. Polon. **B23** (1992) 637

[BrWWW] The BRAHMS web pages (2000): http://www.rhic.bnl.gov/brahms/

[Bu91] H. Burkhardt, J. Steinberger, Ann. Rev. Nucl. Part. Sci. **41** (1991) 55; CERN-PPE-91-50 (1991)

[CER00] CERN Press release: New State of Matter created at CERN (2000)

[CDR95] BRAHMS Conseptual Design Report (1994), updated 1995

[Ced93] P. Cederqvist: Version Management with CVS (1993)

[Fel81] G.J. Feldman, SLAC-PUB-2839 (1981)

[Fra96] A. Frantz, NA44 coll., Nucl. Phys.**A610** (1996) 240c

[Gol60] G. Goldhaber et al., Phys. Rev. **120** (1960) 300

[Guy94] M. Gyulassy and X.N. Wang, Nucl. Phys. **B420** (1994) 583

[Har98] J.W. Harris: Relativistic Heavy Ion Physics and the Relativistic Heavy Ion Collider, (Lectures at Lake Louise Winter Institute on Quantum Chromodynamics, 1998)

[HBT56] R. Hanbury-Brown and R.Q. Twiss, Nature **178** (1956) 1046

[Hei00] U. Heinz at CERN seminar: A New State of Matter, (2000)

[Hei91] U. Heinz, K.S. Lee, Phys. Lett. **B259** (1991) 162

[Her96] B. Hermann, Diploma Thesis (1996), Ludwigs-Maximilians Universität München

[Hov82] L. van Hove, Phys. Lett. **B118** (1982) 138; Z.Phys. **C21** (1983) 93

[Kar91] F. Karsch and H. Satz, Z. Phys. **C51** (1991) 617

[Kar95] F. Karsch, Nucl. Phys. **A590** (1995) 367c

[Kha97] D. Kharzeev et at., Z. Phys. **C74** (1997) 307

[Kle87] K. Kleinknecht: Detectors for Particle Radiation, Cambridge University Press (1987), ISBN 0-521-35852-3

[Küh95] A. Kühmichel, Nucl. Instr. and Methods **A360** (1995) 52

[Lae96] E. Laermann, Nucl. Phys. **A610** (1996) 1c

[Leo94] W.R. Leo: Techniques for Nuclear and Particle Physics Experiments, Springer-Verlag (1987), rev. 1994, ISBN 0-387-57280-5

[Loh91] T. Lohse, W. Witzeling: The Time Projection Chamber, ALEPH 91-156 (1991)

[Løv97] G. Løvhøiden: Heavy Ion Collisions at High Energies, UIO/PHYS/97-01 (1997)

[Mat86] T. Matsui and H. Satz, Phys. Lett. **B178** (1986) 416

[NA49a] The NA49 Collaboration, Phys. Rev. Lett. **82** (1999) 2471

[NA49b] The NA49 Collaboration: NA49 Experimental Results Relevant to the Question of QGP formation, NA49 Note number 215 (1999)

[NA49c] The NA49 Collaboration: Projectile Fragmentation in Pb+Pb Collisions at 158 A·GeV, NA49 Note number 133 (1997)

[NA50] The NA50 Collaboration, CERN-EP-2000-013 (To be published by Phys. Lett. **B**)

[PDG98] Particle Data Group, extracts from *Review of Particle Physics*, The European Physics Journal **C3** (1998) 1

[PhWWW] The PHENIX web pages (2000): http://www.rhic.bnl.gov/phenix/

[Pov95] B. Povh, K. Rith, C. Scholz, F. Zetsche: Particles and Nuclei (1995) 120

[Raf82] J. Rafaelski and B. Müller, Phys. Rev. Lett. **48** (1982) 1066

[RDM98] RHIC Design Manual, Revised September 1998

[Ruu91] P.V. Ruuskanen, Nucl. Phys. **A525** (1991) 225c

[RoWWW] The ROOT web pages (2000): http://root.cern.ch

[SKC98] The Super-Kamiokande Collaboration: Evidence for oscillation of atmospheric neutrinos, Phys. Rev. Lett. **81** (1998) 1158-1162

[WA80] The WA80 Collaboration, Phys. Rev. Lett. **76** (1996) 3506

[WA98a] The WA98 Collaboration, Phys. Lett. **B469** (1999) 30

[WA98b] The WA98 Collaboration, Phys. Rev. Lett. **83** (1999) 926

[WA98c] The WA98 Collaboration, Phys. Lett. **B420** (1998) 169

[ZDC98] Zero Degree Calorimeters for RHIC, QCAL Group, BNL (http://www.rhic.bnl.gov/html/ZDC.html) (1998)